Fig. 15. Scatter plots showing correlations between bispectrum modes extracted from the different *Planck* foreground-cleaned maps, for all possible pairs of component separation methods. *Top*: *TTT* bispectrum modes. *Bottom*: *EEE* bispectrum modes. While temperature shows a strong correlation, the loss of correlation in polarization between the different methods is evident in these plots, as discussed in the text and quantified in Tables 14 and 15. Results here and in Table 15 have been obtained using the high resolution modal pipeline (2001 modes), while results in Table 14 have been obtained with the low resolution modal pipeline. By construction, the high resolution pipeline is measuring not the full *EEE* bispectrum of the map, but the component of *EEE* that is orthogonal to *TTT*. For this reason, r^2 measured by the two pipelines for *EEE* will not be identical. With this caveat in mind, the agreement between the two modal approaches is very good.

We also perform model-independent checks by looking at the correlation coefficient between different sets of bispectrum modes, in a similar way to Sect. 7.1.2, but now changing the polarization mask. Results are reported in Table 16, and confirm that the data and simulations behave similarly, and that polarization modes display a lower correlation level than temperature.

7.3. Tests on simulations

We consider two realistic data simulations, one of which is Gaussian, while the other includes local NG. We start with a foreground-free realization, add foregrounds according to the Planck Sky Model, and finally process through the four component separation pipelines. By estimating $f_{\rm NL}$ in the input

Table 15. r^2 statistic, Eq. (58), showing the degree of correlation between measured bispectrum β coefficients for the component separation methods shown in Fig. 15 (upper three rows for temperature, lower for polarization).

	SEVEM	NILC	Commander
SMICA (T)	0.95	0.94	0.63
SEVEM (T)		0.92	0.66
NILC (T)			0.72
SMICA (E)	0.39	0.89	0.55
SEVEM (E)		0.30	0.50
NILC (E)			0.43

Notes. Correlation between SMICA, NILC, and SEVEM is excellent in temperature; however, it declines markedly for the latter in polarization. Note that results are from the high resolution Modal 2 pipeline using the orthogonal *EEE* component only.

Table 16. Correlation coefficients between pairs of *EEE* bispectrum modes, extracted using two different masks for each of the four component-separated maps.

	EEE	
Method	Data	Simul.
SMICA	0.87	0.87
SEVEM	0.87	0.87
NILC	0.87	0.87
Commander	0.88	0.87

Notes. We compare correlations measured from data with Monte Carlo averages over 100 Gaussian realizations. The simulations were processed through the different component separation pipelines in the same way as the data, but do *not* include any foreground component. According to this test, modal expansions are stable for a change of sky coverage, with measured correlations in full agreement with expectations from simulations.

foreground-free simulation, for each method, and comparing to $f_{\rm NL}$ recovered from the cleaned maps (or with the input local $f_{\rm NL}$, for the NG case), we can assess both the impact of foregrounds on our measurement before subtraction and which method gives the highest accuracy. The necessity to clean is very apparent in the middle set of columns in Table 17, where no cleaning has been performed.

SMICA and SEVEM give the best results, both in the G and NG tests. In the G test, reported in Table 17, SMICA results show an agreement between the input and the cleaned map at the level $\sigma_{f_{\rm NL}}/2$ for all shapes, and for all of *TTT*, *EEE*, and *T+E*. SEVEM displays a similar level of accuracy, except for $f_{\rm NL}^{\rm local}$, where the difference is larger, but within one standard deviation. NILC and Commander clearly perform worse for the local shape, with NILC showing a $2\sigma_{f_{\rm NL}}$ difference, and Commander even larger than that. In the NG test, reported in Table 18, SEVEM gives the most accurate results, recovering the input with $\sigma_{f_{\rm NL}}/2$ accuracy or better. Results for SMICA are accurate at the $1\sigma_{f_{\rm NL}}$ level for the *TTT* constraint, and worse (about $2\sigma_{f_{\rm NL}}$) in *EEE*. However, the combined *T+E* measurement is again very good ($\sigma_{f_{\rm NL}}/2$). NILC is also performing very well in *TTT* and *T+E*, while the *EEE* result is more than $2\sigma_{f_{\rm NL}}$ off.

Table 17. Comparison of component separation methods, using Gaussian FFP8 simulations.

	Input map			Input map + foregrounds			Cleaned map		
	Local	Equilateral	Orthogonal	Local	Equilateral	Orthogonal	Local	Equilateral	Orthogonal
SMICA									
T	5.2 ± 5.8	29 ± 71	-8 ± 34	-107.0 ± 5.8	-23 ± 71	27 ± 34	7.8 ± 5.8	38 ± 71	-20 ± 34
E	-39 ± 30	-99 ± 133	59 ± 69	-10 ± 30	-154 ± 133	-41 ± 69	-56 ± 30	-120 ± 133	65 ± 34
$T+E$ ...	5.9 ± 5.1	14 ± 45	-20 ± 22	-118.0 ± 5.1	-32 ± 45	8 ± 22	8.3 ± 5.2	14 ± 45	-22 ± 22
SEVEM									
T	5.6 ± 5.7	32 ± 69	-8 ± 32	-113.2 ± 5.7	-8 ± 69	34 ± 32	12.7 ± 5.7	35 ± 69	-25 ± 32
E	-17 ± 41	-149 ± 175	28 ± 95	-14 ± 41	-171 ± 175	-44 ± 95	-22 ± 41	-120 ± 175	41 ± 95
$T+E$ ...	7.7 ± 5.3	12 ± 49	-37 ± 24	-126.0 ± 5.3	-29 ± 49	-57 ± 25	13.0 ± 5.3	11 ± 49	-41 ± 24
NILC									
T	5.1 ± 5.7	32 ± 69	-5 ± 31	-102.0 ± 5.7	-14 ± 69	32 ± 31	17.8 ± 5.7	85 ± 69	-16 ± 31
E	-52 ± 33	-157 ± 156	72 ± 73	-6 ± 33	-155 ± 156	-47 ± 73	-76 ± 33	-179 ± 156	113 ± 73
$T+E$ ...	5.7 ± 5.0	7 ± 46	-15 ± 21	-117.0 ± 5.9	-27 ± 46	12 ± 21	15.8 ± 5.0	-20 ± 46	-7 ± 21
Commander									
T	0.5 ± 6.2	-5 ± 73	-14 ± 36	-127.0 ± 6.2	-25 ± 73	-137 ± 36	25.6 ± 6.2	67 ± 73	-17 ± 36
E	-51 ± 38	-64 ± 160	93 ± 86	-10 ± 38	-153 ± 160	-45 ± 86	-70 ± 38	-78 ± 159	138 ± 86
$T+E$ ...	1.6 ± 5.4	-2 ± 48	-21 ± 23	-137.0 ± 5.4	-29 ± 48	13 ± 23	20.4 ± 5.4	28 ± 48	-11 ± 23

Notes. We firstly consider Gaussian, foreground-free simulations, with simulated noise for each frequency band, process them through each of the four foreground cleaning pipelines, and measure f_{NL} for the three standard shapes (columns labelled with "Input map"). We then include foregrounds and repeat the measurement, *before* applying the cleaning, and including realistic noise levels for each method (columns labelled with "Input map + foregrounds"); this step is performed in order to get an idea of the level of contamination introduced by foregrounds, before cleaning. Finally, we apply the different component separation methods, and again estimate f_{NL} from the final maps (columns labelled with "Cleaned map"). The discrepancies between f_{NL} measured on the input map, and f_{NL} extracted from the cleaned map, provide a figure of merit to assess how well foregrounds are subtracted by different methods. Results below have been obtained with the KSW estimator and the "cleaned map" results were also checked with the binned estimator.

The test described here has several limitations, the main and most obvious one being that it has been performed on just two maps (due to lack of availability of a large sample of this type of simulation at this stage). Another clear issue is that some methods, in particular `Commander`, seem to perform much better on actual data than on these simulations. On the other hand some important trends, observed in the data in previous tests, are clearly reproduced here, like the good stability of `SMICA` and `SEVEM`, especially for the combined $T+E$ results and, most notably, the fact that the clear degradation in the accuracy of the *EEE* measurement for some methods does *not* seem to propagate to $T+E$.

7.4. Dependence on multipole number

In this section we discuss another stability test of our results, namely the dependence of the results for f_{NL} on the maximum and minimum multipole number used in the analysis. This test is most easily performed with the binned bispectrum estimator, since it gets the dependence of f_{NL} on ℓ for free with its standard analysis, simply by leaving out bins in the final sum when computing f_{NL} (the binned equivalent of Eq. (39)).

The dependence on ℓ_{max} of the results for the three standard primordial shapes (local, equilateral, and orthogonal modes), is shown in Fig. 16, for T-only, E-only, and full $T+E$. As mentioned in Sect. 6, the KSW and binned estimators use $\ell_{max} = 2500$ for temperature, while the modal estimators use $\ell_{max} = 2000$. As can be seen in the figure, both the T-only and $T+E$ results are basically unchanged between $\ell = 2000$ and $\ell = 2500$ for all three shapes, showing that this difference has no impact on the results (as was to be expected from the excellent agreement between estimators in Table 10). In fact, the values of f_{NL} for T and $T+E$

Table 18. Same test as in Table 17, but with a NG map as input, with $f_{NL}^{local} = 8.8$.

	Cleaned map. Input $f_{NL}^{local} = 8.8$		
	Local	Equilateral	Orthogonal
SMICA			
T	3.1 ± 5.8	47 ± 71	-6 ± 34
E	-53 ± 30	-113 ± 133	94 ± 69
$T+E$ ...	5.7 ± 5.1	22 ± 45	-19 ± 22
SEVEM			
T	8.0 ± 5.7	43 ± 69	-11 ± 32
E	-19 ± 41	-112 ± 175	35 ± 95
$T+E$ ...	10.2 ± 5.3	19 ± 49	-37 ± 24
NILC			
T	10.2 ± 5.7	84 ± 69	7 ± 31
E	-76 ± 33	-179 ± 156	113 ± 73
$T+E$ ...	10.1 ± 5.0	20 ± 46	4 ± 21
Commander			
T	22.2 ± 6.2	81 ± 73	-5 ± 36
E	-68 ± 38	-78 ± 160	132 ± 86
$T+E$ ...	18.3 ± 5.4	35 ± 48	-9 ± 23

Notes. For this case, we only report the final value after foreground cleaning for each method. Results below have been obtained with the KSW estimator and double-checked with the binned estimator. ISW-lensing contributions are removed.

are reasonably stable (given their error bars) down to much lower values of ℓ_{max}, of about 1000.

On the polarization side we can draw a similar conclusion. The binned estimator uses $\ell_{max} = 2000$ for polarization, while the other estimators use $\ell_{max} = 1500$, but we see that results
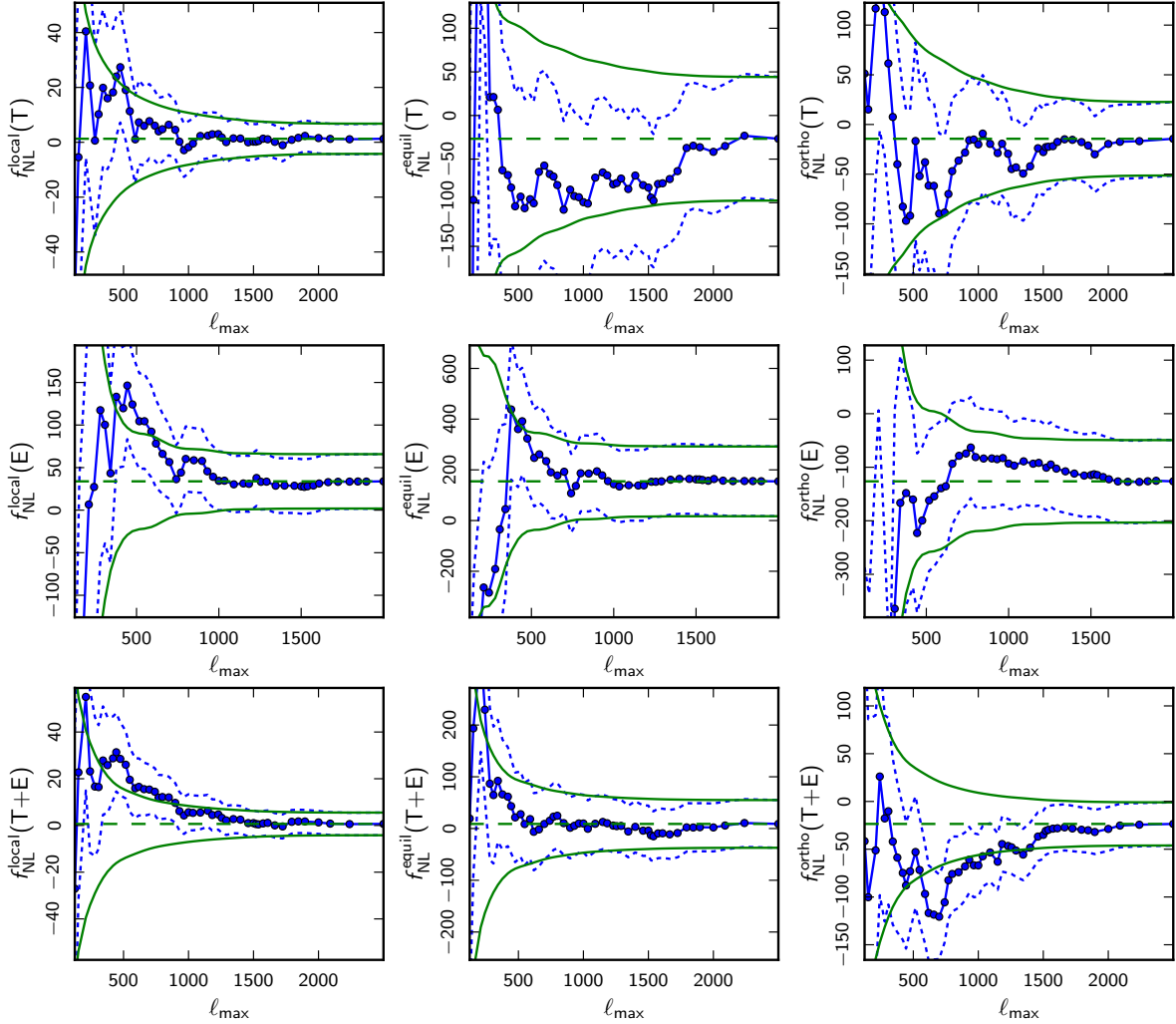
Fig. 16. Evolution of the f_{NL} parameters (solid blue line with data points) and their uncertainties (dashed lines) for the three primordial bispectrum templates as a function of the maximum multipole number ℓ_{max} used in the analysis. *From left to right* the figures show, respectively local, equilateral, and orthogonal, while the different rows *from top to bottom* show results for T-only, E-only, and full $T+E$. To indicate more clearly the evolution of the uncertainties, they are also plotted around the final value of f_{NL} (solid green lines without data points, showing the $\pm 1\sigma$ range around the dashed green lines). The results are for SMICA, and assume all shapes to be independent, and that the ISW-lensing bias has been subtracted. They have been determined with the binned bispectrum estimator.

for E remain basically unchanged between $\ell = 1500$ and $\ell = 2000$. Central values and error bars for E for all three shapes have clearly converged by $\ell = 1500$, and are in fact reasonably stable down to much lower values of about 700.

As we noted in the 2013 analysis (Planck Collaboration XXIV 2014), when going to the much lower WMAP resolution of $\ell_{max} \simeq 500$, we agree with the slightly high value of f_{NL}^{local} that the WMAP team reported (Bennett et al. 2013). This value is also confirmed when including polarization. One can clearly see the value of the higher resolution of Planck.

The dependence on ℓ_{min} is shown in Fig. 17. Here all estimators used the same values, $\ell_{min}^T = 2$ and $\ell_{min}^E = 40$. As explained in Planck Collaboration VII (2016), not all systematic and foreground uncertainties in the low-ℓ HFI polarization data have been fully characterized yet, and hence it was decided to filter out these data.

For equilateral and orthogonal shapes the values for f_{NL} and their error bars are quite stable as a function of ℓ_{min} up to about $\ell = 100$ (and $\ell \simeq 300$ for E-only), which is not surprising, since these templates have little weight at low ℓ. The local template, on

the other hand, depends very strongly on the lowest multipoles, which is reflected in the very rapid growth of the error bars when ℓ_{min} increases. Looking at T-only and $T+E$ we see a very similar pattern, with f_{NL}^{local} being reasonably stable, although there are some jumps. The local result for E-only wanders a bit more outside of the $\pm 1\sigma$ region, in agreement with the other tests in this section, which also indicate that E-only is not as stable as T-only and $T+E$. However, that is still quite acceptable, given the small weight of E-only in the full $T+E$ result.

One can work out quite generally that when Y is a subset of a data set X, and P_X and P_Y are the values of a parameter P determined from these two data sets, then the variance of the difference $P_Y - P_X$ is equal to $|\mathrm{Var}(P_Y) - \mathrm{Var}(P_X)|$ Hence we can determine how likely the jumps in f_{NL} as a function of ℓ_{min} are. It turns out that the jump in the T-only value of f_{NL}^{local} between $\ell_{min} = 40$ and $\ell_{min} = 53$ is a 2.5σ effect (using the values of f_{NL}^{local} before subtraction of the ISW-lensing bias, which also depends on ℓ). Similarly, the jump in the T-only value of f_{NL}^{equil} between $\ell_{min} = 154$ and $\ell_{min} = 211$ is (by chance) also a 2.5σ effect.
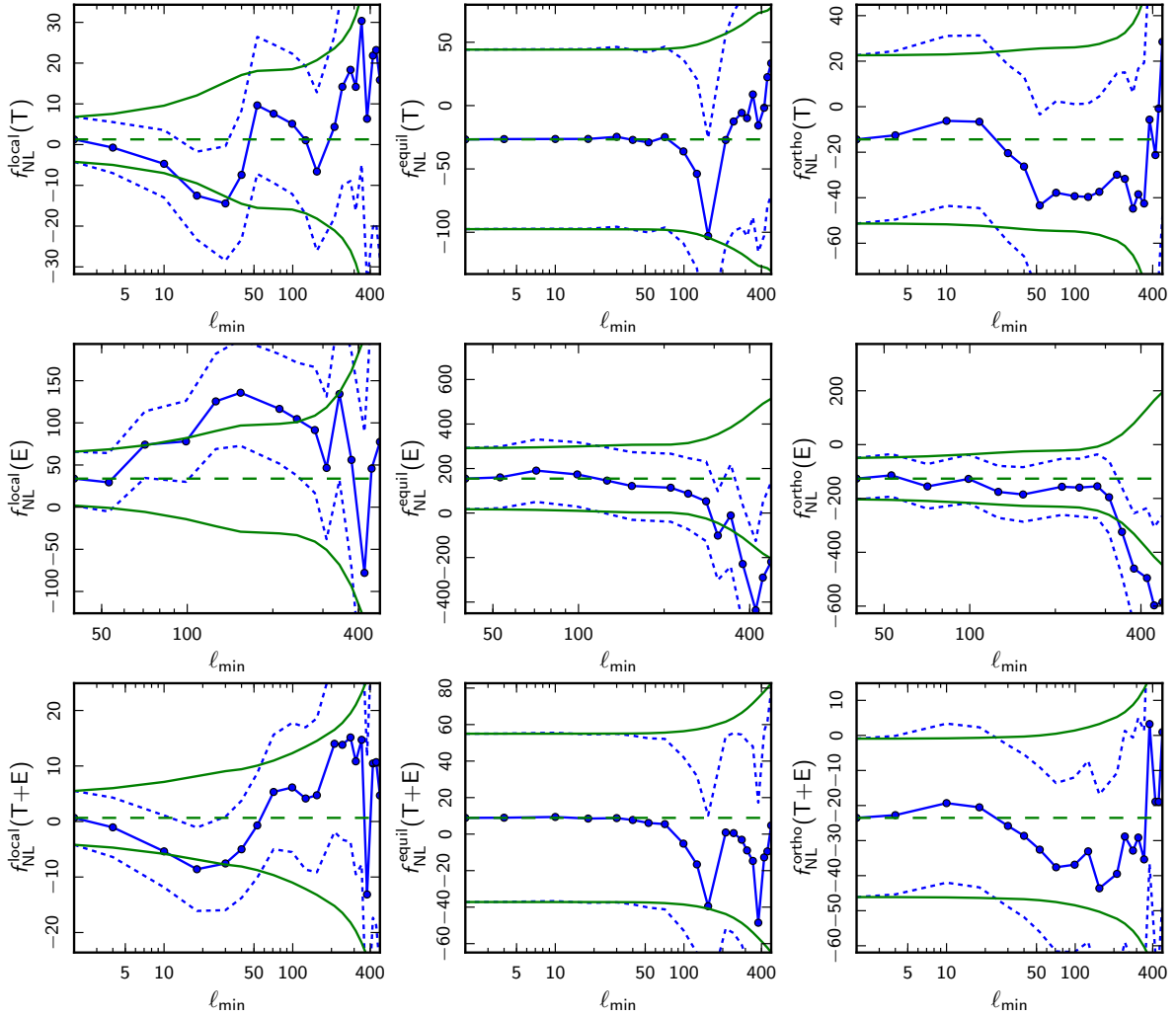
Fig. 17. Evolution of the $f_{\rm NL}$ parameters (solid blue line with data points) and their uncertainties (dashed lines) for the three primordial bispectrum templates as a function of the minimum multipole number $\ell_{\min}$ used in the analysis. *From left to right* the figures show respectively, local, equilateral, and orthogonal, while the different rows *from top to bottom* show results for T-only, E-only, and full $T+E$. To indicate more clearly the evolution of the uncertainties, they are also plotted around the final value of $f_{\rm NL}$ (solid green lines without data points, with $\pm 1\sigma$ range around the dashed green line). The results are for `SMICA`, and assume all shapes to be independent, as well as that the ISW-lensing bias has been subtracted. They have been determined with the binned bispectrum estimator.

Given the fact that there are 57 bins, having such a jump appears to be consistent from a statistical point of view.

7.5. A directional analysis with a needlet-based modal estimator

The validation tests on simulations, described in Sect. 7.3, point to `SMICA` and `SEVEM` as the best foreground cleaning methods for $f_{\rm NL}$ estimation. Results in Table 10 show that `SMICA` also has slightly smaller error bars, thus making it the method of choice for our final results.

As a further check of residual foreground contamination in the `SMICA` map, in this section we investigate the possible directional dependence of `SMICA`-derived third-order statistics by means of a needlet-based modal estimator (i.e., an estimator based on the decomposition described in Sect. 3.2, and references therein, where we use cubic combinations of needlets as our basis modes). In other words, we analyse the behaviour of the needlet bispectrum (see Lan & Marinucci 2008; Rudjord et al. 2010; Donzelli et al. 2012) on separate patches of the sky, and we study the fluctuations of the corresponding residuals.

Rather than assuming a specific anisotropic model, we instead calculate the contribution to the local $f_{\rm NL}$ from different regions of the sky and look for evidence of anisotropy in the result[15].

Our modal needlet estimator has been validated with respect to the procedures considered in Sect. 5, showing excellent agreement. Since in this paper we use the needlet estimator only in this section, and as a diagnostic tool, we will not explicitly report the outcome of these validation tests here, for the sake of conciseness. The advantages of using needlet-based modal estimators have been advocated in Lan & Marinucci (2008), Rudjord et al. (2010), Fergusson et al. (2010a, 2012); we refer to these papers for more discussion and details. In short, however, they can be summarized as follows:

1. it is possible to achieve a strong data compression, i.e., to investigate cubic statistics by means of a small number of

---

[15] Even though we focus here on directional contributions to the local shape (which was typically found as one of the most sensitive to residual foreground contamination), this type of directional analysis can be done in a model-independent way, by looking separately at different needlet modes; we leave this for future work.
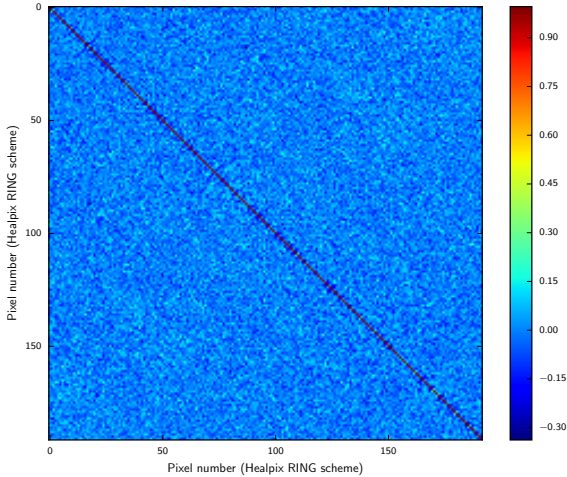
Fig. 18. Temperature only, local shape, pixel correlation matrix from Monte Carlo analysis, at $N_{side} = 4$. The most correlated pixels are those closest to the main diagonal; however, these values are always lower than 34% in the chosen case.

modes (needlet frequencies) for many different bispectrum templates;

2. needlet transforms have good correlation properties in pixel space, which allows study of the pixel contribution to the f_{NL} signal for the templates under investigation, by treating different directions independently.

In our analysis, we first divide the sky into several large "regions", with boundaries defined by the pixels of a `HEALPix` grid (Górski et al. 2005). at lower resolution than the starting map (which is at $N_{side} = 2048$). For the low resolution grid we consider N_{side} values between 2 and 8. For each pixel in the coarse grid, we then compute the local f_{NL} using our modal needlet estimator, and neglect contributions from external regions.

The correlation matrices between f_{NL} measurements in different regions were computed via Monte Carlo simulations. $N_{side} = 4$ was chosen, as providing the best tradeoff between having a large number of regions for directional analysis (i.e., the total number of pixels in the low resolution grid), and a low correlation between different regions. This is shown in Fig. 18. It is readily seen that, at $N_{side} = 4$, the correlation is largely concentrated in one or two points near the main diagonals (where it is still low, never exceeding 34%), and falls off rapidly for all other pixels. Note that the results here refer to temperature only. The *EEE* local polarization error bars are large, even for the full sky analysis, making this directional approach uninformative for *Planck* polarization data. We concentrate on the *TTT* bispectrum here, complementing other validation tests in this section, which are mostly focused on polarization.

Having obtained our correlation matrices, and having shown that different regions are essentially uncorrelated, we can then proceed to extract f_{NL} for each region in the actual `SMICA` map. As a test of directional-dependent contamination of the f_{NL} measurement, we can also compare our results, region by region, with the fluctuations expected by looking at the diagonal of our Monte Carlo correlation matrix.

The results of this analysis are shown in Fig. 19. In the left panel, we represent the directional local f_{NL} map, extracted with this method. In the right panel, we report the f_{NL} values, region by region, and compare them to expectations from simulations. The red line gives the expected standard deviation, while the blue one gives estimates on the component-separated maps with the

Monte Carlo error bars. Our estimator is normalized in such a way that the sum of all these contributions would yield exactly the f_{NL} estimator for the full map, so these results can be viewed as a partition of the estimates along the different directions. It is readily seen that no significant fluctuation occurs, so that our results are consistent with the absence of directionally-dependent features (which could occur due to, for instance, residual foreground contamination). As an additional check, we have also investigated the possible presence of a dipole in these data, and found that our results are consistent with Gaussian isotropic simulations.

7.6. Summary of the main validation results

Throughout Sect. 7 we have shown a battery of tests aimed at evaluating the robustness of our data set, from the point of view of bispectrum estimators, focusing especially on the polarizaton part. We studied the stability of our results (local, equilateral, and orthogonal f_{NL} measurements, model-independent bispectrum reconstruction) under a change of sky coverage, multipole range, and choice of component separation methods. We also considered simulated data sets and studied the ability of different component separation methods to recover the input f_{NL} after foreground subtraction. Our main conclusions from these tests can be summarized as follows:

- *TTT* and *T+E* results are stable both in the pixel and harmonic domains, for different component separation methods. For `SMICA`, we also checked that *TTT* temperature constraints on local f_{NL} show no evidence of a directional variation via a needlet-based analysis.
- `SMICA` and `SEVEM` perform better than `NILC` and `Commander` at recovering the original f_{NL} in foreground-cleaned simulations. At the same time, `SMICA` allows slightly better constraints on f_{NL} than `SEVEM`, due to a lower (by a small amount) noise level.
- *EEE* bispectra, and related f_{NL} measurements, have some problems, and do not pass all the tests. Different component separation methods show a low level of consistency (especially when comparing pixel-based cleaning methods to harmonic-based cleaning methods). This disagreement is only partly alleviated by choosing a larger *E*-mask, so that residual foregrounds do not seem to fully explain all issues. An important caveat, already pointed out previously, is that the noise model in polarized FFP8 simulations is known to underestimate the actual noise level in the data, leading to some degree of underestimation of the error bars in our *EEE* results. We stress again, however, that this has little impact on the final *T+E* constraints, due to the high noise level and consequent low statistical weight of *EEE* bispectra. This was verified in detail both on data and on simulations.

In light of the above analysis, we conclude that, as far as bispectrum estimation is concerned, our best cleaned map is the one produced by `SMICA`, in line with our previous 2013 analysis. We also conclude that our *TTT*-based f_{NL} constraints, summarized in Tables 10 and 11, are robust. Joint *T+E* constraints pass all our validation tests. On the other hand, in the light of the remaining issues in the *EEE* bispectra and in the FFP8 polarized simulations, as we stressed at the end of Sect. 6.1, we suggest that all measurements that include polarization data in this paper should be regarded as *preliminary*.
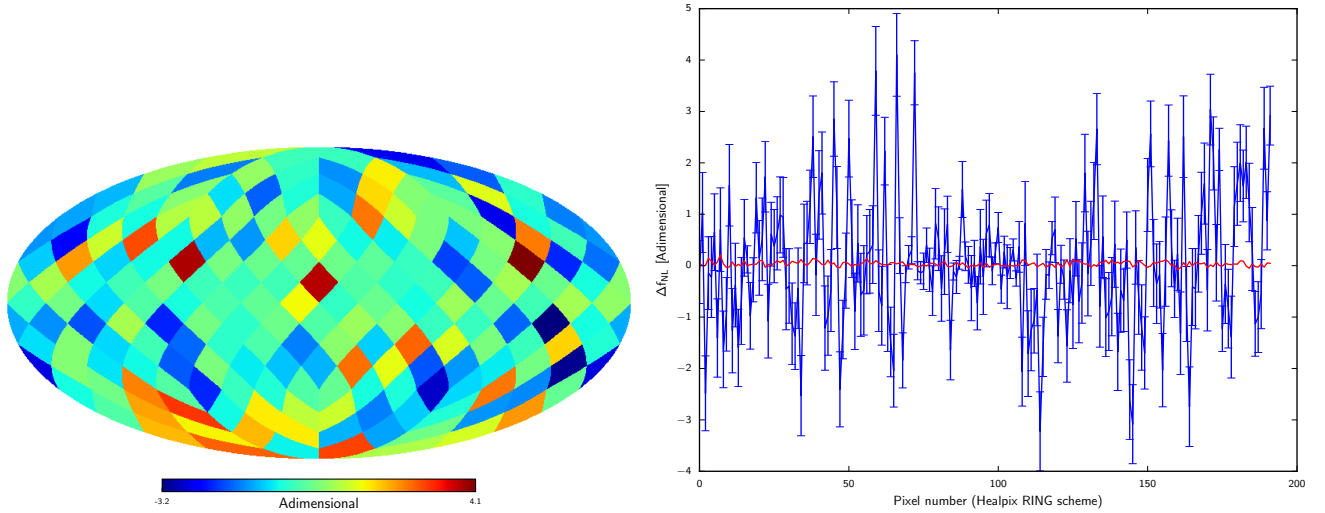
Fig. 19. Temperature only, local f_{NL} directional contributions from SMICA. As explained in the text, summing over all the pixel values would give the full sky f_{NL} needlet estimator result. The *left panel* displays the directional f_{NL} map. On the *right*, the blue points represent the f_{NL} contibution for each direction (i.e., for each pixel in the directional map), with Monte Carlo error bars. The red line is the average from simulations, which is consistent with zero.

Table 19. Results for local isocurvature NG, determined from the SMICA *Planck* 2015 map with the binned bispectrum estimator.

	f_{NL}					
	Independent			Joint		
Shape	Cold dark matter	Neutrino density	Neutrino velocity	Cold dark matter	Neutrino density	Neutrino velocity
T a,aa	1.3 ± 5.4	1.3 ± 5.4	1.3 ± 5.4	21 ± 13	-27 ± 52	-32 ± 48
T a,ai	-2 ± 10	-4 ± 15	47 ± 29	-39 ± 26	140 ± 210	370 ± 350
T a,ii	59 ± 910	-130 ± 280	750 ± 360	$17\,000 \pm 8200$	-4500 ± 4500	-1300 ± 3800
T i,aa	6 ± 50	3.0 ± 9.0	1.0 ± 4.7	96 ± 120	40 ± 99	-27 ± 51
T i,ai	3 ± 66	-5 ± 22	26 ± 21	-2100 ± 1000	220 ± 630	75 ± 170
T i,ii	76 ± 280	-100 ± 250	440 ± 230	4200 ± 2000	-750 ± 2400	-970 ± 1400
E a,aa	34 ± 34	34 ± 34	34 ± 34	66 ± 50	51 ± 120	-140 ± 150
E a,ai	-31 ± 200	70 ± 140	78 ± 93	-380 ± 310	-280 ± 640	1100 ± 620
E a,ii	-4200 ± 4000	-520 ± 2300	190 ± 940	-8800 ± 6100	-6400 ± 6200	-9400 ± 3900
E i,aa	-10 ± 87	42 ± 42	23 ± 27	27 ± 180	52 ± 170	54 ± 120
E i,ai	94 ± 250	83 ± 130	45 ± 62	910 ± 770	670 ± 850	-190 ± 420
E i,ii	690 ± 2200	390 ± 1400	260 ± 460	-6000 ± 5300	-4100 ± 5300	2200 ± 1600
$T+E$ a,aa	0.7 ± 4.9	0.7 ± 4.9	0.7 ± 4.9	5 ± 10	-35 ± 27	2 ± 24
$T+E$ a,ai	-2.6 ± 9.7	-5 ± 14	17 ± 22	-12 ± 20	74 ± 94	330 ± 130
$T+E$ a,ii	130 ± 450	-130 ± 240	130 ± 230	-1800 ± 1300	-3000 ± 1400	-3200 ± 1200
$T+E$ i,aa	30 ± 26	5.6 ± 7.7	-0.7 ± 4.1	53 ± 47	51 ± 45	-44 ± 24
$T+E$ i,ai	26 ± 38	2 ± 19	6 ± 15	140 ± 170	170 ± 210	20 ± 74
$T+E$ i,ii	38 ± 170	-26 ± 180	85 ± 130	-280 ± 390	-390 ± 860	480 ± 430

Notes. In each case the adiabatic mode is considered together with one isocurvature mode (either cold dark matter, neutrino density, or neutrino velocity isocurvature). As explained in the text this gives six different f_{NL} parameters, indicated by the different combinations of the adiabatic (a) and isocurvature (i) modes. Results with two significant digits are shown for both an independent and a fully joint analysis, for T-only, E-only, and full $T+E$. In all cases the ISW-lensing bias has been subtracted.

8. Other non-Gaussianity shapes for f_{NL}

This section discusses new searches for NG beyond standard single-field inflation. The focus here is on extensions to the analysis undertaken in Planck Collaboration XXIV (2014) with new limits on isocurvature models, further oscillatory models over a broader frequency range, and parity-violating tensor NG. However, we also briefly revisit all the non-standard models constrained in Planck Collaboration XXIV (2014), including effective field theory, non-Bunch Davies, and directionally-dependent models, in particular noting the impact of the new (preliminary) polarization data on the previous constraints.

8.1. Isocurvature non-Gaussianity

Here we show the results obtained for a study of the isocurvature NG in the *Planck* 2015 SMICA map using the binned bispectrum estimator. As explained in Sect. 2.3, we only investigate

Table 20. Similar to Table 19, except that we now assume that the adiabatic and isocurvature mode are completely uncorrelated.

	f_{NL}					
	Independent			Joint		
Shape	Cold dark matter	Neutrino density	Neutrino velocity	Cold dark matter	Neutrino density	Neutrino velocity
T a,aa	1.3 ± 5.4	1.3 ± 5.4	1.3 ± 5.4	1.0 ± 5.3	19 ± 12	-0.2 ± 5.4
T i,ii	76 ± 280	-100 ± 250	440 ± 230	65 ± 280	-840 ± 540	440 ± 230
E a,aa	34 ± 34	34 ± 34	34 ± 34	33 ± 35	42 ± 40	35 ± 40
E i,ii	690 ± 2200	390 ± 1400	260 ± 460	210 ± 2200	-680 ± 1700	-31 ± 540
$T{+}E$ a,aa	0.7 ± 4.9	0.7 ± 4.9	0.7 ± 4.9	0.5 ± 5.0	3.0 ± 7.9	-0.3 ± 4.9
$T{+}E$ i,ii	38 ± 170	-26 ± 180	85 ± 130	35 ± 170	-120 ± 290	87 ± 130

Notes. Hence there are only two f_{NL} parameters in this case, a purely adiabatic one and a purely isocurvature one.

isocurvature NG of the local type, and in addition always consider only one isocurvature mode (either cold dark matter, neutrino density, or neutrino velocity isocurvature) in addition to the adiabatic mode. Note that the baryon isocurvature mode behaves identically to the cold dark matter one, only rescaled by factors of Ω_b/Ω_c, so there is no need to consider it separately. In that case there are six different f_{NL} parameters: a purely adiabatic one (a,aa), which corresponds to the result from Sect. 6), a purely isocurvature one (i,ii); and four mixed ones (see Sect. 2.3 for an explanation of the notation).

The results are given in Table 19[16] and show no clear signs of any isocurvature NG. There are a few values that deviate from zero by up to about 2.5σ, but such a small deviation, in particular given the large number of results, cannot be considered a detection. We do see that many constraints are tightened considerably when including polarization, by up to the predicted factor of about six for the cold dark matter a,ii, i,ai, and i,ii modes in the joint analysis. As discussed in detail in Sect. 7, results including polarization data should be considered preliminary, and that is even more important here, since these results depend so strongly on the additional information from polarization.

In the results so far we allowed for a possible correlation between the isocurvature and adiabatic modes. However, if we assume that they are completely uncorrelated, with a zero cross power spectrum, then there are only two f_{NL} parameters, the a,aa and i,ii ones. In Table 20 we give the results for this uncorrelated case. The independent results are the same as in the previous table, while in the joint results one can clearly see the difference between the neutrino density mode (the bispectrum template of which has a large overlap with the adiabatic one), and the cold dark matter and neutrino velocity modes (with templates that are very different from the adiabatic one). Again there is no evidence for any isocurvature NG; the almost 2σ result for the neutrino velocity isocurvature mode in the temperature-only case does not survive the addition of polarization.
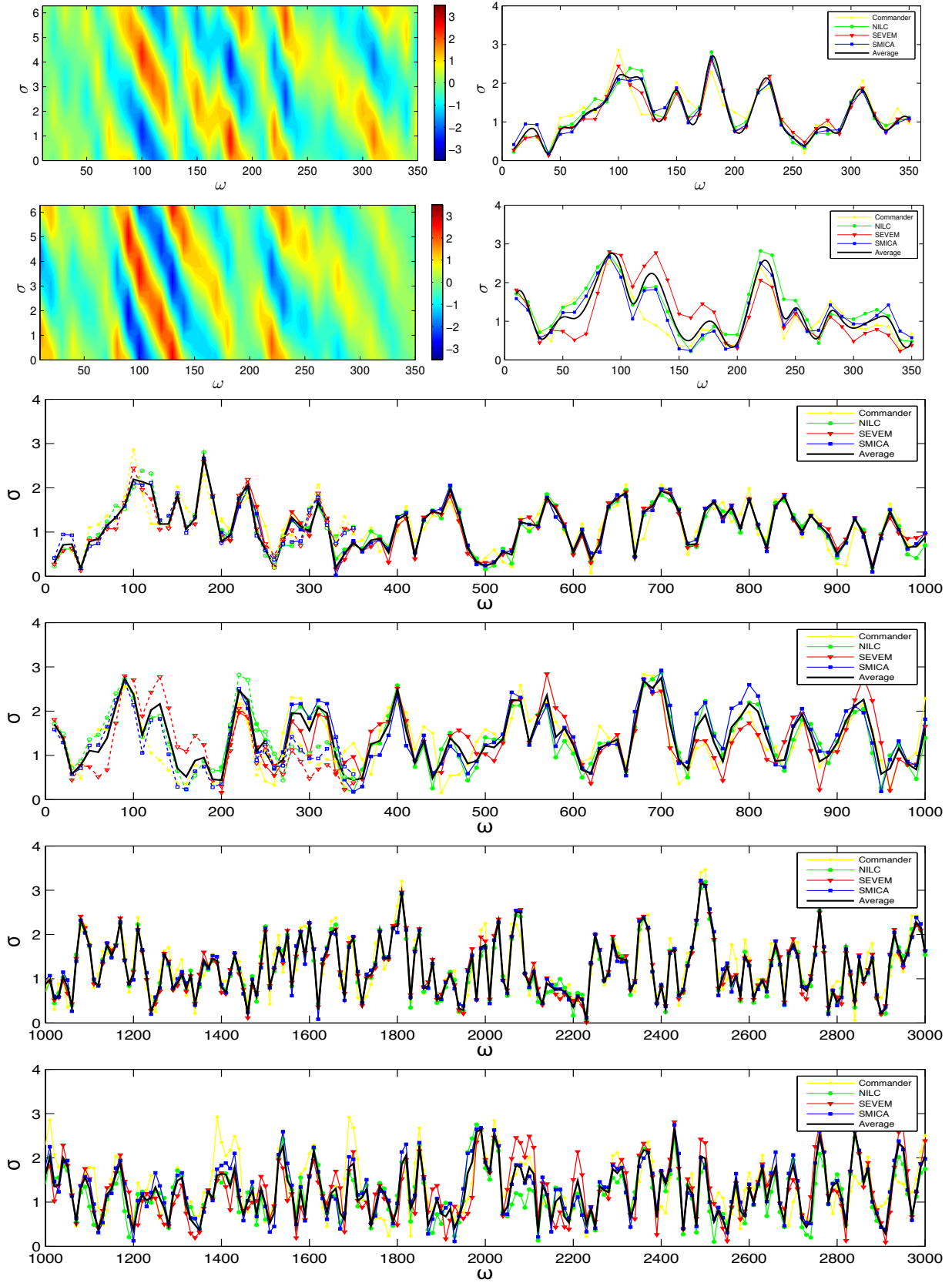
8.2. Feature models

An important and well-motivated class of scale-dependent bispectra is the feature model, characterized by linear oscillations

described by Eq. (15) and its variants in Eqs. (16) and (18). In Planck Collaboration XXIV (2014) we performed an initial search for a variety of feature models using the Modal estimator. This earlier search was limited to $\omega < 200$ by the native resolution of our implementation of the Modal estimator (using 600 modes), roughly the same range as the initial WMAP bispectrum feature model searches at lower precision (with only 50 eigenmodes (Fergusson et al. 2012). Note, in the previous *Planck* release we used wavenumber k_c in line with the theory literature, but here we switch to frequency ω, in line with more recent observational power spectrum searches; the two are related by $\omega = 2\pi/3k_c$. With the improved estimator resolution (now using 2001 modes) we are able to achieve convergence over a broader range up to $\omega = 350$. We perform a frequency scan of 350 sampling points between $\omega = 10$ and $\omega = 350$, i.e., 35 independent frequencies and 10 phases. We also extend the number and variety of feature and resonance models that are investigated, essentially probing the resolution domain in which we have obtained a reliable Modal bispectrum reconstruction (see Fig. 4).
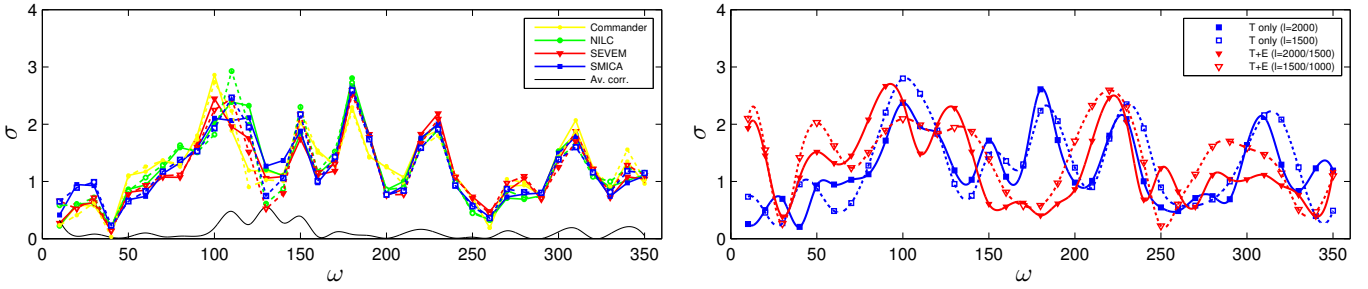
Constant feature ansatz: for the constant feature shape of Eq. (15), we can extend the frequency range much further with another approach. As the bispectrum in Eq. (15) is separable, it allows the construction of a KSW estimator (Münchmeyer et al. 2014) for direct bispectrum estimation at any given frequency. The bispectrum can be written as a sum of sine and cosine components which can be estimated separately (equivalent to measuring the amplitude and phase above) and this method was used to constrain frequencies up to $\omega = 3000$. The range where the two estimators overlap provides validation of the two methods and excellent agreement was seen (see Fig. 20).

Apart from cross-validation with two estimators, we have undertaken further tests to determine the robustness of the results to foreground and noise effects. In Fig. 21 (left panel), we show the effect on feature model results of the subtraction of the simple point source bispectrum, as well as the ISW-lensing bispectrum. This study was a major motivation for adopting the more conservative "extended" common mask, because the consistency between different component separation methods improved markedly for low frequencies, with the original common mask requiring much larger point-source subtractions (e.g., for NILC subtraction the maximum raw significance has reduced from $\sigma = 4.0$ to $\sigma_{\mathrm{clean}} = 2.2$ at $\omega = 110$). After cleaning these signals, the SMICA, SEVEM and NILC results are in good agreement, and also consistent with each other when polarization is included (while the Commander results generally have a larger variance and so are not included in the plotted

---

[16] Compared to definitions in the literature based on ζ and S (see e.g., Langlois & van Tent 2012), here we adopt definitions based on $\Phi_{\mathrm{adi}} = 3\zeta/5$ and $\Phi_{\mathrm{iso}} = S/5$, in order to make the link with the standard adiabatic result more direct. Conversion factors to obtain results based on ζ and S are 6/5, 2/5, 2/15, 18/5, 6/5, and 2/5, for the six modes, respectively.

Fig. 20. Constant feature model results for both *T*-only and *T+E* data across a wide frequency range. The *upper four panels* show the feature signal in the Modal range $0 < \omega < 350$. The *two upper left panels* show contours of the raw significance σ obtained from the SMICA map as a function of the frequency ω, for *T*-only and *T+E*, respectively. The *upper right panels* show the maximum signal after marginalizing over phase ϕ for both *T*-only and *T+E* for all foreground separation models. The *third and fourth panels* show the maximum feature signal in both *T*-only and *T+E* across the frequency range $0 < \omega < 1000$, plotting both Modal results (dashed lines) and KSW results (solid lines for $200 < \omega < 1000$); these show good agreement in the overlap. The *lower two panels* give the maximum KSW results for *T*-only and *T+E* in the range $1000 < \omega < 3000$).

Fig. 21. Constant feature ansatz validation for the Modal estimator, showing the effect of ISW-lensing and point source subtraction for $\ell < 300$ (*left panel*) and the impact of a lower ℓ maximum cutoff on the average signal (*right panel*), i.e., lowering $\ell_{\max} = 2000$ to 1500 (T) and $\ell_{\max} = 1500$ to 1000 (E). All Modal 2 results in Sect. 8 have used the extended common mask, except the validation analysis at different resolutions (*right panel*) which for consistency employs the common mask.

averages). Fortunately, the effect of subtracting ISW-lensing and point source bispectra diminishes rapidly at higher frequencies $\omega > 200$ and should be negligible; subtraction was only undertaken in the Modal region $\ell < 350$. In Fig. 21 (right panel), we show the effect on the averaged significance of reducing the *Planck* domain from the usual $\ell_{\max} = 2000$ to $\ell_{\max} = 1500$ ($\ell_{\max} = 1500$ to $\ell_{\max} = 1000$ for E-modes). Despite the nontrivial change in overall signal-to-noise entailed, there is no strong evidence for an ℓ-dependent signal, as might be expected if there was substantial NG feature contamination in the noise-dominated region. Finally, we note that most peaks at low ω show some correlation between T-only and $T+E$, although there are notable exceptions, such as the peak at $\omega = 180$, which is removed after inclusion of polarization (see also the phase plots in Fig. 20 before marginalization). The temperature feature peaks observed in Fig. 21 at $\omega \approx 110$, 150, and 180 are consistent with the peaks identified previously in Planck Collaboration XXIV (2014).

In Fig. 20, the full set of frequency results, $0 < \omega < 3000$, for the constant feature model in Eq. (15) is shown for both the Modal and KSW estimators. There is good agreement for regions where the estimators overlap and PS and ISW lensing bispectra subtraction is not necessary ($\omega > 200$). Generally, there is tighter consistency between temperature-only results, than with polarization where there is additional scatter between foreground separation methods. Scanning across the full frequency range, there is no strong evidence for any large maximum that might indicate unequivocal evidence for a feature model signal. The maximum peak significance obtained with either T-only or $T+E$ is consistent with expectations for a Gaussian model over this frequency range. In particular, for the KSW estimator using the SMICA data, the highest significance found in the range $200 < \omega < 3000$ is 3.2σ in T-only and 2.9σ in $T+E$. To gauge the likelihood of these results occurring randomly, realistic Gaussian SMICA simulations were analysed with the KSW estimator and found to typically produce a highest peak with $3.1(\pm 0.3)\sigma$ over the same frequency range.

Generalized feature models: we have also deployed the Modal estimator to look at (non-separable) feature models with equilateral and flattened cross-sections, as motivated by varying sound speed scenarios and those with highly excited states, respectively. In the left panels in Fig. 22 we show results from the equilateral feature model of Eq. (16), including the frequency/phase contours before marginalization for the SMICA T-only map. Multiple peaks are apparent in the temperature signal across the Modal range up to an average maximum 3.3σ raw significance. However, from the lower panel it is clear that

the polarization signal is not well correlated with the temperature in the equilateral case, generally reducing peak heights with the maximum now about 2.6σ (while eliminating the $\omega = 180$ peak altogether). This temperature peak remains present with the $\ell_{\max} = 1500$ cutoff, where the signal is slightly higher, but the polarization in this case is less well correlated (using $\ell_{\max}^E = 1000$). For Gaussian noise we would not expect polarization to reinforce a high temperature signal on average. It may also be that the equilateral temperature signal has some residual diffuse point-source contamination. The equilateral feature model is the most affected by the removal of point sources, so the presence of a more complex correlated PS bispectrum (not removed by the constant PS template subtraction) remains for future investigation.

Results for the flattened feature model in Eq. (18) are shown in Fig. 22 (right panels), displaying more coherence between temperature and polarization. The temperature signal with a 2.6σ peak between $50 < \omega < 150$ is reinforced by polarization and merges to make a broad 3σ peak around $\omega = 90$, together with another distinct peak at $\omega \approx 140$. Such broad frequency peaks are not expected, because neighbouring feature models should be nearly uncorrelated over a range $\Delta\omega_{\rm eft} \approx 13$ (as we discuss below). As the phase plots in Fig. (22) indicate, this breadth in frequency ω may reflect the neighbouring feature models adjusting phase ϕ to match an underlying NG signal of a related, but different, nature. We note also that the frequency region for $\omega < 100$ is susceptible to some degeneracy with cosmological parameters. We shall consider a "look-elsewhere" statistical analysis of these results below.

Single-field feature solutions: we have also searched for the specific analytic solutions predicted for single-field inflation models with step-like potential features, as given in Eqs. (19) and (20), with results shown in Fig. 23. The highest peaks for the K^2-cosine model occur around 2.5σ with temperature-only, then rises to 2.7σ when polarization data are included, again with peaks at other distinct frequencies apparent. The K-sine model shows a similar apparent signal level, with a maximum T-only 2.7σ peak, dropping to 2.4σ with polarization. One further difficulty with a positive interpretation of these bispectrum results in this low frequency range is that stronger S/N counterparts in the power spectrum are predicted for these simple models (Adshead et al. 2011), whereas no significant correlated oscillation signals are apparent at the relevant peak frequencies Planck Collaboration XX (2016).

Feature model peak statistics: in order to determine consistency with Gaussianity for these feature model results, we can apply a number of statistical tests developed for this specific
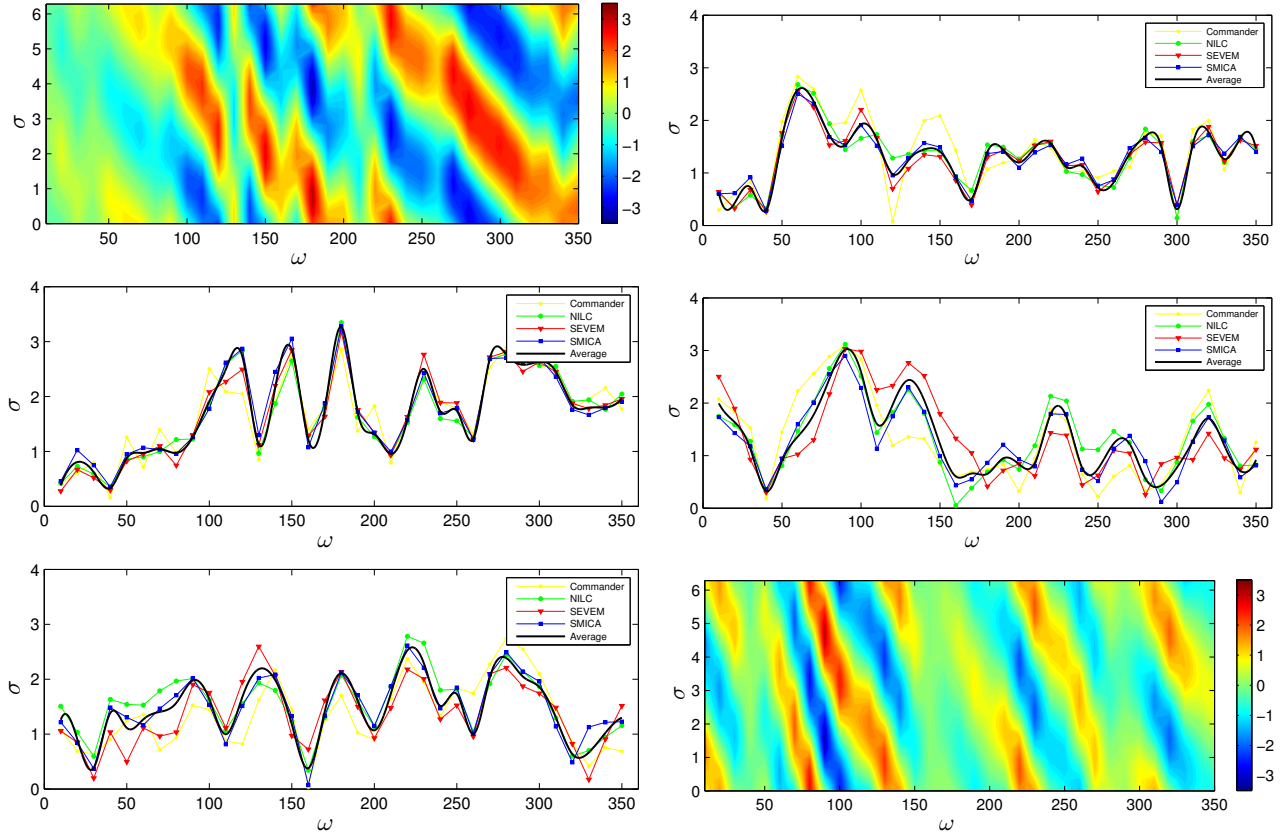
Fig. 22. Generalized feature models analysed at $\ell_{max} = 2000$ (*E*-modes $\ell_{max} = 1500$) for the different *Planck* foreground separation methods, SMICA (blue), SEVEM (red), NILC (green), and Commander (yellow), together with the SSN (SMICA - SEVEM - NILC) average (black). The *left three panels* apply to the equilateral feature models, showing, respectively, in the *top panel* the full feature survey significance at each frequency and phase (temperature only), the maximum significance at each frequency for temperature only (*middle*), and with polarization (*lower*). The *right three panels* apply to the flattened feature models, showing the maximum significance at each frequency for temperature only (*top right*) and with polarization (*middle right*), along with significance at each frequency and phase for temperature and polarization (*right lower*).

Table 21. Peak statistics for the different feature models showing the *Raw* peak maximum significance (for the given Modal survey domain), the corrected significance of this *Single* maximum peak after accounting for the parameter survey size (the "look-elsewhere" effect) and the *Multi*-peak statistic which integrates across the adjusted significance of all peaks to determine consistency with Gaussianity.

	SMICA			SEVEM			NILC			Commander		
	Raw	Single	Multi	Raw	Single	Multi	Raw	Single	Multi	Raw	Single	Multi
Features constant *T*-only	2.7	0.5	1.7	2.6	0.4	1.5	2.8	0.7	2.2	2.9	0.8	2.7
Features constant *T+E*	2.7	0.5	1.9	2.8	0.7	2.5	2.8	0.7	2.4	2.6	0.4	1.5
Features equilateral *T*-only	3.3	1.5	4.0	3.2	1.3	3.5	3.3	1.6	4.1	2.9	0.9	2.5
Features equilateral *T+E*	2.6	0.4	1.3	2.6	0.4	1.6	2.8	0.7	1.9	2.7	0.6	1.5
Features flattened *T*-only	2.5	0.3	1.4	2.6	0.4	1.6	2.7	0.5	2.1	2.8	0.8	2.7
Features flattened *T+E*	2.9	0.9	2.9	3.0	1.1	3.5	3.1	1.2	3.8	3.1	1.2	3.8
K^2 cos features *T*-only	2.5	0.7	1.9	2.3	0.6	1.6	2.7	1.0	2.5	2.2	0.3	1.1
K^2 cos features *T+E*	2.7	1.0	2.5	2.7	1.1	2.6	2.6	1.0	2.5	2.4	0.6	1.8
K sin feature *T*-only	2.8	1.2	2.8	2.7	1.1	2.7	3.0	1.5	3.4	2.6	0.9	2.3
K sin features *T+E*	2.1	0.3	1.0	2.9	1.4	3.1	2.4	0.6	1.7	2.3	0.5	1.6

Notes. SMICA, SEVEM and NILC map analyses exhibit satisfactory bispectrum agreement for all the different models, whereas the Commander results produce some anomalously large results, especially for polarization. The significant signal for the equilateral features model in the *T*-only multi-peak statistic is reduced when polarization is added. The flattened feature model produces interesting results, which are reinforced with polarization to the 3σ-level, with a high multi-peak significance.

purpose (Fergusson et al. 2015) and, if warranted, also apply these jointly in combination with power spectrum results, as for the WMAP polyspectra analysis (Fergusson et al. 2015). When scanning across the (ω, ϕ) parameter-dependent feature models, we are searching through independent models for which

Gaussian noise, by chance, can lead to a large apparent signal. We must correct for this multiplicity of tests when determining the actual significance of results for a given model – this is a quantitative correction for any model with free parameters, distinct from the a posteriori choice of models to test. The simplest
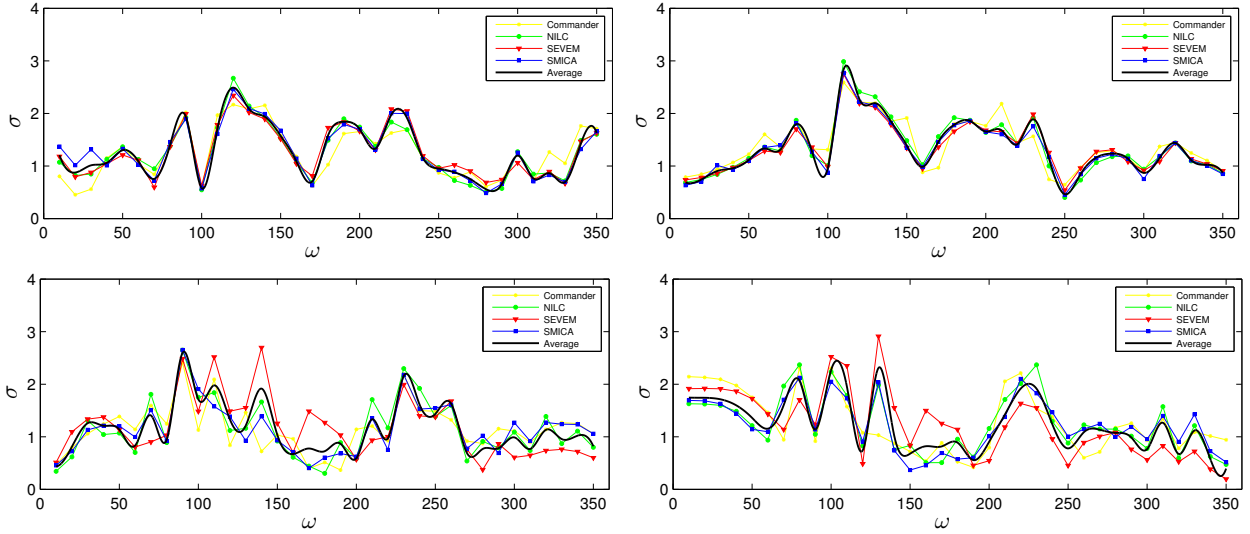
Fig. 23. Single field feature model significance with a $K^2 \cos \omega K$ scaling dependence (Eq. (19); *left panels*, *T*-only *upper* and $T + E$ *lower*) or with a $K \sin \omega K$ scaling (Eq. (20); *right panels*). To find the maximum signal, these results have been marginalized over the α-dependent envelope function ranging from $\alpha \to 0$ (no envelope) to the maximum cutoff allowed by the Modal resolution $\alpha\omega = 90$.

approach is to determine whether the maximum peak is consistent with Gaussian expectations, which can be determined from Monte Carlo simulations. However, in Fergusson et al. (2015) it was recognized that these feature models can be accurately characterized analytically with a χ-distribution having two degrees of freedom[17]. Taking $\ell_{max} = 2000$ and using this analysis, the frequency step size between models that are uncorrelated is approximately $\Delta\omega_{eff} = 13$, so we have an effective number of independent feature models $N_{eff} \approx 27$ for the Modal frequency range (with $N_{eff} \approx 230$ across the larger constant feature survey range). Accordingly appropriate look-elsewhere corrections have been applied to find an adjusted significance for the maximum peak signal found in all the feature model searches undertaken, which is shown in Table 21. Given that this feature model survey is over many independent frequency models and combinations of data, even the highest raw significances above 3σ ("Raw" column in Table 21) are reduced to a corrected significance below 2σ ("Single" column). Hence, there appears to be no evidence from maximum peak statistics for feature model deviations from Gaussianity.

Nevertheless, we also examine the possibility that multiple feature models are contributing to a NG signal, given the

---

[17] For the feature model with parameters (ω, ϕ), the adjusted significance S for the raw significance σ after accounting for the "look-elsewhere" effect is given by (Fergusson et al. 2015)

$$S = \sqrt{2}\,\mathrm{Erf}^{-1}[(F_{\chi,2}(\sigma))^{N_{eff}}], \qquad (59)$$

where $F_{\chi,2}$ is the cumulative distribution function of the χ-distribution of degree two and N_{eff} is the effective number of independent feature models. This can also be used to investigate whether feature models are contributing at several frequencies. This multi-peak statistic integrates over all peak signals using the corrected significance S, i.e.,

$$S_I^2 = \frac{\Delta\omega}{\Delta\omega_{eff}} \sum_{\omega} 2\mathrm{Erf}^{-1}[F_{\chi,2}(\sigma(\omega))^{N_{eff}}]^2, \qquad (60)$$

where $\Delta\omega$ is the sampling step-size and $\Delta\omega_{eff}$ is the effective correlation scale between independent models given by $\Delta\omega_{eff} = (\omega_{max} - \omega_{min})/(N_{eff}-1)$. Essentially this sums up all significant peaks that have a non-zero adjusted significance, after accounting for the look-elsewhere effect in Eq. (59).

apparent emergence of several preferred frequency peaks. This integrated multi-peak statistic can also be accurately approximated analytically (Eq. (60)) using a χ-distribution; essentially we sum over all independent frequencies using the single peak significance adjusted for the "look-elsewhere" effect (see Eq. (59)). Most of the signal surveys exhibit an unusual number of broad overlapping peaks within the accessible frequency domain, so the multi-peak statistic does yield a much higher significance, with many models above 2σ after "look-elsewhere" correction. Notable cases are the temperature-only signal for the equilateral feature model which yields an average significance of 3.4σ across the foreground-cleaned maps with concordant bispectrum results (i.e., SMICA, SEVEM and NILC); however, this interesting multi-peak significance drops to only 1.6σ when the polarization data are included (assuming the reliability of E results). On the other hand, the flattened feature model has an average multi-peak significance of 1.7σ in temperature only, which rises to 3.4σ with polarization included (higher at 3.7σ if Commander data were to be included in the average). In this case, beyond the number of peaks, it is also their width that contributes, with the main signal around $\omega \approx 90$, much broader than $\Delta\omega \approx 13$. Finally, after look-elsewhere effects are taken into account, the K^2-cosine single-field solutions yield multi-peak statistics that rise with the inclusion of polarization data from 2.0σ to 2.5σ, while the K-sine falls from 3.0σ (T) to 1.9σ ($T+E$).

An interesting, but not entirely coherent, picture emerges from these searches for non-standard models in the new *Planck* temperature data, especially when combined with the additional (preliminary) polarization information. In Planck Collaboration XXIV (2014), we noted that the feature model searches provided interesting hints of NG. This more rigorous statistical analysis confirms this view, allowing for several alternative feature model explanations of the apparently high NG signal observed in the bispectrum reconstructions (see Fig. 4). However, there is no strong evidence for a single large feature model at a particular frequency; rather, the high multi-peak statistics indicate signal that is spread across several broad peaks. Given the variability between different feature models and polarization component-separation methods, we note the
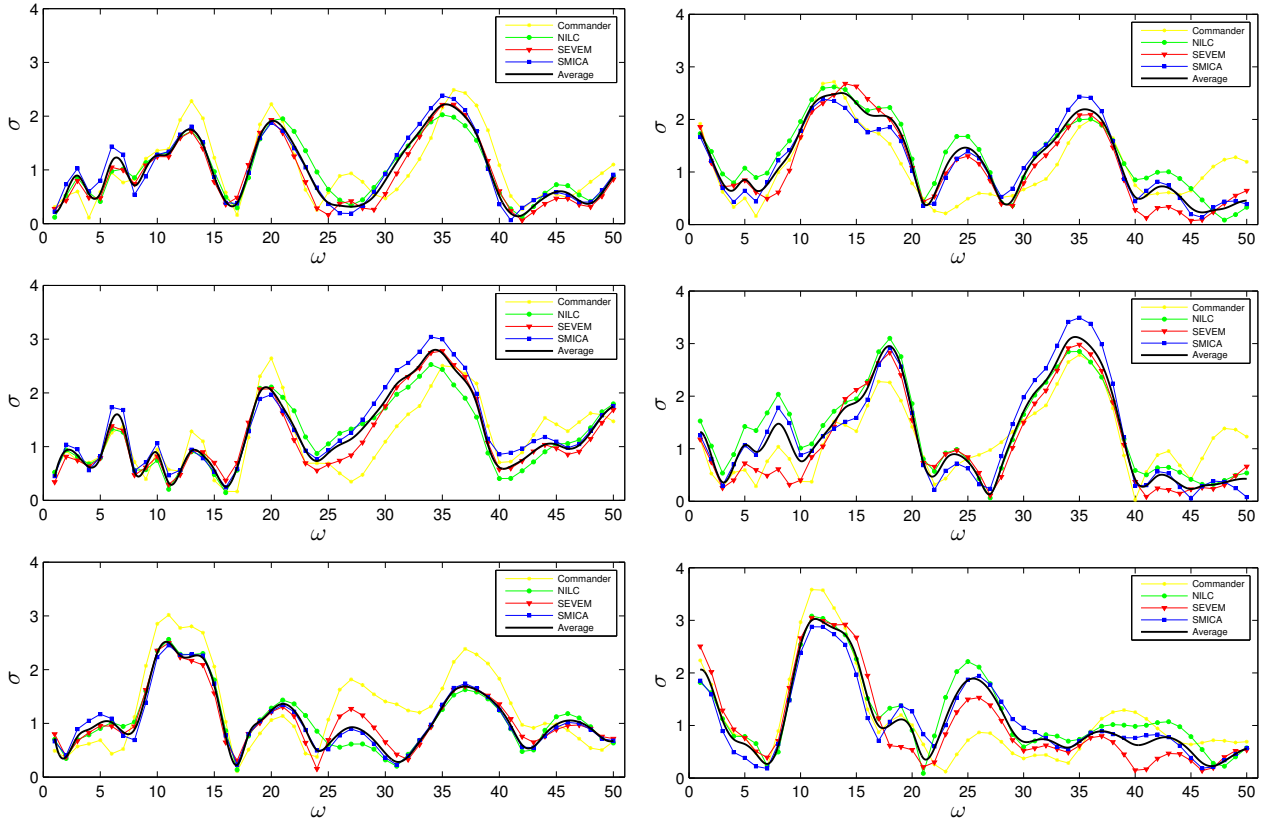
Fig. 24. Generalized resonance models analysed at $\ell_{max} = 2000$ (E-modes $\ell_{max} = 1500$) for the different *Planck* foreground separation methods, SMICA (blue), SEVEM (red), NILC (green), and Commander (yellow), together with the SSN (SMICA − SEVEM − NILC) average (black). The *upper panels* apply to the constant resonance model (Eq. (10)), with *T*-only (*left*) and *T+E* (*right*), the *middle panels* give results for the equilateral resonance model (Eq. (13)), and the lower panels for the flattened resonance model (Eq. (14)). Both the equilateral and flattened resonance models produce broad peaks, which are reinforced with polarization (*middle and bottom right panels*).

caveat that the integrated multi-peak statistic could be sensitive to calibration issues and foreground contamination. For this reason, we do not make strong claims for these non-standard signals at this stage, but we note that oscillatory models will continue to be investigated thoroughly over a wider frequency domain and using the more reliable polarization data available in the final *Planck* data release.

8.3. Resonance/axion monodromy models

Generalized resonance models: using the Modal expansion, we have embarked on a survey of the simplest resonance model (Eq. (10)), as well as the equilateral and flattened variants proposed in the literature, i.e., described by Eqs. (13) and (14), respectively. The raw significance for the resonance models for both temperature-only and temperature plus polarization data are shown in Fig. 24; these are the maximal results marginalized over the phase parameter ϕ. Previously, the resonance model was studied in Planck Collaboration XXIV (2014) using the Modal expansion over a narrower frequency range yielding no results above a raw significance of 1σ. In this extended analysis over a wider frequency range, the constant sin(log) model (Eq. (10)) produces 2.2σ peaks for *T*-only, and 2.6σ for *T+E*. The equilateral resonance model (Eq. (13)) achieves a maximum 2.8σ in *T*-only at $\omega \approx 35$, rising to a more impressive average 3.2σ for *T+E*. For the flattened case (Eq. (14)) we have 2.5σ and 3.0σ, respectively at $\omega \approx 12$. Qualitatively, the results shown in

Fig. 24, exhibiting broad peaks, are similar to those for feature models.

Resonance model peak statistics: to determine the statistical significance of these results given the look-elsewhere effect of scanning across the parameters (ω, ϕ), we have used the two peak statistics defined above in Eqs. (59) and (60) for feature models (Fergusson et al. 2015). In this case, the maximum peak statistic for the constant resonance model of 2.6σ (*T+E*) is readjusted to an unremarkable "look-elsewhere" single peak significance of 0.9σ. Likewise the apparently significant results above 3σ for the equilateral and flattened models now fall below 2.0σ with *T+E*. Using the single peak statistic alone, we would conclude that there is no strong evidence for any individual resonance model. Resonance models also generate oscillations in the power spectrum, and an analysis based on the 2015 temperature and polarization likelihood is presented in (Planck Collaboration XX 2016). A combined statistical treatment of resonance model power spectrum and bispectrum results will be reported in the future.

The multi-peak statistic in Eq. (60) integrates the resonance model signal across all frequencies to determine consistency with Gaussianity. The constant resonance model has a modest multi-peak signal but, like the feature models, the equilateral and flattened resonance shapes offer stronger hints. The multi-peak equilateral signal rose from 1.9σ (*T*-only) to 3.1σ (*T+E*) after adjusting for the "look-elsewhere" effect, while the flattened signal went from 2.4σ (*T*-only) to 3.2σ (*T+E*). These interesting results, reflecting those obtained for feature models, suggests the

Table 22. Peak statistics for the resonance models showing the maximum *Raw* peak significance, the *Single* peak significance after accounting for the parameter survey "look-elsewhere" effect, and the *Multi*-peak statistic integrating across all peaks (also accounting for the "look-elsewhere" correction).

	SMICA			SEVEM			NILC			Commander		
	Raw	Single	Multi	Raw	Single	Multi	Raw	Single	Multi	Max.	Single	Multi
Sin(log) constant T-only	2.4	0.7	1.2	2.2	0.4	0.9	2.0	0.2	0.7	2.5	0.8	1.6
Sin(log) constant $T+E$	2.4	0.7	1.7	2.7	1.1	2.4	2.6	1.0	2.2	2.7	1.1	2.5
Sin(log) equilateral T-only	3.0	1.6	2.4	2.8	1.2	2.0	2.5	0.9	1.5	2.6	1.0	2.1
Sin(log) equilateral $T+E$	3.5	2.2	3.5	3.0	1.5	2.8	3.1	1.7	3.2	2.8	1.2	2.0
Sin(log) flattened T-only	2.5	0.7	1.8	2.5	0.8	1.9	2.6	0.9	2.1	3.0	1.6	3.2
Sin(log) flattened $T+E$	2.9	1.4	2.9	3.0	1.6	3.4	3.1	1.6	3.4	3.6	2.3	4.5

Notes. There is some evidence for a high signal for both the equilateral and flattened resonance models, which increases when the polarization signal is added. This table does not include the results of the high frequency resonance model estimator, whose significance was assessed independently.

fit to any underlying NG signal might await alternative, but related, oscillatory models for a more compelling explanation.

High frequency resonance model estimator: we have further surveyed the simple resonance model (Eq. (10)) with a second approach. Using a model-specific expansion in terms of linear oscillation, proposed in Münchmeyer et al. (2015), it is possible to extend the frequency range of the analysis considerably. In this approach one exploits the fact that any bispectrum shape which is a function of $k_1 + k_2 + k_3$ can be expanded in Fourier modes of $k_1 + k_2 + k_3$, resulting in an effectively one-dimensional expansion, as opposed to the general Modal expansion. In the present implementation we use 800 sine and cosine modes, which cover the full frequency space of the power spectrum search, i.e., $0 < \omega < 1100$. The significances found with this method are presented in Fig. 25. As was the case for the feature model, we find that SMICA, SEVEM and NILC results are in good agreement in both temperature and polarization, while Commander results generally have larger variance and so are not included in the plotted averages. We find that the largest peak of the average is 3.6σ in temperature and 3.1σ in temperature and polarization combined. The results of the Modal expansion discussed in the previous paragraph are in good agreement with the high frequency resonance model estimator in the overlapping frequency range.

Due to the high computational demands of this analysis, we have only exactly assessed the look-elsewhere effect for SMICA T data, for which we find an expected maximum peak of $3.5\sigma \pm 0.4\sigma$ in the case of Gaussian maps, to be compared to 3.7σ in the SMICA T data, demonstrating that the results are fully consistent with Gaussianity. The expected maximum peak for Gaussian maps was calculated from the Fisher matrix with the method described in Meerburg et al. (2016). The average over component separation methods as well as the $T+E$ data is even less significant. For the high frequency estimator we have assessed the significance of multiple peaks in the following way. Define the multi-peak amplitude A_M as the sum of squares of the M highest significances σ_i in the frequency range, i.e., $A_M = \left(\sum_{i=1}^{M} \sigma_i^2\right)^{1/2}$, where only approximately independent peaks with $\Delta\omega > 10$ are considered. One can then compare A_M to its distribution in the Gaussian case and get an individual significance σ_M for each number of peaks M, where we assume $M \leq 10$. The multi-peak statistic is then obtained by maximizing over M, leading to an additional look-elsewhere effect that we also accounted for. In this way we find that in the SMICA T data the raw peak maximum 3.7σ, is reduced to 0.5σ for the single-peak statistic and to 0.6σ in the multi-peak case. This large reduction in significance is due to the

large number of independent frequencies as well as to the maximization over phases. One may argue that the frequency range $\omega < 1100$ is too large, as EFT arguments for resonance non-Gaussianities (Behbahani et al. 2012) limit the frequency range to $O(10^2)$. As an example, we have therefore also calculated the look-elsewhere-corrected significances when we limit the analysis to $\omega < 250$. In this case we find a single-peak significance of 0.6σ and a multi-peak significance of 0.9σ. Clearly the results are fully consistent with Gaussianity.

8.4. Equilateral-type models and the effective field theory of inflation

There is considerable interest in equilateral-type models because they are physically well-motivated, through e.g., varying sound speed scenarios. There are generic predictions available from the effective field theory of inflation, notably the two specific effective field theory (EFT1 and EFT2) shapes that give rise to the equilateral and orthogonal approximations. These models were previously constrained in Planck Collaboration XXIV (2014) and the reader is referred to Sect. 2 of that paper for analytic expressions for the specific shapes constrained here. In Table 23, we list the main equilateral-type models in the literature, giving constraints for T-only and $T+E$. All these models correlate well with the equilateral ansatz (Eq. (12)) and likewise do not show a significant signal. However, despite this correlation, it is interesting to note the variation between models, largely due to the difference between these shapes in the flattened limit. The implications of these results are discussed in Sect. 11.

8.5. Models with excited initial states (non-Bunch-Davies vacua)

Non-Bunch-Davies (NBD) or excited initial states are models which produce flattened (or squeezed) bispectrum shapes. The wide variety of NBD models that have been proposed are briefly classified and labelled in Sect. 2, following a more extensive overview in Sect. 2 of Planck Collaboration XXIV (2014) where more analytic forms and the first constraints were presented. The latest *Planck* constraints for these models are listed in Table 24, obtained using the Modal 2 estimator with polarization, Despite the apparent "flattened" signal seen in the *Planck* bispectrum reconstructions (Fig. 4), this is generally not matched well by the specific modulation induced by the acoustic peaks for these scale-invariant NBD models. Tight constraints emerge for most models. The largest signal obtained is from the NBD sinusoidal
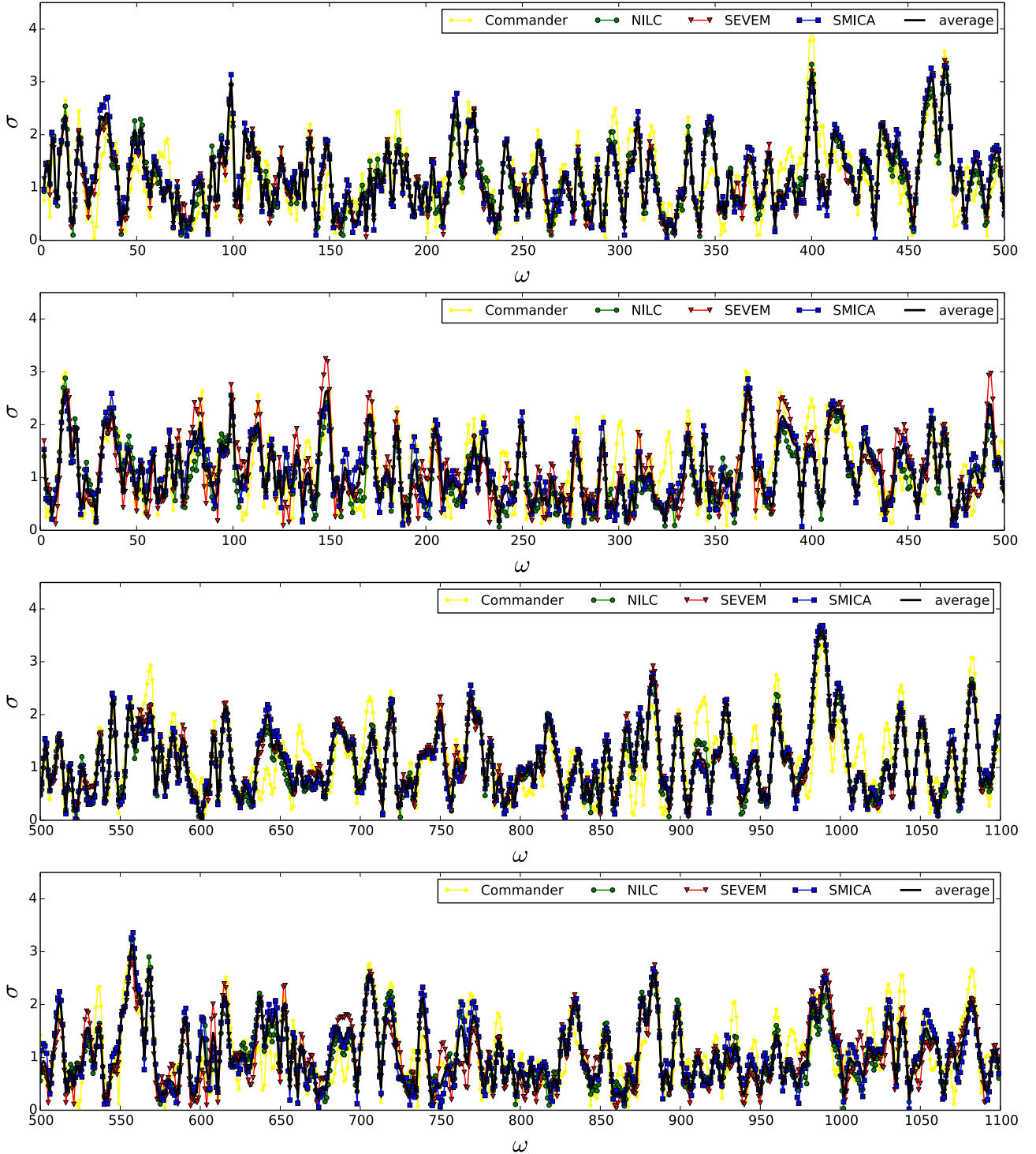
Fig. 25. Standard resonance model results for both T-only and $T+E$ across a wide frequency range using the high frequency resonance model estimator. The *first and second panels* show the signal in both T-only (*first panel*) and $T+E$ (*second panel*) across the frequency range $0 < \omega < 500$. The *lower two panels* give the results for T-only (*third panel*) and $T+E$ (*fourth panel*) in the range $500 < \omega < 1100$.

shape which gives a 1.6σ T-only raw significance, rising to 2.1σ for $T+E$; this is hardly an impressive correspondence given the number of models surveyed and the parameter freedom used in maximizing the signal. However, an important caveat for NBD models is that the predicted shapes can be very narrow in the flattened limit, in which case solutions have been smoothed to match the current Modal resolution (though this has improved considerably since the *Planck* 2013 NG analysis). An improved match to the warm inflation shape means that the final constraint

shown in Table 24 is more robust, with further implications discussed in Sect. 11.

8.6. Direction-dependent primordial non-Gaussianity

We impose observational limits on direction-dependent primordial NG parametrized by Eq. (23). Rather than using c_1 and c_2 we instead choose to work with the non-linearity parameters $f_{NL}^{L=1} = -c_1/4$ and $f_{NL}^{L=2} = -c_2/16$ (chosen to match a primordial

Table 23. Constraints on models with equilateral-type NG covering the shapes predicted by the effective field theory of inflation, together with constraints on specific non-canonical inflation models, such as DBI inflation.

	SMICA		SEVEM		NILC		Commander	
Equilateral-type model	$A \pm \sigma_A$	S/N	$A \pm \sigma_A$	S/N	$A \pm \sigma_A$	S/N	$A \pm \sigma_A$	S/N
Constant T-only	12 ± 38	0.3	16 ± 38	0.4	10 ± 37	0.3	1 ± 39	0.0
Constant $T+E$	18 ± 22	0.8	28 ± 24	1.2	12 ± 23	0.5	26 ± 24	1.1
Equilateral T-only	-15 ± 68	-0.2	-9 ± 68	-0.1	-19 ± 67	-0.3	-17 ± 69	-0.3
Equilateral $T+E$	5 ± 42	0.1	4 ± 45	0.1	-2 ± 42	-0.1	27 ± 45	0.6
EFT shape 1 T-only	-3 ± 65	0.0	3 ± 64	0.0	-7 ± 62	-0.1	-9 ± 66	-0.1
EFT shape 1 $T+E$	12 ± 39	0.3	15 ± 42	0.3	3 ± 39	0.1	32 ± 42	0.8
EFT shape 2 T-only	17 ± 50	0.3	22 ± 50	0.5	15 ± 47	0.3	8 ± 51	0.2
EFT shape 2 $T+E$	23 ± 29	0.8	31 ± 31	1.0	15 ± 29	0.5	36 ± 31	1.2
DBI inflation T-only	3 ± 62	0.0	9 ± 61	0.1	-1 ± 59	0.0	-4 ± 63	-0.1
DBI inflation $T+E$	15 ± 37	0.4	20 ± 39	0.5	7 ± 37	0.2	34 ± 40	0.9
Ghost inflation T-only	-50 ± 80	-0.6	-45 ± 80	-0.6	-54 ± 79	-0.7	-45 ± 82	-0.6
Ghost inflation $T+E$	-27 ± 50	-0.5	-37 ± 54	-0.7	-31 ± 51	-0.6	1 ± 55	0.0
Inverse decay T-only	17 ± 43	0.4	21 ± 43	0.5	14 ± 41	0.3	4 ± 44	0.1
Inverse decay $T+E$	23 ± 25	0.9	32 ± 27	1.2	15 ± 26	0.6	32 ± 27	1.2

Notes. See Planck Collaboration XXIV (2014) (Sect. 2) for further explanation of these specific models, with further implications discussed in Sect. 11.

Table 24. Constraints on models with excited initial states (non-Bunch-Davies models), as well as warm inflation.

	SMICA		SEVEM		NILC		Commander	
Flattened-type model	$A \pm \sigma_A$	S/N	$A \pm \sigma_A$	S/N	$A \pm \sigma_A$	S/N	$A \pm \sigma_A$	S/N
Flat model T-only	49 ± 65	0.8	57 ± 65	0.9	47 ± 65	0.7	19 ± 65	0.3
Flat model $T+E$	44 ± 37	1.2	70 ± 37	1.9	33 ± 37	0.9	47 ± 37	1.3
Non-Bunch-Davies T-only	42 ± 82	0.5	53 ± 82	0.6	26 ± 82	0.3	17 ± 82	0.2
Non-Bunch-Davies $T+E$	61 ± 47	1.3	76 ± 47	1.6	43 ± 47	0.9	58 ± 47	1.2
NBD sine T-only	567 ± 341	1.7	513 ± 341	1.5	588 ± 341	1.7	604 ± 341	1.8
NBD sine $T+E$	-387 ± 206	-1.9	-485 ± 218	-2.2	-425 ± 206	-2.1	-417 ± 210	-2.0
NBD1 cos flattened T-only	-10 ± 22	-0.5	-4 ± 22	-0.2	-8 ± 22	-0.4	-9 ± 22	-0.4
NBD1 cos flattened $T+E$	-20 ± 19	-1.1	-10 ± 19	-0.5	-19 ± 19	-1.0	-14 ± 19	-0.8
NBD2 cos squeezed T-only	10 ± 17	0.6	10 ± 17	0.6	8 ± 17	0.5	-2.5 ± 17	-0.1
NBD2 cos squeezed $T+E$	-3 ± 5	-0.5	-0.8 ± 5.5	-0.1	-4 ± 5	-0.8	-3.8 ± 5.5	-0.7
NBD1 sin flattened T-only	-25 ± 22	-1.1	-27 ± 22	-1.2	-18 ± 22	-0.8	-33 ± 23	-1.4
NBD1 sin flattened $T+E$	48 ± 30	1.6	49 ± 33	1.5	35 ± 31	1.1	26 ± 34	0.8
NBD2 sin squeezed T-only	-2.0 ± 1.4	-1.4	-1.4 ± 1.4	-1.0	-1.6 ± 1.4	-1.1	-1.3 ± 1.4	-0.9
NBD2 sin squeezed $T+E$	-0.8 ± 0.4	-1.9	-0.5 ± 0.4	-1.2	-0.6 ± 0.4	-1.4	-0.5 ± 0.4	-1.2
NBD3 non-canonical T-only ($\times 1000$)	-5.9 ± 6.7	-0.9	-6.0 ± 6.8	-0.9	-5.4 ± 6.8	-0.8	-5.5 ± 6.7	-0.8
NBD3 non-canonical $T+E$ ($\times 1000$)	-8.7 ± 5.0	-1.7	-6.2 ± 5.2	-1.2	-7.5 ± 5.2	-1.5	-9.4 ± 5.2	-1.8
WarmS inflation T-only	-23 ± 36	-0.6	-26 ± 36	-0.7	-32 ± 36	-0.9	-24 ± 36	-0.7
WarmS inflation $T+E$	-14 ± 23	-0.6	-28 ± 23	-1.2	-21 ± 23	-0.9	-17 ± 23	-0.7

Notes. See Sect. 2 for further explanation and the labelling of these classes of NBD models. Note that the NBD, NBD1, and NBD2 models contain free parameters, so here we quote the maximum significance found over the available parameter range; the maximum for T and $T+E$ can occur at different parameter values (on which the error bars are also dependent).

bispectrum that is equal to the equilateral shape in the equilateral limit) keeping the notation from the 2013 results. We estimated the f_{NL}^L values from temperature data and high-pass filtered polarization data from the four foreground-cleaned CMB maps SMICA, NILC, SEVEM, and Commander, where we apply the common mask. The details of the KSW estimator and its derivation is presented in Appendix A. For temperature data, we use the common mask as adopted in Planck Collaboration XII (2014), which has more conservative foreground masking than the newly available mask. We choose the more conservative foreground masking, considering the fact that anisotropic NG is more sensitive to residual foregrounds. We set the maximum multipole to 2000 and 1000 for temperature and polarization data, respectively. Validating our analysis pipeline with realistic simulations, we find that the asymmetry of the *Planck* beam, coupled with the

Planck scanning pattern, inflates the statistical fluctuations of the f_{NL}^L significantly. Noting the large angular scale of artificial anisotropy produced by the beam asymmetry, we set the minimum multipole to 101, and find that the statistical fluctuation of estimation from simulated data is close to the theoretical expectations.

These two shapes are also constrained using the Modal 2 estimator, which is not affected by the beam asymmetry and is used in the same form as elsewhere in the paper with multipoles from 2 to 2000 and 30 to 1500 being used for temperature and polarization, respectively. The present constraints are consistent with those found for T-only in Planck Collaboration XXIV (2014), but at higher resolution convergence has improved considerably, reflected in the lower variance.

Table 25. Direction-dependent NG results for both the $L = 1$ and $L = 2$ models.

	Commander		NILC		SEVEM		SMICA	
	$A \pm \sigma_A$	S/N	$A \pm \sigma_A$	S/N	$A \pm \sigma_A$	S/N	$A \pm \sigma_A$	S/N
$L = 1$								
Modal 2 T-only	-41 ± 43	-0.9	-58 ± 42	-1.4	-51 ± 43	-1.2	-49 ± 43	-1.1
KSW T-only	-8 ± 46	-0.2	-62 ± 46	-1.3	-34 ± 45	-0.8	-26 ± 45	-0.6
Modal 2 $T+E$	-28 ± 29	-1.0	-30 ± 27	-1.1	-49 ± 28	-1.7	-31 ± 26	-1.2
KSW $T+E$	-57 ± 33	-1.7	-62 ± 32	-1.9	-79 ± 32	-2.5	-54 ± 32	-1.7
$L = 2$								
Modal 2 T-only	0.7 ± 2.8	0.2	0.8 ± 2.8	0.4	1.1 ± 2.7	0.3	0.5 ± 2.7	0.2
KSW T-only	1.5 ± 5.1	0.3	-3.9 ± 5.1	-0.8	-0.4 ± 5.1	-0.1	0.1 ± 5.0	0.0
Modal 2 $T+E$	1.1 ± 2.4	0.5	0.5 ± 2.4	0.2	1.3 ± 2.4	0.6	-0.2 ± 2.3	-0.1
KSW $T+E$	-3.0 ± 4.1	-0.7	-3.6 ± 4.0	-0.9	-3.8 ± 4.0	-1.0	-1.3 ± 3.9	-0.3

Notes. We present results from both the KSW and Modal 2 pipelines. The discrepancy between the central values for the $L = 2$ models is due to the differing ℓ ranges taken for the two estimators, the key difference being the KSW $\ell_{\min} = 101$. As this model peaks in the squeezed configuration, a significant portion of the signal is lost, which is reflected in the increased error bars.

We find that the ISW-lensing bispectrum and the unresolved point-sources bispectrum bias the estimation of the $f_{\rm NL}^L$, in particular in the analysis of temperature data. For our final values, we subtract both these biases from our estimation. In Table 25, we report the estimated value of $f_{\rm NL}^L$ from the foreground-cleaned CMB maps. For $L = 1$ the effect of the differing ℓ-ranges between the two estimators is not so significant and the results are quite consistent. For $L = 2$, which has significant signal in the squeezed configuration, the effect of removing small scales from the KSW estimator is more pronounced, resulting in significantly enlarged error bars. In light of this, the differences seen between the central values for the two methods is to be expected and does not indicate any inconsistencies between the two approaches. The slight differences between the results from different foreground-cleaned temperature maps are within the likely range of statistical fluctuations, estimated from realistic simulations of CMB and noise propagated through the pipelines of foreground-cleaned map making. As seen in Table 25, we find that the estimated values of $f_{\rm NL}^L$ from *Planck* 2015 temperature plus polarization data are consistent with zero.

8.7. Parity-violating tensor non-Gaussianity

We present observational limits on the parity-violating tensor nonlinearity parameter $f_{\rm NL}^{\rm tens}$ from the temperature and E-mode polarization data. Unlike the usual scalar-mode templates, the CMB bispectra sourced from the tensor NG (Eq. (27)) are written in non-factorizable forms (Shiraishi et al. 2013b); hence, we use the separable Modal pipeline in our bispectrum estimations.

The parity-violating NG under examination induces non-vanishing signals not only in parity-even configurations ($\ell_1 + \ell_2 + \ell_3 =$ even) but also in the parity-odd ones ($\ell_1 + \ell_2 + \ell_3 =$ odd) in the temperature and E-mode polarization bispectra (Shiraishi et al. 2013b). The optimal estimator, including all (even + odd) bispectrum signals, is expressed by the linear combination of the parity-even and parity-odd estimators, reading (Liguori, in prep.)

$$\hat{f}_{\rm NL}^{\rm all} = \frac{N^{\rm even} \hat{f}_{\rm NL}^{\rm even} + N^{\rm odd} \hat{f}_{\rm NL}^{\rm odd}}{N^{\rm even} + N^{\rm odd}}, \tag{61}$$

where $N^{\rm even/odd}$ is the normalization factor (related to the Fisher matrix as $N^{\rm even/odd} = 6F^{\rm even/odd}$) defined for $\ell_1 + \ell_2 + \ell_3 =$ even/odd. The parity-even estimator $\hat{f}_{\rm NL}^{\rm even}$ can be computed using the original Modal methodology (Fergusson et al. 2010a, 2012; Fergusson 2014; Liguori, in prep.), while in computations of the parity-odd estimator $\hat{f}_{\rm NL}^{\rm odd}$, we follow the extended spin-weighted pipeline (Shiraishi et al. 2014, 2015; Liguori, in prep.).

Our $f_{\rm NL}^{\rm tens}$ estimations (with both temperature and polarization data) are based on the resolution of $\ell_{\max} = 500$ and HEALPix $N_{\rm side} = 512$, leading to feasible computational costs. This choice is not expected to change the results significantly, in comparison to the analysis at higher resolution, e.g., $\ell_{\max} = 2000$ and Healpix $N_{\rm side} = 2048$, since the cosmic variance and instrumental noise are already far higher than the signals for $\ell \gtrsim 300$ (Shiraishi et al. 2013b). Only in the polarization data analysis is an effective $\ell_{\min}$ also adopted, which is motivated by the high-pass filtering process for $\ell \leq 40$ in component separation.

Within the above ℓ ranges, the theoretical bispectrum templates are decomposed with the eigenbasis composed of $O(1-10)$ polynomials and some special functions reconstructing the tensor-mode features, e.g., temperature enhancement due to the ISW effect ($\ell \lesssim 100$), and two E-mode peaks created by reionization ($\ell \lesssim 10$) and recombination ($\ell \simeq 100$). The resulting factorized templates are more than 95% correlated with the original ones. The validity of our numerical computations has been confirmed through the map-by-map comparisons of $\hat{f}_{\rm NL}^{\rm even/odd}$ at very low resolution, showing the consistency between the values from the Modal methodology and those obtained by the brute-force $O(\ell^5)$ summations like Eq. (36). We have also checked that our parity-even estimator successfully leads to the constraints on $f_{\rm NL}^{\rm local}$, $f_{\rm NL}^{\rm equil}$, and $f_{\rm NL}^{\rm ortho}$ at $\ell_{\max} = 500$, compatible with the results from the binned estimator.

Our limits estimated from the foreground-cleaned temperature and high-pass filtered polarization data (SMICA, SEVEM, and NILC) are summarized in Table 26. The data and MC simulations used here, including all experimental features, i.e., beam, anisotropic noise levels and partial sky mask, have been inpainted using the identical recursive process adopted in the standard $f_{\rm NL}$ estimations (see Sect. 3.5). The sky fractions of the temperature and polarization masks adopted here are, respectively, $f_{\rm sky} = 0.76$ and $f_{\rm sky} = 0.74$. Although the error bars

Table 26. Results for the tensor nonlinearity parameter $f_{NL}^{tens}/10^2$, estimated from the SMICA, SEVEM, and NILC temperature and high-pass filtered polarization maps.

	Even	Odd	All
SMICA			
T	2 ± 15	120 ± 110	4 ± 15
$T+E$	0 ± 13		
SEVEM			
T	2 ± 15	120 ± 110	5 ± 15
$T+E$	4 ± 13		
NILC			
T	3 ± 15	110 ± 100	5 ± 15
$T+E$	1 ± 13		

Notes. We separately show the central values and the errors (68% CL) extracted from $\ell_1 + \ell_2 + \ell_3$ = even (Even), $\ell_1 + \ell_2 + \ell_3$ = odd (Odd) and their whole domain (All). The parity-odd constraints have also been obtained from the *E*-mode data, but they are still preliminary and not currently shown.

Table 27. Correlation coefficients between pairs of bispectrum modes, extracted from two of the *Planck* component separated maps and the WMAP foreground-cleaned map at $\ell_{max} = 500$ resolution.

	TTT		*EEE*	
Methods	Even	Odd	Even	Odd
SMICA–SEVEM ..	1.00	0.99	0.80	0.80
SMICA–NILC ...	1.00	1.00	0.90	0.87
SEVEM–NILC ...	0.99	1.00	0.70	0.60
SMICA–WMAP .	0.75	0.67	...	...

Notes. We separately present the results estimated from $\ell_1 + \ell_2 + \ell_3$ = even (Even) and $\ell_1 + \ell_2 + \ell_3$ = odd (Odd) combinations. The loss of the correlations is confirmed in the *EEE* case, like Table 14.

and the linear terms have been computed using 160 MC simulations, the resulting error bars are close to the expected values, $(f_{sky}F)^{-1/2}$.

We have confirmed the stability of the *T*-only constraints, and significant scatter of the *E*-only constraints both in the parity-even case and in the parity-odd one, when changing f_{sky}. Such *E*-mode instability has given insignificant effects on our *T+E* constraints in the parity-even case, as they are determined almost exclusively by *TTT*, like the scalar NG analyses. In contrast, our parity-odd *T+E* results vary a lot, due to the *E*-mode scatter (quantitatively speaking, only a few percent change of f_{sky} has shifted f_{NL}^{tens} by more than 1σ), because *TTE* and *TEE* contribute significantly to the signal-to-noise ratio in the parity-odd case (Shiraishi et al. 2013b). Table 27 presents the correlations of the bispectra reconstructed from the component separated maps, also indicating the robustness of the *T*-only constraints and the instability of the *E*-only results. We report only stable results in Table 26 and conclude that there is no evidence at $>2\sigma$ of f_{NL}^{tens} in the parity-even, parity-odd or their whole domain.

The parity-odd components of the *TTT* and *EEE* bispectra extracted model-independently from the SMICA data are visually
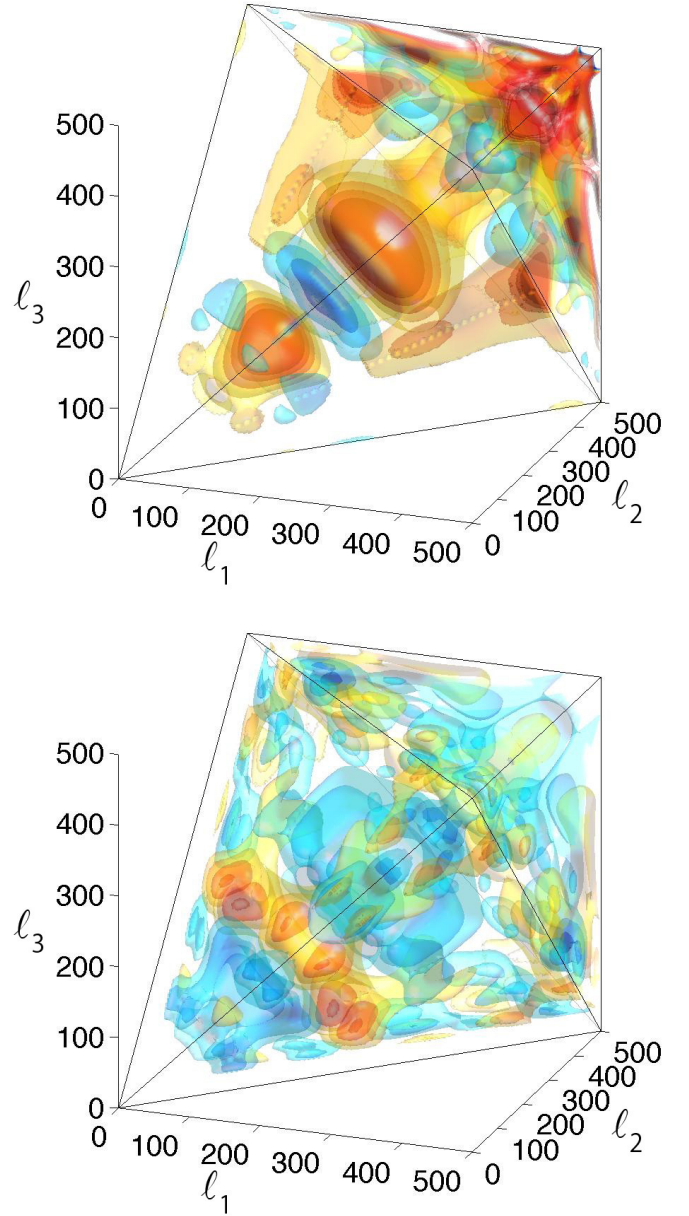
Fig. 26. Parity-odd signals ($\ell_1 + \ell_2 + \ell_3$ = odd) of the *TTT* (*top*) and *EEE* (*bottom*) bispectra ($\ell_i \leq 500$) recovered from the SMICA maps by means of the Modal decomposition with 101 simple polynomial-based eigenmodes, not including any special functions fitting the CMB tensor-mode features. In the panel for *EEE*, only the signals larger than $\ell = 40$ are shown. The *TTT* and *EEE* bispectra shown here are rescaled with a constant Sachs-Wolfe weighting and signal-to-noise weighting, respectively.

represented in Fig. 26. It is apparent from this figure that the *Planck TTT* bispectrum has similar features to the WMAP one (Shiraishi et al. 2015), e.g., distinctive signals distributed around $\ell_1 \approx \ell_2 \approx \ell_3$. As indicated by the roughly 70% correlation between the SMICA and WMAP bispectra (see Table 27), the *Planck T*-only limits in Table 26 are close to the WMAP ones (68% CL): $f_{NL}^{tens}/10^2 = 4 \pm 16$ for parity-even; and $f_{NL}^{tens}/10^2 = 80 \pm 110$ for parity-odd (Shiraishi et al. 2015).

9. Limits on the primordial trispectrum

So far, we have considered a variety of physically motivated possibilities for the inflationary 3-point function, or bispectrum. A similar phenomenology exists for the 4-point function, or trispectrum. Our constraints on the trispectrum will use CMB temperature only; we do not use polarization in this section. We start by briefly reviewing the inflationary physics and classifying the signals we will search for.

First, some notation: a "primed" ζ-trispectrum $\langle \zeta_{k_1} \zeta_{k_2} \zeta_{k_3} \zeta_{k_4} \rangle'$ denotes the connected trispectrum without its momentum-conserving delta function, i.e.,

$$\langle \zeta_{k_1} \zeta_{k_2} \zeta_{k_3} \zeta_{k_4} \rangle = \langle \zeta_{k_1} \zeta_{k_2} \zeta_{k_3} \zeta_{k_4} \rangle' (2\pi)^3 \delta^{(3)}\left(\sum k_i\right) + \text{disc.}, \quad (62)$$

where "+ disc." denotes the disconnected contributions to the 4-point function.

One possible signal is the "local" trispectrum $g_{\mathrm{NL}}^{\mathrm{local}}$, which arises if the non-Gaussian adiabatic curvature ζ is of cubic-type form (see, e.g., Okamoto & Hu 2002), i.e.,

$$\zeta(x) = \zeta_G(x) + \frac{9}{25} g_{\mathrm{NL}}^{\mathrm{local}} \zeta_G(x)^3 \quad (63)$$

where $g_{\mathrm{NL}}^{\mathrm{local}}$ is a free parameter and ζ_G is a Gaussian field. In this model, the bispectrum is zero (since there is a $\zeta \to -\zeta$ symmetry) and the trispectrum is given by

$$\langle \zeta_{k_1} \zeta_{k_2} \zeta_{k_3} \zeta_{k_4} \rangle' = \frac{54}{25} g_{\mathrm{NL}}^{\mathrm{local}} \left[P_\zeta(k_1) P_\zeta(k_2) P_\zeta(k_3) + 3 \text{ perm.} \right]. \quad (64)$$

Analogously to the case of the local bispectrum, $f_{\mathrm{NL}}^{\mathrm{local}}$, the observational signal-to-noise for $g_{\mathrm{NL}}^{\mathrm{local}}$ is largest in the "squeezed" limit, $k_1 \ll \min(k_2, k_3, k_4)$, and there is a consistency relation which shows that in single-field inflation, the four-point function is always small in the squeezed limit (e.g., Senatore & Zaldarriaga 2012a). Thus $g_{\mathrm{NL}}^{\mathrm{local}}$ can only be detectably large in multi-field models. Conversely, there are multi-field models where $g_{\mathrm{NL}}^{\mathrm{local}}$ is detectable. The main obstacle here is technical naturalness, i.e., ensuring that radiative corrections do not generate an observationally larger bispectrum. This can be the case if a large bispectrum is forbidden by a Z_2 symmetry, or by supersymmetry (Senatore & Zaldarriaga 2012b).

A further category of four-point signals can be obtained by adding quartic interactions to the inflationary action. Following Smith et al. (2015), we will concentrate on the simplest possibility, by considering quartic operators consistent with the symmetries of inflation and having the lowest possible number of derivatives (Bartolo et al. 2010b; Senatore & Zaldarriaga 2011, 2012b). There are three such operators, of the schematic form $\dot{\sigma}^4$, $\dot{\sigma}^2(\partial_i \sigma)^2$, and $(\partial_i \sigma)^2(\partial_j \sigma)^2$. By a short calculation using the in-in formalism (Maldacena 2003), the associated four-point functions are (Smith et al. 2015; see also

Huang & Shiu 2006):

$$\langle \zeta_{k_1} \zeta_{k_2} \zeta_{k_3} \zeta_{k_4} \rangle' = \frac{9216}{25} g_{\mathrm{NL}}^{\dot{\sigma}^4} A_\zeta^3 \int_{-\infty}^{0} \mathrm{d}\tau_E\, \tau_E^4 \left(\prod_{i=1}^{4} \frac{e^{k_i \tau_E}}{k_i} \right)$$
$$= \frac{221\,184}{25} g_{\mathrm{NL}}^{\dot{\sigma}^4} A_\zeta^3 \frac{1}{k_1 k_2 k_3 k_4 K^5}; \quad (65)$$

$$\langle \zeta_{k_1} \zeta_{k_2} \zeta_{k_3} \zeta_{k_4} \rangle' = -\frac{13\,824}{325} g_{\mathrm{NL}}^{\dot{\sigma}^2(\partial\sigma)^2} A_\zeta^3 \int_{-\infty}^{0} \mathrm{d}\tau_E\, \tau_E^2$$
$$\times \left[\frac{(1 - k_3 \tau_E)(1 - k_4 \tau_E)}{k_1 k_2 k_3^3 k_4^3} (k_3 \cdot k_4) e^{\sum k_i \tau_E} \right.$$
$$\left. + 5 \text{ perm.} \right]$$
$$= -\frac{27\,648}{325} g_{\mathrm{NL}}^{\dot{\sigma}^2(\partial\sigma)^2} A_\zeta^3$$
$$\times \left[\frac{K^2 + 3(k_3 + k_4)K + 12 k_3 k_4}{k_1 k_2 k_3^3 k_4^3 K^5} (k_3 \cdot k_4) \right.$$
$$\left. + 5 \text{ perm.} \right]; \quad (66)$$

$$\langle \zeta_{k_1} \zeta_{k_2} \zeta_{k_3} \zeta_{k_4} \rangle' = \frac{82\,944}{2575} g_{\mathrm{NL}}^{(\partial\sigma)^4} A_\zeta^3 \int_{-\infty}^{0} \mathrm{d}\tau_E$$
$$\times \left[\prod_{i=1}^{4} \frac{(1 - k_i \tau_E) e^{k_i \tau_E}}{k_i^3} \right]$$
$$\times \left[(k_1 \cdot k_2)(k_3 \cdot k_4) + 2 \text{ perm.} \right]$$
$$= \frac{165\,888}{2575} g_{\mathrm{NL}}^{(\partial\sigma)^4} A_\zeta^3$$
$$\times \left(\frac{2K^4 - 2K^2 \sum k_i^2 + K \sum k_i^3 + 12 k_1 k_2 k_3 k_4}{k_1^3 k_2^3 k_3^3 k_4^3 K^5} \right)$$
$$\times \left[(k_1 \cdot k_2)(k_3 \cdot k_4) + 2 \text{ perm.} \right]. \quad (67)$$

Here $K = \sum k_i$ and we have introduced parameters $g_{\mathrm{NL}}^{\dot{\sigma}^4}$, $g_{\mathrm{NL}}^{\dot{\sigma}^2(\partial\sigma)^2}$, and $g_{\mathrm{NL}}^{(\partial\sigma)^4}$ to parametrize the amplitude of each trispectrum.

The normalization of the g_{NL}-parameters is chosen so that $\langle \zeta_{k_1} \zeta_{k_2} \zeta_{k_3} \zeta_{k_4} \rangle = (216/25) g_{\mathrm{NL}} A_\zeta^3/k^9$ for "tetrahedral" configurations, with $|k_i| = k$ and $(k_i \cdot k_j) = -k^3/3$. This is the analogue of the commonly-used normalization for the bispectrum, where f_{NL} parameters are defined so that $\langle \zeta_{k_1} \zeta_{k_2} \zeta_{k_3} \rangle = (18/5) f_{\mathrm{NL}} A_\zeta^2/k^6$ for equilateral configurations with $|k_i| = k$.

For simplicity in Eqs. (65)–(67) we have assumed a scale-invariant initial power spectrum $P_\zeta(k) = A_\zeta/k^3$. In order to analyse *Planck* data, we must slightly generalize this to a power-law spectrum $P_\zeta(k) \propto k^{n_s - 4}$. Our scheme for doing this follows Appendix C of Smith et al. (2015).

A Fisher matrix analysis shows that there is one large correlation among the three trispectra in Eqs. (65)–(67), so that to an excellent approximation we can treat only two of the trispectra as independent. To quantify this, in Smith et al. (2015) it is shown that the $\dot{\sigma}^2(\partial\sigma)^2$ shape is 98.6 % correlated to a linear combination of the shapes $\dot{\sigma}^4$ and $(\partial\sigma)^4$. Therefore, we will only search for the parameters $g_{\mathrm{NL}}^{\dot{\sigma}^4}$ and $g_{\mathrm{NL}}^{(\partial\sigma)^4}$.

We note that the analysis that leads to the trispectrum shapes $g_{\mathrm{NL}}^{\dot{\sigma}^4}$ and $g_{\mathrm{NL}}^{(\partial\sigma)^4}$ is very similar to the analysis that leads to the "standard" bispectrum shapes $f_{\mathrm{NL}}^{\mathrm{equi}}$ and $f_{\mathrm{NL}}^{\mathrm{ortho}}$. However, there are some minor differences as follows. In the bispectrum case, one considers the cubic operators $\dot{\pi}^3$ and $\dot{\pi}(\partial\pi)^2$, but it is conventional to define observables $f_{\mathrm{NL}}^{\mathrm{equi}}, f_{\mathrm{NL}}^{\mathrm{ortho}}$ which are related to

Table 28. Number of factorizable terms $N_{\rm in}$ needed to represent each trispectrum by direct sampling of the integral, and number of terms $N_{\rm out}$ obtained after running the optimization algorithm from Sect. VII of Smith et al. (2015).

Trispectrum	$N_{\rm in}$	$N_{\rm out}$
$g_{\rm NL}^{\rm local}$	436	17
$\dot\sigma^4$	6955	73
$(\partial\sigma)^4$	20 865	192

the operator coefficients by a linear transformation. This is done because the two cubic operators are about 90 % correlated, so it is convenient to orthogonalize. In the trispectrum case the correlation is smaller (around 60 % for *Planck*), and we have chosen to omit the orthogonalization step. Another reason to omit the orthogonalization step is that the trispectrum shape $(\partial\sigma)^4$ is a signature of multi-field inflation. In single field inflation, the $(\partial\sigma)^4$ trispectrum is not technically natural; radiative corrections generate cubic operators of the form $\dot\pi^3$ and $\dot\pi(\partial\pi)^2$, which generate a bispectrum with larger signal-to-noise.

There are more trispectrum shapes one might consider. For example, classifying Galilean invariant quartic operators leads to higher-derivative trispectra, which are not highly correlated to the trispectra considered above (Bartolo et al. 2013c; Arroja et al. 2013). We have only considered "contact" diagrams arising from one power of a quartic operator, and it would be interesting to study "exchange" diagrams arising from two cubic operators and exchange of a light particle (e.g., Chen et al. 2009; Arroja et al. 2009; Chen & Wang 2010; Bartolo et al. 2010a; Baumann & Green 2012). We leave these as extensions for future work.

Summarizing, we will search for the following trispectrum signals:

$$\left\{ g_{\rm NL}^{\rm local}, g_{\rm NL}^{\dot\sigma^4}, g_{\rm NL}^{(\partial\sigma)^4} \right\} \tag{68}$$

defined by Eqs. (64), (65), and (67) above.

9.1. Data analysis

Turning now to data analysis, we use the machinery from Smith et al. (2015). The first step is to represent each trispectrum as a small sum of factorizable terms as follows. The angular CMB trispectrum can be written either as an integral over comoving distance r (in the case of $g_{\rm NL}^{\rm local}$) or as a double integral over (τ, r) where τ is conformal time during inflation (in the case of the $\dot\sigma^4$ or $(\partial\sigma)^4$ trispectra). We approximate the integral by a finite sum, which represents the CMB trispectrum as a sum of terms that are factorizable in a sense defined in Smith et al. (2015). A large number of sampling points are needed to obtain a good approximation to the integral, leading to a large number of terms in the factorizable representation. However, there exists an optimization algorithm, which takes as input a trispectrum that has been represented as a sum of many factorizable terms, and outputs a representation with fewer terms. The reduction can be quite dramatic, as shown in Table 28. The optimization algorithm guarantees that the output trispectrum accurately approximates the input trispectrum, in the sense that the two are nearly observationally indistinguishable.

Armed with "small" factorizable representations for each trispectrum, the next step is to run an analysis pipeline that estimates the amplitude of each trispectrum from *Planck* data.

We use the "pure MC" pipeline from Smith et al. (2015), which compares the trispectrum of the data to the mean trispectrum of an ensemble of simulations. This pipeline requires a filtering operation $d \rightarrow \tilde{a}_{\ell m}$ which processes the pixel-space CMB data d and generates a harmonic-space map $\tilde{a}_{\ell m}$. Our filtering operation is defined by the following steps:

1. Starting from the data d, we compute (with uniform pixel weighting) a best-fit monopole and dipole outside the Galactic mask. We use the temperature "common mask", the union of the confidence masks for the `SMICA`, `SEVEM`, `NILC`, and `Commander` component separation methods (Planck Collaboration IX 2016).
2. The mask defines a few "islands", i.e., isolated groups of pixels that are unmasked, but contained in a larger masked region. We slightly enlarge the mask so that it removes the islands.
3. We classify the components of the masked part of the sky into "small" masked regions with ≤1000 pixels (at `HEALPix` resolution $N_{\rm side} = 2048$), and "large" regions with >1000 pixels. Small regions usually correspond to point sources, and large regions typically correspond to areas of diffuse galactic emission. In small regions, we inpaint the CMB by assigning the unique map that agrees with the data on boundary pixels, and whose value in each interior pixel is the average of the neighboring pixels.
4. In large regions, we do not inpaint the CMB, but rather apodize the boundary of the large region using cosine apodization with 12′ radius.
5. We apply a spherical harmonic transform to the inpainted, apodized CMB map to obtain a harmonic-space map $a_{\ell m}$ with $\ell_{\rm max} = 1600$. We then take the final filtered map $\tilde{a}_{\ell m}$ to be

$$\tilde{a}_{\ell m} = \frac{a_{\ell m}}{b_\ell C_\ell + b_\ell^{-1} N_\ell} \tag{69}$$

where b_ℓ is the beam, C_ℓ is the fiducial CMB power spectrum, and N_ℓ is the sky-averaged noise power spectrum (without beam deconvolution). To motivate this choice of ℓ-weighting, we note that for an ideal all-sky experiment with isotropic noise, we have $a_{\ell m} = b_\ell s_{\ell m} + n_{\ell m}$ where $s_{\ell m}, n_{\ell m}$ are signal and noise realizations. In this case, Eq. (69) weights the signal as $s_{\ell m}/(C_\ell + b_\ell^{-2} N_\ell)$, which is optimal.

In our pipeline, we apply this filter to the component-separated `SMICA` maps (Planck Collaboration IX 2016), obtaining a harmonic-space map $\tilde{a}_{\ell m}$. We apply the same filter to 1000 Monte Carlo simulations to obtain an ensemble of harmonic-space maps. Our pipeline has the property that it always estimates the trispectrum of the data in excess of the trispectrum in the simulations. Since the simulations include lensing, this means that lensing bias will automatically be subtracted from our $g_{\rm NL}$ estimates.

Now that the filter, data realization, and Monte Carlo simulations have been fully specified, the details of the pipeline are described in Sect. IX.B of Smith et al. (2015). For each trispectrum, the pipeline outputs an estimate of $g_{\rm NL}$ and an estimate of the statistical error. Our basic results are:

$$g_{\rm NL}^{\rm local} = (-9.0 \pm 7.7) \times 10^4;$$
$$g_{\rm NL}^{\dot\sigma^4} = (-0.2 \pm 1.7) \times 10^6; \tag{70}$$
$$g_{\rm NL}^{(\partial\sigma)^4} = (-0.1 \pm 3.8) \times 10^5.$$

No deviation from Gaussian statistics is seen. These results significantly improve the previous best constraints on the trispectrum from WMAP (Vielva & Sanz 2010; Smidt et al. 2010; Fergusson et al. 2010b; Hikage & Matsubara 2012; Sekiguchi & Sugiyama 2013; Regan et al. 2013; Smith et al. 2015) and large-scale structure (Desjacques & Seljak 2010; Giannantonio et al. 2014; Leistedt et al. 2014).

A constraint on g_{NL}^{local} from *Planck* 2013 data was recently reported by Feng et al. (2015), who find $g_{NL}^{local} = (-13 \pm 18) \times 10^4$. Our central value in Eq. (70) agrees well with this result, but the statistical error is smaller by a factor of 2.3. This improvement is partly due to the lower noise levels in *Planck* 2015 data, and partly due to the use of a better estimator.

Each line in Eq. (70) is a "single-g_{NL}" constraint; i.e., the constraint on one g_{NL} parameter with the other g_{NL}-parameters held fixed. For joint constraints, one needs to know the full covariance matrix. The correlation between g_{NL}^{local} and the other two parameters is negligble, and the $g_{NL}^{\dot{\sigma}^4}$-$g_{NL}^{(\partial\sigma)^4}$ correlation is:

$$\text{Corr}\left(g_{NL}^{\dot{\sigma}^4}, g_{NL}^{(\partial\sigma)^4}\right) = 0.61. \tag{71}$$

Multi-field models of inflation will generally give a linear combination of $\dot{\sigma}^4$, $\dot{\sigma}^2(\partial_i\sigma)^2$, and $(\partial_i\sigma)^2(\partial_j\sigma)^2$ trispectra. In this case we proceed as follows. First, if the $\dot{\sigma}^2(\partial_i\sigma)^2$ coefficient is non-zero, we can use the near-degeneracy with a linear combination of the other two operators to absorb it into the effective values of $g_{NL}^{\dot{\sigma}^4}$ and $g_{NL}^{(\partial\sigma)^4}$. A Fisher matrix analysis shows that the coefficients of this linear combination are

$$(g_{NL}^{\dot{\sigma}^4})_{\text{eff}} = 0.59 \, g_{NL}^{\dot{\sigma}^2(\partial\sigma)^2}$$
$$(g_{NL}^{(\partial\sigma)^4})_{\text{eff}} = 0.091 \, g_{NL}^{\dot{\sigma}^2(\partial\sigma)^2}. \tag{72}$$

It is convenient to define the two-component parameter vector:

$$g_i = \begin{pmatrix} g_{NL}^{\dot{\sigma}^4} \\ g_{NL}^{(\partial\sigma)^4} \end{pmatrix}. \tag{73}$$

We also compute a two-by-two Fisher matrix F_{ij}, whose diagonal is given by $F_{ii} = 1/\sigma_i^2$, where σ_i is the single-g_{NL} statistical error in Eq. (70), and whose off-diagonal is $F_{12} = r F_{11}^{1/2} F_{22}^{1/2}$, where r is the correlation in Eq. (71). This procedure gives:

$$F_{ij} = \begin{pmatrix} 3.3 & 9.2 \\ 9.2 & 68.7 \end{pmatrix} \times 10^{-13}. \tag{74}$$

For a given parameter vector g_i, we can define a trispectrum-χ^2 by

$$\chi^2(g) = [F_{ii}\hat{g}_i - (Fg)_i] \, F_{ij}^{-1} \, [F_{jj}\hat{g}_j - (Fg)_j] \tag{75}$$

where $\hat{g}_i = (-0.21 \times 10^6, -0.10 \times 10^5)$ is the vector of best-fit single-g_{NL} values from Eq. (70). This definition of χ^2 follows from the observation that $(F_{ii}\hat{g}_i)$ is an estimator with expectation value $(Fg)_i$ and covariance matrix $\text{Cov}(F_{ii}\hat{g}_i, F_{jj}\hat{g}_j) = F_{ij}$.

The inflationary implications of these trispectrum constraints are discussed in Sect. 11.5 below.

10. Minkowski functionals results

In this section, we present constraints on local NG at first and second order (f_{NL}^{local} and g_{NL}^{local}) obtained with Minkowski functionals (MFs) on temperature and polarization

E maps. MFs (Mecke et al. 1994; Schmalzing & Buchert 1997; Schmalzing & Gorski 1998; Winitzki & Kosowsky 1998) are a measure of fields' local morphology used to constrain their stationarity, isotropy and Gaussianity. Mostly probing general NG in a frequentist fashion in two-dimensions on CMB maps (Eriksen et al. 2004; Komatsu et al. 2005; Modest et al. 2013; Natoli et al. 2010; Curto et al. 2008) or three-dimensions on LSS data (Park et al. 2005; Wiegand et al. 2014), they have also been used to measure specific NG targets with Bayesian methods, such as f_{NL}^{local} (Hikage et al. 2006, 2008; Ducout et al. 2013; Planck Collaboration XXIV 2014), other bispectrum and trispectrum shapes (Hikage & Matsubara 2012) and topological defects (Planck Collaboration XXV 2014). New developments have been made recently, using needlets (Fantaye et al. 2015), neural networks (Novaes et al. 2015) or allowing scale-dependent measurements (Munshi et al. 2013).

MF-based limits are well known to be suboptimal for f_{NL}^{local} and g_{NL}^{local}, but they provide an independent cross-check of bispectrum and trispectrum-based estimators. They are complementary to optimal estimators: they are weighted integrals of the polyspectra and are sensitive to any source of NG, including foregrounds and secondaries. While MFs are not always able to distinguish between these different sources and systematics, they allow upper bounds to be put on them.

The most recent constraints (1σ) from MFs on f_{NL}^{local} and g_{NL}^{local} have been obtained with WMAP (Hikage & Matsubara 2012) and *Planck* (Planck Collaboration XXIV 2014):

$$f_{NL}^{local} = 4.2 \pm 20.5; \qquad g_{NL}^{local} = (1.9 \pm 6.4) \times 10^5. \tag{76}$$

10.1. Method and definition of MFs

For a smoothed two-dimensional field δ of zero mean and of variance σ_0^2, defined on the sphere, we consider an excursion set of height $\nu = \delta/\sigma_0$, i.e., the set of points where the field exceeds the threshold ν. We use four functionals denoted by $V_k(\nu)(k = 0, 1, 2, 3)$. The first three correspond to MFs: V_0 is the fractional *Area* of the regions above the threshold, V_1 is the *Perimeter* of these regions and V_2 is the *Genus*, defined as the total number of connected components of the excursion above the threshold minus the total number of connected components under the threshold. The fourth, V_3, is the *Number* of clusters (also referred to as N_{clusters}). This is the number of connected regions above the threshold for positive thresholds and below the threshold for negative thresholds. Precise definitions and formulae for the quantities V_k as well as their expectation values for Gaussian fields are summarized in Appendix B.

We calculate the four normalized[18] functionals $v_k(\nu)$ on $n_{\text{th}} = 26$ thresholds ν, between $\nu_{\min} = -3.5$ and $\nu_{\max} = +3.5$.

For this analysis, we used the same temperature and polarization E data, simulations and masks described in Sect. 3.4 for consistency with the bispectrum estimators. In addition, the maps are filtered to optimize constraints on local NG (Ducout et al. 2013), the filters used being similar to Wiener filters for T and E (W_M), and for the first (W_{D1}) and second (W_{D2}) derivatives of these fields (Fig. 27):

$$W_{D1} \propto \sqrt{\ell(\ell+1)} \, W_M; \tag{77}$$
$$W_{D2} \propto \ell(\ell+1) \, W_M. \tag{78}$$

---

[18] Raw Minkowski functionals V_k depend on the Gaussian part of fields through a normalization factor A_k, a function only of the shape of the power spectrum. We therefore normalize functionals $v_k = V_k/A_k$ to focus on NG, see Appendix B.
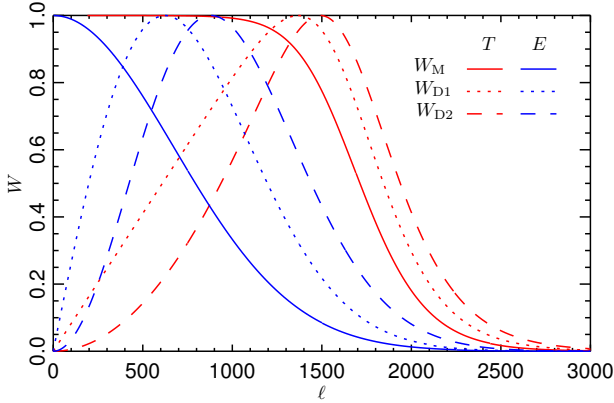
Fig. 27. Filters used to optimize constraints on local NG, in harmonic space. The temperature filter W_M is a smoothed version of the true Wiener filter obtained with realistic models, while the E-mode W_M filter is adapted from the temperature one, with a cutoff value at $\ell \simeq 800$. The formulae for the derivative filters are given in Eq. (78).

For the temperature map, known point sources in the mask are inpainted.

We define the vector y as any combination $y = \{v_k^{A,W}\}$ with $k = \{0, 3\}$, $A = \{T, E\}$, $W = \{W_M, W_{D1}, W_{D2}\}$, $\hat{y}$ being the vector measured on the data.

From these measurements, we then use a Bayesian method to jointly estimate f_{NL}^{local} and g_{NL}^{local},

$$P(f_{NL}^{local}, g_{NL}^{local} | \hat{y}) =$$
$$\frac{P(\hat{y} | f_{NL}^{local}, g_{NL}^{local}) P(f_{NL}^{local}, g_{NL}^{local})}{\int P(\hat{y} | f_{NL}^{local}, g_{NL}^{local}) P(f_{NL}^{local}, g_{NL}^{local}) \mathrm{d}f_{NL}^{local} \mathrm{d}g_{NL}^{local}}. \quad (79)$$

We take a uniform prior for f_{NL}^{local} in the range -400 to 400, and for g_{NL}^{local} in the range -4×10^6 to $+4 \times 10^6$, while the evidence is just considered as a normalization.

Assuming MFs are multi-variate Gaussian-distributed we obtain the posterior distribution for $(f_{NL}^{local}, g_{NL}^{local})$ with a χ^2 test

$$P(f_{NL}^{local}, g_{NL}^{local} | \hat{y}) \propto \exp\left[-\frac{\chi^2(\hat{y}, f_{NL}^{local}, g_{NL}^{local})}{2}\right], \quad (80)$$

with

$$\chi^2(\hat{y}, f_{NL}^{local}, g_{NL}^{local}) \equiv$$
$$\left[\hat{y} - \bar{y}_{\mathrm{sim1}}(f_{NL}^{local}, g_{NL}^{local})\right]^T C_{\mathrm{sim2}}^{-1} \left[\hat{y} - \bar{y}_{\mathrm{sim1}}(f_{NL}^{local}, g_{NL}^{local})\right]. \quad (81)$$

For this test, we use two types of simulations to first construct a model including primordial NG $\bar{y}_{\mathrm{sim1}}(f_{NL}^{local}, g_{NL}^{local})$ and secondly a covariance matrix

$$C_{\mathrm{sim2}} \equiv \left\langle (y_{\mathrm{sim2}} - \bar{y}_{\mathrm{sim2}})(y_{\mathrm{sim2}} - \bar{y}_{\mathrm{sim2}})^T \right\rangle, \quad (82)$$

with $\bar{y}_{\mathrm{sim}} \equiv \langle y_{\mathrm{sim}} \rangle_{\mathrm{sim}}$ averaged over the simulations. We now describe the details of these simulations.

– *Simulations 1*: *Non-Gaussian model*
For the first type of simulation, we included all possible sources of NG, assuming that the total and individual levels of NG are small enough that MFs are linear with respect to those NG levels (Ducout et al. 2013). The three kinds of NG we included are foreground residuals (Galactic residuals with scalable amplitude α, as well as radio sources,

CIB anisotropies, secondaries (SZ, lensing and ISW-lensing, but not SZ-lensing) and primordial NG (f_{NL}^{local}, g_{NL}^{local}):

$$\mathrm{sim1}^i = \mathrm{map}_{\mathrm{lensed}}^i(f_{NL}^{local}, g_{NL}^{local})$$
$$+ \mathrm{map}^{\mathrm{fg}}(\text{radio sources, CIB, SZ})$$
$$+ \alpha \times \mathrm{map}^{\mathrm{fg}}(\text{Galactic residuals}). \quad (83)$$

We tried to reproduce all instrumental effects, with realistic effective beams (isotropic window functions), noise from FFP8 simulations (Planck Collaboration XII 2016), filtered with component separation weights. We checked the accuracy of these simulations by comparing them to FFP8 simulations, using no foreground and no primordial NG. The astrophysical models are provided by the *Planck Sky Model* (PSM, Delabrouille et al. 2013), while the primordial NG simulations are computed as in Elsner & Wandelt (2009). The lensing uses LensPix[19]. The power spectrum used for these NG simulations and the lensing is the best-fit power spectrum from *Planck* 2013+ACT/SPT+BAO (Planck Collaboration XXII 2014). We created $n_1 = 200$ simulations i, using n_1 maps for the primordial NG, while we had only one astrophysical foreground simulation.

– *Simulations 2*: *FFP8 (Planck Collaboration XII 2016) MC simulations*
Since NG is weak, the covariance matrix C is computed with $n_2 = 10^4$ simulations, including no primordial NG and no foregrounds. These simulations reproduce realistic instrumental effects (anisotropy of beams in particular), realistic noise and component separation filtering. The only NG still present in these simulations are lensing and the ISW-lensing correlation.

Validation of the estimator

Part of the validation for the MFs estimator is described in Sect. 5.3 for f_{NL}^{local}, to compare the results to bispectrum estimators on realistic simulations (FFP8 MC, second item above). In addition we present in Table 29 the results obtained on the same realistic simulations for g_{NL}^{local}, and on simulations containing primordial NG (first item above), with $f_{NL}^{local} = 10$ and $g_{NL}^{local} = 10^5$, with 200 simulations used in each case. These tests have been performed using the SMICA method with lensing bias removed.

10.2. Results

Results for f_{NL}^{local} and g_{NL}^{local} estimation with MFs on the four component separated maps in temperature and polarization are presented in Table 30. The results for polarization E-only maps are not quoted, since these results were not sufficiently stable (cf. Sect. 7.6). No deviation from Gaussianity is detected. $T+E$ analysis generally finds higher values for f_{NL}^{local}, but remains consistent with Gaussianity.

The posteriors for f_{NL}^{local} and g_{NL}^{local} from SMICA are shown in Fig. 28. One interesting point is that the estimates of f_{NL}^{local} and g_{NL}^{local} are almost uncorrelated ($r < 0.1$); this can be inferred when we consider the parity of MF deviations from Gaussianity, which is different for the two parameters (Matsubara 2010).

Foreground and secondary biases are removed from these estimates, since the NG model directly includes them. However, an estimation of their contribution in the map is reported in Table 31.

---

[19] http://cosmologist.info/lenspix

Table 29. Results for local NG parameters at first and second order, f_{NL}^{local} and g_{NL}^{local}, obtained with Minkowski functionals on SMICA simulations in temperature and polarization.

	f_{NL}^{local}	g_{NL}^{local} ($\times 10^4$)
$f_{NL}^{local} = 0,\; g_{NL}^{local} = 0$		
T	0 ± 13	-1 ± 19
E	1 ± 42	0 ± 23
$T+E$	1 ± 12	0 ± 13
$f_{NL}^{local} = 10,\; g_{NL}^{local} = 10^5$		
T	10 ± 13	9 ± 22
E	12 ± 42	10 ± 23
$T+E$	11 ± 12	10 ± 13

Notes. These results are corrected for the lensing and ISW-lensing biases unless stated otherwise. Parameters are estimated jointly, and we report marginalized results, quoting 1σ errors. The results are the average obtained from 200 simulations.

Table 30. Results for local NG parameters at first and second order, f_{NL}^{local} and g_{NL}^{local}, obtained with Minkowski functionals on all four component separated maps in temperature and polarization.

	f_{NL}^{local}	g_{NL}^{local} ($\times 10^4$)
SMICA		
T	2 ± 13	-17 ± 19
$T+E$	3 ± 12	-8 ± 13
SEVEM		
T	3 ± 13	-23 ± 20
$T+E$	7 ± 12	-9 ± 13
NILC		
T	10 ± 13	-23 ± 20
$T+E$	12 ± 12	-15 ± 13
Commander		
T	8 ± 13	-30 ± 19
$T+E$	10 ± 13	-18 ± 13

Notes. These results are corrected for the lensing and ISW-lensing biases unless stated otherwise. Parameters are estimated jointly, and we report marginalized results, quoting 1σ errors.

Foreground and secondary biases

Foreground residuals are generally negligible, in particular in the T analysis. This is different from the *Planck* 2013 results, where the residuals were more important; this can be explained by the beam correction applied to these previous estimates which exaggerated signals from small scales.

Lensing has a significant signature in MF estimation of f_{NL}^{local}, but is even stronger in g_{NL}^{local} (the four-point correlation signature) and could be detected (and not treated just as a bias) with this estimator. The Wiener filters enhance the scales where lensing is dominant.
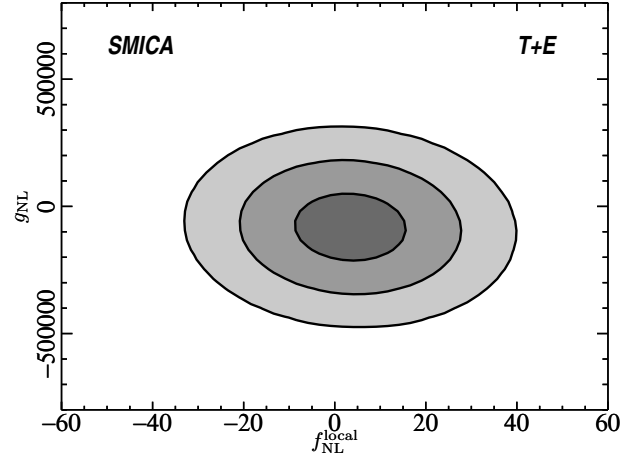
Fig. 28. Joint constraint on f_{NL}^{local} and g_{NL}^{local} obtained with MFs. The contour lines represent 1, 2 and 3σ limits of a 2D-Gaussian distribution. Constraints were obtained with SMICA temperature and polarization E maps.

Table 31. Biases for local NG parameters at first and second order f_{NL}^{local}, g_{NL}^{local} obtained with Minkowski Functionals on SMICA in temperature and polarization.

	Δf_{NL}^{local}		Δg_{NL}^{local} ($\times 10^4$)	
	T	$T+E$	T	$T+E$
SMICA				
SZ	0.0	-0.3	2.3	1.1
CIB	0.7	0.5	-6.8	3.4
Galaxy	-0.1	-0.2	-1.2	3.1
PS	0.1	0.2	2.2	1.2
Lensing	16.5	10.0	63.1	40.4

Notes. Parameters are estimated jointly, and we report marginalized results. For the corresponding error (on one map), see Table 30.

11. Implications for early Universe physics

The NG constraints obtained in this paper show consistency of *Planck* data with Gaussian primordial fluctuations, thus confirming the results obtained in the 2013 release (Planck Collaboration XXIV 2014) and improving them through the inclusion of CMB polarization data. The standard single-field slow-roll models of inflation have therefore been confirmed as a viable scenario for inflation, passing one of their most stringent tests, based on lack of measurable deviations from Gaussianity. The constraints obtained on local, equilateral, and orthogonal NG, after accounting for various contaminants, strongly limit different mechanisms proposed as alternatives to the standard inflationary models to explain the seeds of cosmological perturbations. Measurements on deviations from Gaussianity for other primordial bispectral shapes help to shed light on more subtle effects about the detailed physics of inflation.

As in Planck Collaboration XXIV (2014), in the following we derive limits on parameters of the models from the NG constraints in the following way (unless explicitly stated otherwise): we construct a posterior based on the assumption that the sampling distribution is Gaussian (as supported by Gaussian simulations); the likelihood is approximated by

the sampling distribution, but centred on the NG estimate (see Elsner & Wandelt 2009); we employ uniform or Jeffreys' priors, over intervals of the parameters values that are physically meaningful, or as otherwise stated; and in the cases when two or more parameters are involved, we marginalize the posterior to provide one-dimensional constraints on the parameter considered.

11.1. General single-field models of inflation

DBI models: DBI models of inflation (Silverstein & Tong 2004; Alishahiha et al. 2004), characterized by a non-standard kinetic term of the inflaton field, predict a non-linearity parameter $f_{\rm NL}^{\rm DBI} = -(35/108)(c_{\rm s}^{-2} - 1)$, where $c_{\rm s}$ is the sound speed of the inflaton perturbations (Silverstein & Tong 2004; Alishahiha et al. 2004; Chen et al. 2007b). The corresponding bispectrum shape is very close to the equilateral shape. Nonetheless we have constrained the exact theoretical (non-separable) shape (see Eq. (7) of Planck Collaboration XXIV 2014). The constraint we obtain $f_{\rm NL}^{\rm DBI} = 2.6 \pm 61.6$ from temperature data ($f_{\rm NL}^{\rm DBI} = 15.6 \pm 37.3$ from temperature and polarization) at 68% CL (with ISW-lensing and point sources subtracted, see Table 23) implies

$$c_{\rm s}^{\rm DBI} \geq 0.069 \qquad \text{95\% CL (}T\text{-only)}, \tag{84}$$

and

$$c_{\rm s}^{\rm DBI} \geq 0.087 \qquad \text{95\% CL (}T+E\text{)}. \tag{85}$$

In Planck Collaboration XXIV (2014) we constrained the so-called infrared (IR) DBI models (Chen 2005b,a), which arise in string frameworks. We focused on a minimal setup, considering a regime where stringy effects are negligible and predictions for primordial perturbations are built within standard field theory. In the companion paper Planck Collaboration XX (2016) we present an analysis of a more general class of IR DBI models which accounts for stringy signatures (see Bean et al. 2008) by combining *Planck* power spectrum and bispectrum constraints.

Implications for effective field theory of inflation: in this subsection we use the effective field theory approach to inflation in order to translate the contraints on $f_{\rm NL}^{\rm equil}$ and $f_{\rm NL}^{\rm ortho}$ into limits on the parameters of the Lagrangian of general single-field models of inflation (of the type $P(X, \varphi)$ models). In particular we derive the most conservative bound on the sound speed of the inflaton perturbations for this class of models.

The effective field theory approach (Cheung et al. 2008; Weinberg 2008) provides an efficient way to constrain inflationary perturbations for various classes of models that incorporate deviations from the standard single-field slow-roll scenario. In this approach the Lagrangian of the system is expanded into the (lowest dimension) operators obeying the underlying symmetries. We consider general single-field models described by the following action

$$S = \int {\rm d}^4 x \sqrt{-g} \left[-\frac{M_{\rm Pl}^2 \dot{H}}{c_{\rm s}^2} \left(\dot{\pi}^2 - c_{\rm s}^2 \frac{(\partial_i \pi)^2}{a^2} \right) \right. \tag{86}$$

$$\left. - M_{\rm Pl}^2 \dot{H}(1 - c_{\rm s}^{-2}) \dot{\pi} \frac{(\partial_i \pi)^2}{a^2} + \left(M_{\rm Pl}^2 \dot{H}(1 - c_{\rm s}^{-2}) - \frac{4}{3} M_3^4 \right) \dot{\pi}^3 \right],$$

where the curvature perturbation is related to the scalar field π as $\zeta = -H\pi$. The inflaton interaction terms $\dot{\pi}(\partial_i \pi)^2$ and $(\dot{\pi})^3$ generate two kind of bispectra with amplitudes, respectively, $f_{\rm NL}^{\rm EFT1} = -(85/324)(c_{\rm s}^{-2} - 1)$ and $f_{\rm NL}^{\rm EFT2} = -(10/243)(c_{\rm s}^{-2} - 1)[\tilde{c}_3 + (3/2)c_{\rm s}^2]$, where M_3 is the amplitude of the operator
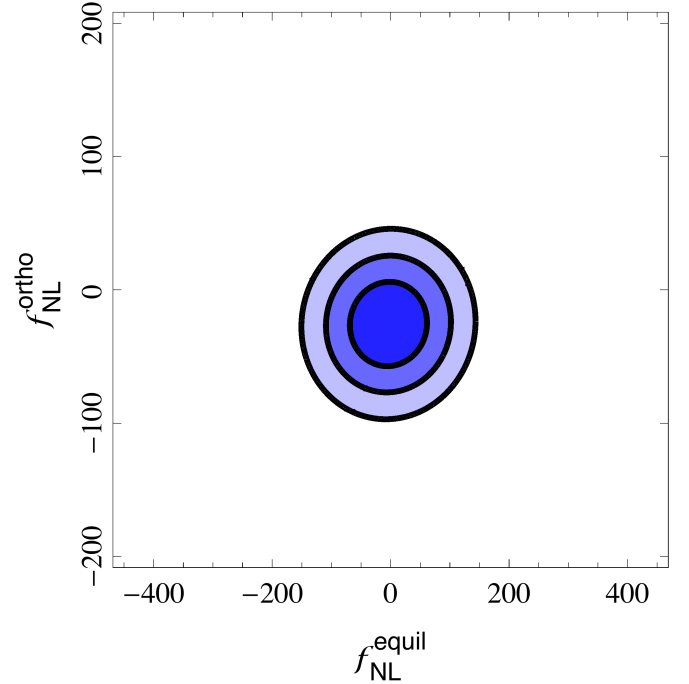
Fig. 29. 68%, 95%, and 99.7% confidence regions in the parameter space ($f_{\rm NL}^{\rm equil}$, $f_{\rm NL}^{\rm ortho}$), defined by thresholding χ^2 as described in the text.

$\dot{\pi}^3$ (Senatore et al. 2010; see also Chen et al. 2007b; Chen 2010b). These two bispectra both peak for equilateral triangles in Fourier space. Nevertheless, they are sufficiently different, and the total NG signal turns out to be a linear combination of the two, leading also to an orthogonal shape. We can put constraints on $c_{\rm s}$ and the dimensionless parameter $\tilde{c}_3(c_{\rm s}^{-2} - 1) = 2M_3^4 c_{\rm s}^2/(\dot{H} M_{\rm Pl}^2)$ (Senatore et al. 2010). Notice that DBI inflationary models corresponds to having $\tilde{c}_3 = 3(1 - c_{\rm s}^2)/2$, while $c_{\rm s} = 1$ and $M_3 = 0$ (or $\tilde{c}_3(c_{\rm s}^{-2} - 1) = 0$) represent the non-interacting (vanishing NG) case.

The mean values of the estimators for $f_{\rm NL}^{\rm equil}$ and $f_{\rm NL}^{\rm ortho}$ are expressed in terms of $c_{\rm s}$ and $\tilde{c}_3$ by

$$f_{\rm NL}^{\rm equil} = \frac{1 - c_{\rm s}^2}{c_{\rm s}^2} \left[-0.275 - 0.0780 c_{\rm s}^2 - (2/3) \times 0.780 \tilde{c}_3 \right]$$

$$f_{\rm NL}^{\rm ortho} = \frac{1 - c_{\rm s}^2}{c_{\rm s}^2} \left[0.0159 - 0.0167 c_{\rm s}^2 - (2/3) \times 0.0167 \tilde{c}_3 \right]. \tag{87}$$

Here the coefficients come from the Fisher matrix between the equilateral and orthogonal templates and the theoretical bispectra predicted by the two operators $\dot{\pi}(\nabla \pi)^2$ and $\dot{\pi}^3$. We use a χ^2 statistic given by $\chi^2(\tilde{c}_3, c_{\rm s}) = \boldsymbol{v}^{\rm T}(\tilde{c}_3, c_{\rm s}) C^{-1} \boldsymbol{v}(\tilde{c}_3, c_{\rm s})$, where $v^i(\tilde{c}_3, c_{\rm s}) = f^i(\tilde{c}_3, c_{\rm s}) - f_P^i$ ($i = \{$equilateral, orthogonal$\}$), f_P^i being the joint estimates of equilateral and orthogonal $f_{\rm NL}$ (see Table 11), C the covariance matrix of the joint estimators, and $f^i(\tilde{c}_3, c_{\rm s})$ is provided by Eq. (87). As an example in Fig. 29 we show the 68%, 95%, and 99.7% confidence regions for $f_{\rm NL}^{\rm equil}$ and $f_{\rm NL}^{\rm ortho}$ obtained from the $T + E$ constraints, requiring $\chi^2 \leq 2.28, 5.99$, and 11.62 respectively (corresponding to a χ^2 variable with two degrees of freedom). In Fig. 30 we show the corresponding confidence regions in the ($\tilde{c}_3, c_{\rm s}$) parameter space. Marginalizing over $\tilde{c}_3$ we find

$$c_{\rm s} \geq 0.020 \qquad \text{95\% CL (}T\text{-only)}, \tag{88}$$
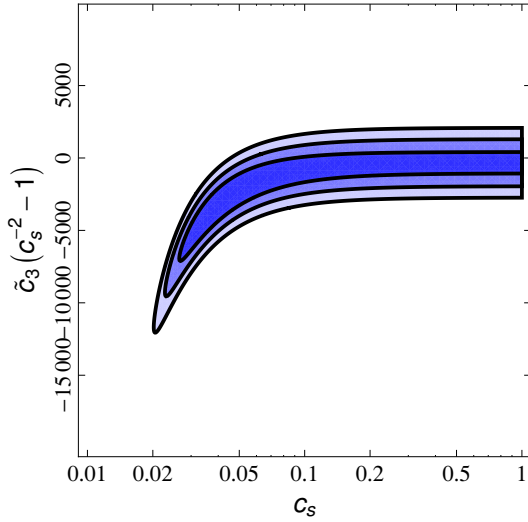
Fig. 30. 68%, 95%, and 99.7% confidence regions in the single-field inflation parameter space $(c_s, \tilde{c}_3)$, obtained from Fig. 29 via the change of variables in Eq. (87).

Fig. 31. 68%, 95%, and 99.7% probability contours in the Galileon models for c_s and $\bar{c}_s$ parameters for the $\bar{c}_s > 0$ branch (tensor spectral index $n_T < 0$).

and

$$c_s \geq 0.024 \qquad 95\% \text{ CL } (T+E). \tag{89}$$

The constraints improve by a few percent in T-only and by up to 25% by including polarization, in comparison with those of Planck Collaboration XXIV (2014).

Galileon models of inflation: Galileon models of inflation (Burrage et al. 2011; Kobayashi et al. 2010; Mizuno & Koyama 2010; Ohashi & Tsujikawa 2012) are well motivated models based on the so called "Galilean symmetry" (Nicolis et al. 2009). They are characterized by stability properties that are quite well understood (ghost-free, and stable against quantum corrections) and can arise naturally within fundamental physics models (de Rham & Gabadadze 2010b,a). Moreover they are an interesting example of models where gravity is modified on large scales and we focus on them also as a typical example of a more general class of modified gravity theories that are ghost-free (the so called Horndeski theories, Horndeski 1974; see also Planck Collaboration XIII 2016 where these models are discussed in the context of dark energy/modified gravity scenarios for the late time evolution of the universe). The predictions for the primordial perturbations are very rich. Bispectra can be generated with the same shapes as the "EFT1" and "EFT2" bispectra (see also discussion in Creminelli et al. 2011), however the amplitude(s) scale with the fluctuation sound speed as c_s^{-4}, differently from the general single-field models of inflation considered in the above subsection. They can be written as (at the lowest-order in slow-roll parameters)

$$f_{NL}^{EFT1} = \frac{17}{972} \left(-\frac{5}{c_s^4} + \frac{30}{c_s^2} - \frac{40}{c_s \bar{c}_s} + 15 \right) \tag{90}$$

$$f_{NL}^{EFT2} = \frac{1}{243} \left(\frac{5}{c_s^4} + \frac{30/A - 55}{c_s^2} + \frac{40}{c_s \bar{c}_s} - 320 \frac{c_s}{\bar{c}_s} - \frac{30}{A} + 275 \right.$$
$$\left. - 225 c_s^2 + 280 \frac{c_s^3}{\bar{c}_s} \right). \tag{91}$$

Here A, $\bar{c}_s$, and c_s are dimensionless parameters of the models. In particular c_s is the sound speed of the Galileon scalar
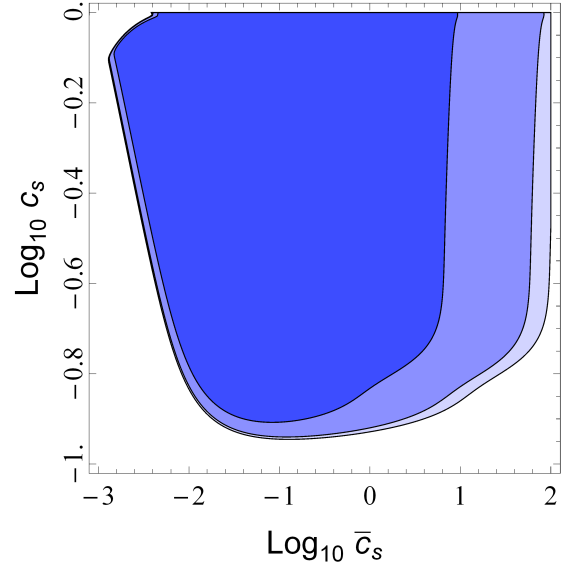
field, while $\bar{c}_s$ is a parameter that appears to break the standard consistency relation for the tensor-to-scalar perturbation ratio ($r = 16\epsilon\bar{c}_s = -8n_T\bar{c}_s$, n_T being the tensor spectral index)[20]. Accordingly to Eq. (87) a linear combination of these two bispectra generate equilateral and orthogonal bispectra templates[21]. From the *Planck* constraints on f_{NL}^{equil} and f_{NL}^{ortho} (see Table 11), we derive constraints on these model parameters following the procedure described at the beginning of this section. We choose log-constant priors in the ranges $10^{-4} \leq A \leq 10^4$, and $10^{-4} \leq \bar{c}_s \leq 10^2$, together with a uniform prior $10^{-4} < c_s < 1$. These priors have been choosen essentially on the basis of perturbative regime validity of the theory and to allow for a quite wide range of parameter values. In Fig. 31, as an example, probability contours are shown in the parameter space $(c_s, \bar{c}_s)$ from the $T + E$ constraints, after marginalizing over the parameter A. Marginalizing over both A and $\bar{c}_s$ we find

$$c_s^{Galileon} \geq 0.21 \qquad 95\% \text{ CL } (T\text{-only}), \tag{92}$$

and

$$c_s^{Galileon} \geq 0.23 \qquad 95\% \text{ CL } (T+E). \tag{93}$$

Notice that interestingly enough the parameter $\bar{c}_s$ can be negative in principle, corresponding to a blue spectral tilt of inflationary gravitational waves (without any kind of instability). We therefore also explore this branch, with a log-constant prior (for $-\bar{c}_s$), $-10^2 \leq \bar{c}_s \leq -10^{-4}$, and the same priors for the other parameters as above. Figure 32 shows the probability contours in the $(c_s, \bar{c}_s)$ plane, after marginalizing over the parameter A, for the $n_T < 0$ branch. Marginalizing over both A and $\bar{c}_s$ gives

$$c_s^{Galileon} \geq 0.19 \qquad 95\% \text{ CL } (T\text{-only}), \tag{94}$$

---

[20] For the explicit expressions of these parameters in terms of the coefficients of the Galileon Lagrangian see Planck Collaboration XX (2016).
[21] We note that we are neglecting $O(\epsilon_1/c_s^4)$ corrections (where $O(\epsilon_1)$ means also $O(\eta_s, s, ...)$); see Burrage et al. (2011) and Ribeiro & Seery (2011). These corrections will have a different shape associated with them and they are not necessarily small when compared with some of the terms displayed, e.g., the terms $O(1/c_s^2)$.
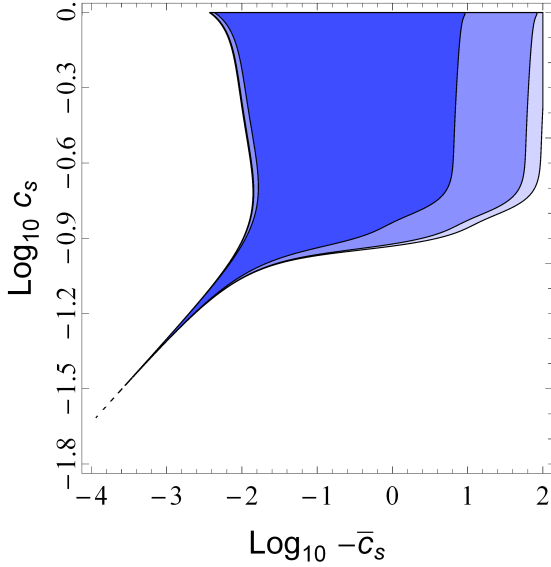
Fig. 32. 68%, 95%, and 99.7% probability contours in the Galileon models for c_s and $\bar{c}_s$ parameters for the $\bar{c}_s < 0$ branch (blue tensor spectral index $n_T > 0$).

and

$$c_s^{\text{Galileon}} \geq 0.21 \qquad 95\% \text{ CL } (T+E). \qquad (95)$$

A combined analysis of the *Planck* bispectrum and power spectrum constraints on the Galileon models is presented in the companion *Planck* paper on inflation (Planck Collaboration XX 2016).

11.2. Multi-field models

Curvaton models: the simplest adiabatic curvaton models predict local NG with an amplitude (Bartolo et al. 2004c,b)

$$f_{\text{NL}}^{\text{local}} = \frac{5}{4r_{\text{D}}} - \frac{5r_{\text{D}}}{6} - \frac{5}{3}, \qquad (96)$$

for a quadratic potential of the curvaton field (Lyth & Wands 2002; Lyth et al. 2003; Lyth & Rodriguez 2005; Malik & Lyth 2006; Sasaki et al. 2006), where $r_{\text{D}} = [3\rho_{\text{curvaton}}/(3\rho_{\text{curvaton}} + 4\rho_{\text{radiation}})]_{\text{D}}$ is the "curvaton decay fraction" at the time of the curvaton decay in the sudden decay approximation. Assuming a uniform prior, $0 < r_{\text{D}} < 1$, our constraint $f_{\text{NL}}^{\text{local}} = 2.5 \pm 5.7$ at 68% CL (see Table 11) yields

$$r_{\text{D}} \geq 0.16 \qquad 95\% \text{ CL } (T\text{-only}), \qquad (97)$$

while accounting for temperature and polarization data ($f_{\text{NL}}^{\text{local}} = 0.8 \pm 5.0$ at 68% CL) gives

$$r_{\text{D}} \geq 0.19 \qquad 95\% \text{ CL } (T+E), \qquad (98)$$

improving the previous *Planck* bound which was previously $r_{\text{D}} \geq 0.15$ (95% CL; Planck Collaboration XXIV 2014). In Planck Collaboration XX (2016), assuming there is some relic isocurvature fluctuations in the curvaton field, a limit on r_{D} is derived from the bounds on isocurvature fluctuations. In this restricted case, the limit $r_{\text{D}} > 0.98$ (95% CL) is derived, which is consistent with the constraint given here.

Notice that the above expression of $f_{\text{NL}}^{\text{local}}$ Eq. (96) is valid under the assumption that there is no significant decay of the inflaton into curvaton particles. In general one should account
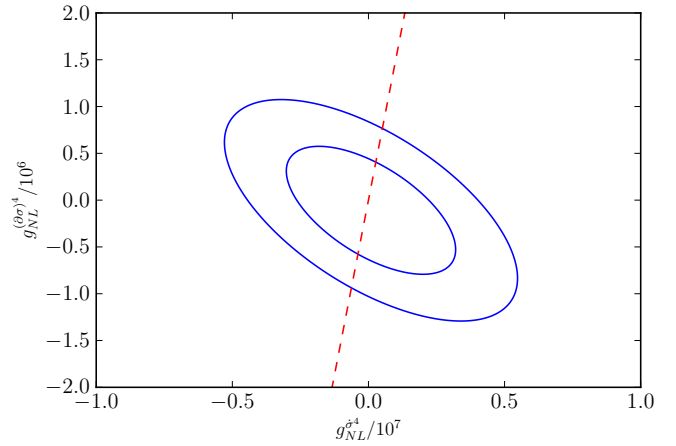
Fig. 33. 68% and 95% confidence regions in the $(g_{\text{NL}}^{\dot{\sigma}^4}, g_{\text{NL}}^{(\partial\sigma)^4})$ plane, with the Lorentz invariant model in Eq. (107) shown as the dashed line.

for such a possibility. For example, if the classical curvaton field survives and starts to dominate, then the curvaton particles produced during reheating (which have the same equation of state as the classical curvaton field) are expected to survive and dominate over other species at the epoch of their decay. The classical curvaton field and the curvaton particles decay at the same time, inevitably producing adiabatic perturbations (for a detailed discussion see Linde & Mukhanov 2006). A general formula for $f_{\text{NL}}^{\text{local}}$, accounting for the possibility that the inflaton field decays into curvaton particles, is provided in Sasaki et al. (2006):

$$f_{\text{NL}}^{\text{local}} = (1 + \Delta_s^2)\frac{5}{4r_{\text{D}}} - \frac{5r_{\text{D}}}{6} - \frac{5}{3}, \qquad (99)$$

where $\Delta_s^2 = \rho_{\text{curv. particles}}/\rho_{\text{curv.field}}$ measures the ratio of the energy density of curvaton particles to the energy density of the classical curvaton field (Linde & Mukhanov 2006; Sasaki et al. 2006) and ρ_{curvaton} in the expression for r_{D} is given by $\rho_{\text{curvaton}} = \rho_{\text{curv.particles}} + \rho_{\text{curv.field}}$. Using the uniform prior $0 < r_{\text{D}} < 1$ and $0 < \Delta_s^2 < 10^2$ our measurements of $f_{\text{NL}}^{\text{local}}$ constrain $\Delta_s^2 \leq 8.5$ at 95% CL (T) and $\Delta_s^2 \leq 6.9$ ($T+E$).

11.3. Non-standard inflation models

Directional dependence motivated by gauge fields: in Table 25 we constrained directionally-dependent bispectra (Eq. (23)). This kind of NG is generated by inflationary models characterized by the presence of gauge fields. An actual realization of this type of scenario can be obtained with a coupling between the inflaton and the gauge field(s), via the kinetic term of the field(s), i.e., $\mathcal{L} = -I^2(\phi)F^2/4$. In this formula, F^2 represents the strength of the gauge field, while $I(\phi)$ is a function of the inflaton field with an appropriate time dependence (see, e.g., Ratra 1992). In this type of scenario, vector fields can be generated during inflation, and this in turn determines the excitation of $L = 0$ and 2 modes in the bispectrum, with $f_{\text{NL}}^L = X_L(|g_*|/0.1)(N_{k_3}/60)$, where $X_{L=0} = (80/3)$ and $X_{L=2} = -(10/6)$ (Barnaby et al. 2012b; Bartolo et al. 2013a; Shiraishi et al. 2013a). The parameter g_*, appearing in the equations above, represents the amplitude of a quadrupolar anisotropy in the power spectrum (see, e.g., Ackerman et al. 2007), while N defines the number of e-folds, before the end of inflation, when the relevant scales exit

the horizon. It is thus clear that these models predict both a degree of statistical anisotropy in the power spectrum, and a potentially non-negligible bispectrum, as well as a direct relation between the two.

Starting from our SMICA constraints from $T(T+E)$ in Table 25, marginalizing over a uniform prior $50 \leq N \leq 70$, and assuming uniform priors on $-1 \leq g_* \leq 1$, we obtain the limits $-0.050 < g_* < 0.050$ ($-0.040 < g_* < 0.040$), and $-0.31 < g_* < 0.31$ ($-0.29 < g_* < 0.29$), from the $L = 0$, $L = 2$ modes, respectively (95% CL) (considering g_* as scale-independent). We note that these constraints refer to all models in which curvature perturbations are sourced by an $I^2(\phi)F^2$ term (see references in Shiraishi et al. 2013a). The constraints we obtain are consistent with the tighter (model-independent) limits obtained in Planck Collaboration XX (2016) for the case of a scale-independent g_*, from an analysis of quadrupolar anisotropies in the CMB power spectrum.

NG from gauge field production during axion inflation: we have also constrained the inverse decay NG of Eq. (25) arising typically in models where the inflaton field is a pseudoscalar axion that couples to a gauge field. Using the modal estimator we get the following constraints (removing ISW-lensing bias):

$$f_{NL}^{inv.dec} = 17 \pm 43 \qquad 68\% \text{ CL},\qquad (100)$$

for temperature only; and

$$f_{NL}^{inv.dec} = 23 \pm 26 \qquad 68\% \text{ CL},\qquad (101)$$

from temperature+polarization (see Table 23). The NG amplitude is given by $f_{NL}^{inv.dec} = f_3(\xi_*, 1, 1)\mathcal{P}_*^3 e^{6\pi\xi_*}/\mathcal{P}_\zeta^2(k_*)$, where $\mathcal{P}^{1/2} = H^2/(2\pi|\dot{\phi}|)$ is the power spectrum of vacuum-mode curvature perturbations (i.e., the power spectrum predicted without the coupling to gauge fields), $\mathcal{P}_\zeta^2(k_*)$ is the dimensionless scalar power spectrum of curvature perturbations (a star denoting evaluation at the pivot scale). The NG parameter is exponentially sensitive to the strength of the coupling between the axion and the gauge field. From Eq. (101) we limit the strength of the coupling to $\xi \leq 2.5$ (95% CL). The details together with constraints on the axion decay constant can be found in Planck Collaboration XX (2016), where an overview of various observational limits on axion (monodromy) models of inflation is presented. This limit is in agreement with the one that can be derived from tensor non-Gaussianities (see below).

Tensor NG and pseudoscalars: in inflationary scenarios associated with a pseudoscalar coupling to a U(1) gauge field, the tensor bispectrum generated via the gravitational interaction with the gauge field is expressed by Eq. (27), and the amplitude f_{NL}^{tens} depends on the following: the coupling strength of the pseudoscalar field to the gauge field (ξ); a slow-roll parameter for the inflaton (ϵ); and the power spectrum of vacuum-mode curvature perturbations ($\mathcal{P}$). The expression is $f_{NL}^{tens} \approx 6.4 \times 10^{11}\mathcal{P}^3 \epsilon^3 e^{6\pi\xi}/\xi^9$ (Cook & Sorbo 2013; Shiraishi et al. 2013b). The constraints on f_{NL}^{tens} presented in Table 26 can then be used to constrain the model parameters. Clearly there are strong degeneracies, but if we marginalize over a uniform prior $1.5 \times 10^{-9} \leq \mathcal{P} \leq 3 \times 10^{-9}$ and set $\epsilon = 0.01$, then assuming a uniform prior $0.1 \leq \xi \leq 7$, from the SMICA (T-only or $T+E$) limit, we obtain $\xi < 3.3$ (95% CL).

Warm inflation: we update the constraints on warm inflation models in the strongly dissipative regime, when dissipative effects are relevant. In this regime $f_{NL}^{warm} = -15\ln(1 + r_d/14) - 5/2$ (Moss & Xiong 2007) with a large dissipation parameter

$r_d = \Gamma/(3H)$ (where Γ is a friction term for the inflaton evolution describing the energy transfer from the inflaton field to radiation).. The limit from the 2013 *Planck* release is $\log_{10} r_d \leq 2.6$ (95% CL) (Planck Collaboration XXIV 2014). Assuming a constant prior $0 \leq \log_{10} r_d \leq 4$, the new SMICA constraint $f_{NL}^{warmS} = -23 \pm 36$ at 68% CL from T ($f_{NL}^{warmS} = -14 \pm 23$ from $T+E$), see Table 24, yields a limit on the dissipation parameter of $\log_{10} r_d \leq 3.3$ ($\log_{10} r_d \leq 2.5$) at 95% CL, with the $T+E$ constraints (in brackets), slightly improving the 2013 *Planck* limits. Values of $r_d \gtrsim 2.5$ (strongly-dissipative regime) are still allowed; however, the *Planck* constraint puts the model in a regime where there might be an overproduction of gravitinos (see Hall & Peiris 2008 and references therein). Unlike the strong dissipative regime, in the intermediate and weak dissipative regimes ($r_D \leq 1$) the NG level strongly depends on the microscopic parameters (T/H and r_D), giving rise to a new additional bispectrum shape (for details see Bastero-Gil et al. 2014).

11.4. Alternatives to inflation

Ekpyrotic/cyclic models have been proposed as an alternative to inflation (for a review, see Lehners 2010). Local NG is generated from the conversion of "intrinsic" non-Gaussian entropy perturbation modes into curvature fluctuations. Models based on a conversion taking place during the ekpyrotic phase (the so called "ekpyrotic conversion mechanism") are already ruled out (Koyama et al. 2007; Planck Collaboration XXIV 2014). Ekpyrotic models where "kinetic conversion" occurs after the ekpyrotic phase predict a local bispectrum with $f_{NL}^{local} = (3/2)\kappa_3\sqrt{\epsilon} \pm 5$, where the sign depends on the details of the conversion process (Lehners & Steinhardt 2008, 2013; Lehners 2010), where $\epsilon \simeq 50$ or greater are typical values. If we take $\epsilon \simeq 100$ and a uniform prior on $-5 < \kappa_3 < 5$ the constraints on f_{NL}^{local} from T-only (see Table 11), yield $-0.91 < \kappa_3 < 0.58$ and $-0.25 < \kappa_3 < 1.2$ at 95% CL, for the plus and minus sign in f_{NL}^{local} respectively. From the $T+E$ f_{NL}^{local} constraints (Table 11) we obtain $-0.94 < \kappa_3 < 0.38$ and $-0.27 < \kappa_3 < 1.0$ at 95% CL, for the plus and minus sign in f_{NL}^{local} respectively. If we consider $\epsilon \simeq 50$ we derive the following limits: $-1.3 < \kappa_3 < 0.81$ and $-0.35 < \kappa_3 < 1.8$ at 95% CL from T-only; $-1.3 < \kappa_3 < 0.53$ and $-0.38 < \kappa_3 < 1.5$ at 95% CL from $T+E$. Another variant of the ekpyrotic models has been investigated in Qiu et al. (2013), Li (2013), Fertig et al. (2014), where the intrinsic NG is zero and NG is generated only by non-linearities in the conversion mechanism, reaching a value of $f_{NL}^{local} \simeq \pm 5$.

11.5. Inflationary interpretation of CMB trispectrum results

We briefly interpret the trispectrum constraints in an inflationary context. First, consider the case of single field inflation. The action for the Goldstone boson π is highly constrained by residual diffeomorphism invariance (see, e.g., Smith et al. 2015). To lowest order in the derivative expansion, the most general action is:

$$S_\pi = \int d^4x \sqrt{-g}\Big\{ -M_{Pl}^2\dot{H}(\partial_\mu\pi)^2$$
$$+ 2M_2^4\left[\dot{\pi}^2 + \dot{\pi}^3 - \dot{\pi}\frac{(\partial_i\pi)^2}{a^2} + (\partial_\mu\pi)^2(\partial_\nu\pi)^2\right]$$
$$- \frac{M_3^4}{3!}\left[8\dot{\pi}^3 + 12\dot{\pi}^2(\partial_\mu\pi)^2 + \cdots\right]$$
$$+ \frac{M_4^4}{4!}\left[16\dot{\pi}^4 + 32\dot{\pi}^3(\partial_\mu\pi)^2 + \cdots\right] + \cdots\Big\},\qquad (102)$$

where the parameter M_4 is related to the trispectrum by

$$g_{\text{NL}}^{\dot{\sigma}^4} = \frac{25}{288} \frac{M_4^4}{H^4} A_\zeta c_{\text{s}}^3. \qquad (103)$$

The $g_{\text{NL}}^{\dot{\sigma}^4}$ constraint in Eq. (70) translates to the following parameter constraint in single field inflation:

$$-9.70 \times 10^{14} < \frac{M_4^4}{H^4 c_{\text{s}}^3} < 8.59 \times 10^{14} \qquad (95\% \text{ CL}). \qquad (104)$$

This constraint is a factor 1.8 better than WMAP.

Turning now to multifield inflation, we consider an action of the form

$$S_\sigma = \int \mathrm{d}^4 x \, \sqrt{-g} \left[\frac{1}{2} (\partial_\mu \sigma)^2 + \frac{1}{\Lambda_1^4} \dot{\sigma}^4 \right.$$
$$\left. + \frac{1}{\Lambda_2^4} \dot{\sigma}^2 (\partial_i \sigma)^2 + \frac{1}{\Lambda_3^4} (\partial_i \sigma)^2 (\partial_j \sigma)^2 \right], \qquad (105)$$

where σ is a spectator field that acquires quantum fluctuations with power spectrum $P_\sigma(k) = H^2/(2k^3)$ and converts to adiabatic curvature via $\zeta = (2A_\zeta)^{1/2} H^{-1} \sigma$. The trispectrum in this model is

$$g_{\text{NL}}^{\dot{\sigma}^4} A_\zeta = \frac{25}{768} \frac{H^4}{\Lambda_1^4},$$
$$g_{\text{NL}}^{\dot{\sigma}^2(\partial\sigma)^2} A_\zeta = -\frac{325}{6912} \frac{H^4}{\Lambda_2^4}, \qquad (106)$$
$$g_{\text{NL}}^{(\partial\sigma)^4} A_\zeta = \frac{2575}{20\,736} \frac{H^4}{\Lambda_3^4},$$

so we can constrain its parameters by thresholding the χ^2 defined in Eq. (75). For example, if we consider the Lorentz invariant model

$$S = \int \mathrm{d}^4 x \, \sqrt{-g} \left[\frac{1}{2} (\partial_\mu \sigma)^2 + \frac{1}{\Lambda^4} (\partial_\mu \sigma)^2 (\partial_\nu \sigma)^2 \right], \qquad (107)$$

so that the parameters Λ_i of the more general action in Eq. (105) are given by $\Lambda_1^4 = -2\Lambda_2^4 = \Lambda_3^4 = \Lambda^4$, then by thresholding at $\Delta\chi^2 = 4$ (as appropriate for one degree of freedom), we obtain the following constraint on the parameter Λ:

$$-0.26 < \frac{H^4}{\Lambda^4} < 0.20 \qquad (95\% \text{ CL}). \qquad (108)$$

Constraints in other parameter spaces can also be obtained by thresholding the χ^2 defined in Eq. (75). For example we show 68% and 95% confidence regions in the $(g_{\text{NL}}^{\dot{\sigma}^4}, g_{\text{NL}}^{(\partial\sigma)^4})$-plane, obtained by thresholding at $\chi^2 = 2.28$ and $\chi^2 = 5.99$ as appropriate for a χ^2 random variable with two degrees of freedom.

DBI trispectrum: the trispectrum constraint on the shape $\dot{\sigma}^4$ in Eq. (70) can also be used to obtain a lower bound on the DBI model sound speed. This is because, in the small sound speed limit (Chen et al. 2009; Arroja et al. 2009), the dominant contribution to the contact interaction trispectrum (Huang & Shiu 2006) has this shape. The corresponding non-linearity parameter is $g_{\text{NL}}^{\dot{\sigma}^4} = -25/(768\,c_{\text{s}}^4)$. We follow the same procedure as described at the beginning of this Sect. 11 and, assuming a uniform prior in the range $0 \le c_{\text{s}} \le 1/5$, we can derive a constraint on c_{s} as

$$c_{\text{s}}^{\text{DBI}} \ge 0.021, \qquad 95\% \text{ CL}. \qquad (109)$$

This constraint is consistent with the ones derived from the bispectrum measurements (see Eqs. (84) and (85)) and it is only a factor of about three worse. Notice, however, that in this case we are ignoring the scalar exchange contribution, which is of the same order in c_{s}.

Curvaton trispectrum: for the simplest curvaton scenario, the trispectrum non-linearity parameter $g_{\text{NL}}^{\text{local}}$ prediction is (Sasaki et al. 2006)

$$g_{\text{NL}}^{\text{local}} = \frac{25}{54} \left(-\frac{9}{r_{\text{D}}} + \frac{1}{2} + 10 r_{\text{D}} + 3 r_{\text{D}}^2 \right). \qquad (110)$$

Following the procedure described at the beginning of Sect. 11, we use the observational constraint obtained in Sect. 9 (Eq. (70)), and the same prior ($0 < r_{\text{D}} < 1$) as in 11.2, to obtain a lower bound on the curvaton decay fraction as

$$r_{\text{D}} \ge 0.05 \qquad 95\% \text{ CL}. \qquad (111)$$

This limit is consistent with the previous ones derived using the bispectrum measurements and it is a factor of about 3 to 4 worse.

12. Conclusions

In this paper we have presented the constraints on primordial NG using the full *Planck* mission data. The results have improved compared to the *Planck* 2013 release (Planck Collaboration XXIV 2014) as a consequence of including data from the full mission and taking advantage of *Planck*'s polarization capability – the first time that maps of the CMB polarization anisotropies have been used to constrain primordial NG.

Using temperature data alone, the constraints on the local, equilateral, and orthogonal bispectrum templates are $f_{\text{NL}}^{\text{local}} = 2.5 \pm 5.7$, $f_{\text{NL}}^{\text{equil}} = -16 \pm 70$, and $f_{\text{NL}}^{\text{ortho}} = -34 \pm 33$. Moving from the nominal *Planck* 2013 data to the full mission data yielded modest improvements of up to 15% (for the orthogonal shape). After the inclusion of full mission polarization data, our final constraints become $f_{\text{NL}}^{\text{local}} = 0.8 \pm 5.0$, $f_{\text{NL}}^{\text{equil}} = -4 \pm 43$, and $f_{\text{NL}}^{\text{ortho}} = -26 \pm 21$, which represents a substantial step forward relative to *Planck* 2013, with error bars shrinking by 14% (local), 43% (equilateral), and 46% (orthogonal). These improved limits on the standard shapes enhance our understanding of different inflationary models that can potentially lead to subtle effects beyond the simplest models of inflation.

The reason that the polarization data provide such complementary constraints on primordial curvature perturbations is due to the phase shift of the CMB polarization transfer functions compared to the temperature transfer functions. So, despite the relatively much lower signal-to-noise in the polarization maps, their inclusion leads to appreciable improvements on limits on NG parameters. Nevertheless, the full characterization of the noise properties in the polarized maps is still ongoing. In spite of the extensive testing and cross-checks validating the combined temperature and polarization results, we therefore conservatively recommend that *all* results that include polarization information, not just the polarization-only results, be taken as preliminary at this stage.

The complementary nature of the polarization information also represents an important cross-check on the analysis. The *Planck* results based on polarization alone are statistically consistent with the results based on temperature alone, with a precision comparable to that achievable in an optimal analysis of the WMAP 3-yr temperature maps (Spergel et al. 2007; Creminelli et al. 2007; Yadav & Wandelt 2008).

Our analysis was subject to an extensive validation exercise. In addition to extensive simulation tests, including for the first time a detailed test of the impact of time-domain de-glitching, our results are supported by tests for robustness under change of estimator implementations (KSW, binned bispectrum, and two modal estimators), and variations in sky coverage as well as upper and lower multipole cutoffs. We also tested for possible directional dependence using a needlet estimator. These tests form the basis of our selection of `SMICA` as the main foreground cleaning method for our headline results.

The *Planck* 2015 analysis presented here provides constraints on a greatly extended range of template families. These extensions include a tenfold increase in the range of frequencies covered in feature models, giving rise to linearly oscillating bispectra, generalized shapes for oscillating models including for logarithmic oscillations, tests for deviations from the Bunch-Davies vacuum, models of equilateral type in the context of the effective field theory of inflation, and direction-dependent primordial NG. Beyond purely scalar mode templates we also tested for parity-violating tensor NG.

Using the full mission data with polarization, we have investigated the hints of NG reported in the *Planck* 2013 analysis of oscillatory features. While no individual feature or resonance model rises above our detection threshold of 3σ (after inclusion of the look-elsewhere effect), the results of integrated (multi-peak) statistical tests indicate that continued investigation of oscillatory and non-scaling models is warranted.

In addition to searches for specific NG templates, we present model-independent reconstructions of the temperature and polarization bispectra using the modal and binned bispectrum approaches. These full mission reconstructions can achieve twice the resolution of the *Planck* 2013 results, demonstrating excellent consistency in temperature, and good agreement with the WMAP9 reconstruction in regions where this earlier data set is signal-dominated.

The inclusion of polarization information leads to significantly improved constraints on NG in primordial isocurvature perturbations, providing complementary information to 2-point function results for models where the NG in isocurvature components is more easily detectable than its contribution to the power spectrum.

A significant addition to this year's analysis is the inclusion of detailed trispectrum results due to cubic NG. The local trispectrum is constrained by *Planck* temperature data to be $g_{\mathrm{NL}}^{\mathrm{local}} = (-9.0 \pm 7.7) \times 10^4$ and the other two shapes were also found to be consistent with Gaussianity. Both 3-point and 4-point constraints are consistent with the improved (though still suboptimal) constraints from Minkowski functionals, a very different estimation framework. This concordance adds confidence in our results.

We have discussed the implications of our results on the physics of the early Universe, showing that the *n*-point functions for $n > 2$ provide a significant window onto the primordial Universe beyond the power spectrum, constraining general-single-field, multifield, and non-standard inflation models, as well as alternatives to inflation. Using bispectrum and trispectrum limits we updated results on the parameter space of the inflationary models (and alternatives) already tested in 2013, and constrained the parameter space of other well-motivated inflationary models (e.g., Galileon-like models of inflation, and models where axion/pseudoscalar fields are present during inflation).

The global picture that emerges is one of consistency with the premises of the ΛCDM cosmology, namely that the structure we observe today is the consequence of passive evolution of adiabatic, Gaussian, primordial seed perturbations. Nevertheless, NG at some level is expected in all inflationary models, and hence we should strive to find means to reduce errors on f_{NL} still further.

References

Achúcarro, A., Gong, J.-O., Hardeman, S., Palma, G. A., & Patil, S. P. 2011, J. Cosmol. Astropart. Phys., 1, 30

Achucarro, A., Gong, J.-O., Palma, G. A., & Patil, S. P. 2013, Phys. Rev. D, 87, 121301

Ackerman, L., Carroll, S. M., & Wise, M. B. 2007, Phys. Rev. D, 75, 083502

Acquaviva, V., Bartolo, N., Matarrese, S., & Riotto, A. 2003, Nucl. Phys. B, 667, 119

Adshead, P., Hu, W., Dvorkin, C., & Peiris, H. V. 2011, Phys. Rev. D, 84, 043519

Adshead, P., Dvorkin, C., Hu, W., & Lim, E. A. 2012, Phys. Rev. D, 85, 023531

Agullo, I., & Parker, L. 2011, General Relativity and Gravitation, 43, 2541

Alishahiha, M., Silverstein, E., & Tong, D. 2004, Phys. Rev. D, 70, 123505

Argüeso, F., González-Nuevo, J., & Toffolatti, L. 2003, ApJ, 598, 86

Arkani-Hamed, N., Creminelli, P., Mukohyama, S., & Zaldarriaga, M. 2004, J. Cosmol. Astropart. Phys., 4, 1

Arroja, F., Mizuno, S., Koyama, K., & Tanaka, T. 2009, Phys. Rev. D, 80, 043527

Arroja, F., Bartolo, N., Dimastrogiovanni, E., & Fasiello, M. 2013, J. Cosmol. Astropart. Phys., 1311, 005

Ashoorioon, A., & Shiu, G. 2011, J. Cosmol. Astropart. Phys., 1103, 025

Babich, D., Creminelli, P., & Zaldarriaga, M. 2004, J. Cosmol. Astropart. Phys., 8, 9

Bardeen, J. M. 1980, Phys. Rev. D, 22, 1882

Barnaby, N., & Cline, J. M. 2006, Phys. Rev. D, 73, 106012

Barnaby, N., & Peloso, M. 2011, Phys. Rev. Lett., 106, 181301

Barnaby, N., Namba, R., & Peloso, M. 2011, J. Cosmol. Astropart. Phys., 4, 9

Barnaby, N., Moxon, J., Namba, R., et al. 2012a, Phys. Rev. D, 86, 103508

Barnaby, N., Namba, R., & Peloso, M. 2012b, Phys. Rev. D, 85, 123523

Barnaby, N., Pajer, E., & Peloso, M. 2012c, Phys. Rev. D, 85, 023525

Bartolo, N., Matarrese, S., & Riotto, A. 2002, Phys. Rev. D, 65, 103505

Bartolo, N., Komatsu, E., Matarrese, S., & Riotto, A. 2004a, Phys. Rep., 402, 103

Bartolo, N., Matarrese, S., & Riotto, A. 2004b, Phys. Rev. Lett., 93, 231301

Bartolo, N., Matarrese, S., & Riotto, A. 2004c, Phys. Rev. D, 69, 043503

Bartolo, N., Fasiello, M., Matarrese, S., & Riotto, A. 2010a, J. Cosmol. Astropart. Phys., 8, 8

Bartolo, N., Fasiello, M., Matarrese, S., & Riotto, A. 2010b, J. Cosmol. Astropart. Phys., 9, 35

Bartolo, N., Matarrese, S., Peloso, M., & Ricciardone, A. 2013a, Phys. Rev. D, 87, 023504

Bartolo, N., Matarrese, S., Peloso, M., & Ricciardone, A. 2013b, J. Cosmol. Astropart. Phys., 8, 22

Bartolo, N., Dimastrogiovanni, E., & Fasiello, M. 2013c, J. Cosmol. Astropart. Phys., 1309, 037

Bartolo, N., Peloso, M., Ricciardone, A., & Unal, C. 2014, J. Cosmol. Astropart. Phys., 11, 9

Bastero-Gil, M., Berera, A., Moss, I. G., & Ramos, R. O. 2014, J. Cosmol. Astropart. Phys., 12, 8

Battefeld, T., Niemeyer, J. C., & Vlaykov, D. 2013, J. Cosmol. Astropart. Phys., 5, 6

Baumann, D., & Green, D. 2012, Phys. Rev. D, 85, 103520
Bean, R., Chen, X., Peiris, H., & Xu, J. 2008, Phys. Rev. D, 77, 023527
Behbahani, S. R., Dymarsky, A., Mirbabayi, M., & Senatore, L. 2012, J. Cosmol. Astropart. Phys., 1212, 036
Bennett, C. L., Larson, D., Weiland, J. L., et al. 2013, ApJS, 208, 20
Bernardeau, F., & Uzan, J.-P. 2002, Phys. Rev. D, 66, 103506
Bernardeau, F., Kofman, L., & Uzan, J.-P. 2004, Phys. Rev. D, 70, 083004
Bond, J. R., Frolov, A. V., Huang, Z., & Kofman, L. 2009, Phys. Rev. Lett., 103, 071301
Brown, I., & Crittenden, R. 2005, Phys. Rev. D, 72, 063002
Bucher, M., Moodley, K., & Turok, N. 2000, Phys. Rev. D, 62, 083508
Bucher, M., van Tent, B., & Carvalho, C. S. 2010, MNRAS, 407, 2193
Bucher, M., Racine, B., & van Tent, B. 2015, J. Cosmol. Astropart. Phys. 5, 055
Burrage, C., de Rham, C., Seery, D., & Tolley, A. J. 2011, J. Cosmol. Astropart. Phys., 1, 14
Byrnes, C. T., & Choi, K.-Y. 2010, Adv. Astron., 2010, 724525
Catalano, A., Ade, P., Atik, Y., et al. 2014, A&A, 569, A88
Chambers, A., & Rajantie, A. 2008, Phys. Rev. Lett., 100, 041302
Chen, X. 2005a, J. High Energy Phys., 8, 45
Chen, X. 2005b, Phys. Rev. D, 71, 063506
Chen, X. 2010a, J. Cosmol. Astropart. Phys., 12, 3
Chen, X. 2010b, Adv. Astron., 2010
Chen, X. 2011, ArXiv e-prints [arXiv:1104.1323]
Chen, X., & Wang, Y. 2010, J. Cosmol. Astropart. Phys., 4, 27
Chen, X., Easther, R., & Lim, E. A. 2007a, J. Cosmol. Astropart. Phys., 6, 23
Chen, X., Huang, M.-X., Kachru, S., & Shiu, G. 2007b, J. Cosmol. Astropart. Phys., 1, 2
Chen, X., Easther, R., & Lim, E. A. 2008, J. Cosmol. Astropart. Phys., 4, 10
Chen, X., Hu, B., Huang, M.-X., Shiu, G., & Wang, Y. 2009, J. Cosmol. Astropart. Phys., 8, 8
Chen, X., Namjoo, M. H., & Wang, Y. 2015, J. Cosmol. Astropart. Phys., 2, 27
Cheung, C., Fitzpatrick, A. L., Kaplan, J., Senatore, L., & Creminelli, P. 2008, J. High Energy Phys., 3, 14
Cicoli, M., Tasinato, G., Zavala, I., Burgess, C. P., & Quevedo, F. 2012, J. Cosmol. Astropart. Phys., 5, 39
Cook, J. L., & Sorbo, L. 2013, J. Cosmol. Astropart. Phys., 11, 47
Cooray, A., & Melchiorri, A. 2006, J. Cosmol. Astro-Particle Phys., 1, 18
Crawford, T. M., Schaffer, K. K., Bhattacharya, S., et al. 2014, ApJ, 784, 143
Creminelli, P., Nicolis, A., Senatore, L., Tegmark, M., & Zaldarriaga, M. 2006, J. Cosmol. Astropart. Phys., 5, 4
Creminelli, P., Senatore, L., Zaldarriaga, M., & Tegmark, M. 2007, J. Cosmol. Astropart. Phys., 3, 5
Creminelli, P., D'Amico, G., Musso, M., Noreña, J., & Trincherini, E. 2011, J. Cosmol. Astropart. Phys., 2, 6
Curto, A., Macias-Perez, J. F., Martínez-González, E., et al. 2008, A&A, 486, 383
Curto, A., Tucci, M., Kunz, M., & Martinez-Gonzalez, E. 2015, MNRAS, 450, 4
de Rham, C., & Gabadadze, G. 2010a, Phys. Rev. D, 82, 044020
de Rham, C., & Gabadadze, G. 2010b, Phys. Lett. B, 693, 334
Delabrouille, J., Betoule, M., Melin, J.-B., et al. 2013, A&A, 553, A96
Desjacques, V., & Seljak, U. 2010, Phys. Rev., D81, 023006
Donzelli, S., Hansen, F. K., Liguori, M., Marinucci, D., & Matarrese, S. 2012, ApJ, 755, 19
Ducout, A., Bouchet, F. R., Colombi, S., Pogosyan, D., & Prunet, S. 2013, MNRAS, 429, 2104
Dvali, G., Gruzinov, A., & Zaldarriaga, M. 2004a, Phys. Rev. D, 69, 083505
Dvali, G., Gruzinov, A., & Zaldarriaga, M. 2004b, Phys. Rev. D, 69, 023505
Elsner, F., & Wandelt, B. D. 2009, ApJS, 184, 264
Elsner, F., & Wandelt, B. D. 2012, ArXiv e-prints [arXiv:1211.0585]
Endlich, S. 2013, J. Cosmol. Astropart. Phys., 10, 11
Endlich, S., Horn, B., Nicolis, A., & Wang, J. 2014, Phys. Rev. D, 90, 063506
Enqvist, K., & Sloth, M. S. 2002, Nucl. Phys. B, 626, 395
Enqvist, K., Jokinen, A., Mazumdar, A., Multamäki, T., & Väihkönen, A. 2005, Phys. Rev. Lett., 94, 161301
Eriksen, H. K., Novikov, D. I., Lilje, P. B., Banday, A. J., & Górski, K. M., 2004, ApJ, 612, 64
Falk, T., Rangarajan, R., & Srednicki, M. 1993, ApJ, 403, L1
Fantaye, Y., Marinucci, D., Hansen, F., & Maino, D. 2015, Phys. Rev. D, 91, 063501
Feng, C., Cooray, A., Smidt, J., et al. 2015, Phys. Rev. D, 92, 043509
Fergusson, J. 2014, Phys. Rev. D, 90, 043533
Fergusson, J. R., Liguori, M., & Shellard, E. P. S. 2010a, Phys. Rev. D, 82, 023502
Fergusson, J. R., Regan, D. M., & Shellard, E. P. S. 2010b, ArXiv e-prints [arXiv:1012.6039]
Fergusson, J. R., Liguori, M., & Shellard, E. P. S. 2012, J. Cosmol. Astropart. Phys., 12, 32

Fergusson, J., Gruetjen, H., Shellard, E., & Wallisch, B. 2015, Phys. Rev. D, 91, 123506
Fergusson, J., Gruetjen, H., Shellard, E., & Liguori, M. 2015, Phys. Rev. D, 91, 023502
Ferreira, R. Z., & Sloth, M. S. 2014, J. High Energy Phys., 2014, 139
Fertig, A., Lehners, J.-L., & Mallwitz, E. 2014, Phys. Rev. D, 89, 103537
Flauger, R., & Pajer, E. 2011, J. Cosmol. Astropart. Phys., 1, 17
Flauger, R., McAllister, L., Pajer, E., Westphal, A., & Xu, G. 2010, J. Cosmol. Astropart. Phys., 6, 9
Gangui, A., & Martin, J. 2000, MNRAS, 313, 323
Gangui, A., Lucchin, F., Matarrese, S., & Mollerach, S. 1994, ApJ, 430, 447
Gao, X., Kobayashi, T., Yamaguchi, M., & Yokoyama, J. 2011, Phys. Rev. Lett., 107, 211301
Giannantonio, T., Ross, A. J., Percival, W. J., et al. 2014, Phys. Rev. D 89, 023511
González-Nuevo, J., Toffolatti, L., & Argüeso, F. 2005, ApJ, 621, 1
Górski, K. M., Hivon, E., Banday, A. J., et al. 2005, ApJ, 622, 759
Hall, L. M. H., & Peiris, H. V. 2008, J. Cosmol. Astropart. Phys., 1, 27
Hannestad, S., Haugbolle, T., Jarnhus, P. R., & Sloth, M. S. 2010, J. Cosmol. Astropart. Phys., 1006, 001
Hanson, D., & Lewis, A. 2009, Phys. Rev. D, 80, 063004
Heavens, A. F. 1998, MNRAS, 299, 805
Hikage, C., & Matsubara, T. 2012, MNRAS, 425, 2187
Hikage, C., Komatsu, E., & Matsubara, T. 2006, ApJ, 653, 11
Hikage, C., Matsubara, T., Coles, P., et al. 2008, MNRAS, 389, 1439
Hikage, C., Koyama, K., Matsubara, T., Takahashi, T., & Yamaguchi, M. 2009, MNRAS, 398, 2188
Hikage, C., Kawasaki, M., Sekiguchi, T., & Takahashi, T. 2013a, J. Cosmol. Astropart. Phys., 7, 7
Hikage, C., Kawasaki, M., Sekiguchi, T., & Takahashi, T. 2013b, J. Cosmol. Astropart. Phys., 3, 20
Holman, R., & Tolley, A. J. 2008, J. Cosmol. Astropart. Phys., 0805, 001
Horndeski, G. W. 1974, Int. J. Theor. Phys., 10, 363
Hu, W. 2000, Phys. Rev. D, 62, 043007
Huang, M.-X., & Shiu, G. 2006, Phys. Rev. D, 74, 121301
Kamionkowski, M., & Souradeep, T. 2011, Phys. Rev. D, 83, 027301
Kawasaki, M., Nakayama, K., Sekiguchi, T., Suyama, T., & Takahashi, F. 2008, J. Cosmol. Astropart. Phys., 11, 19
Kawasaki, M., Nakayama, K., Sekiguchi, T., Suyama, T., & Takahashi, F. 2009, J. Cosmol. Astropart. Phys., 1, 42
Kawakami, E., Kawasaki, M., Miyamoto, K., Nakayama, K., & Sekiguchi, T. 2012, J. Cosmol. Astropart. Phys., 7, 37
Kobayashi, T., Yamaguchi, M., & Yokoyama, J. 2010, Phys. Rev. Lett., 105, 231302
Kofman, L. 2003, ArXiv e-prints [arXiv:astro-ph/0303614]
Kolb, E. W., Riotto, A., & Vallinotto, A. 2006, Phys. Rev. D, 73, 023522
Komatsu, E. 2002, ArXiv e-prints [arXiv:astro-ph/0206039]
Komatsu, E. 2010, Class. Quant. Grav., 27, 124010
Komatsu, E., & Spergel, D. N. 2001, Phys. Rev. D, 63, 063002
Komatsu, E., Spergel, D. N., & Wandelt, B. D. 2005, ApJ, 634, 14
Koyama, K., Mizuno, S., Vernizzi, F., & Wands, D. 2007, J. Cosmol. Astropart. Phys., 0711, 024
Lacasa, F., & Aghanim, N. 2014, A&A, 569, A51
Lacasa, F., Aghanim, N., Kunz, M., & Frommert, M. 2012, MNRAS, 421, 1982
Lacasa, F., Pénin, A., & Aghanim, N. 2014, MNRAS, 439, 123
Lagache, G., Puget, J.-L., & Dole, H. 2005, ARA&A, 43, 727
Lan, X., & Marinucci, D. 2008, Electronic J. Statistics, 2, 332
Langlois, D., & Lepidi, A. 2011, J. Cosmol. Astropart. Phys., 1, 8
Langlois, D., & van Tent, B. 2011, Class. Quant. Grav., 28, 222001
Langlois, D., & van Tent, B. 2012, J. Cosmol. Astropart. Phys., 7, 40
Langlois, D., Vernizzi, F., & Wands, D. 2008, J. Cosmol. Astropart. Phys., 12, 4
Lehners, J.-L. 2010, Adv. Astron., 2010, 903907
Lehners, J.-L., & Steinhardt, P. J. 2008, Phys. Rev. D, 77, 063533
Lehners, J.-L., & Steinhardt, P. J. 2013, Phys. Rev. D, 87, 123533
Leistedt, B., Peiris, H. V., & Roth, N. 2014, Phys. Rev. Lett., 113, 221301
Lewis, A., Challinor, A., & Hanson, D. 2011, J. Cosmol. Astropart. Phys., 3, 18
Li, M. 2013, Phys. Lett. B, 724, 192
Liguori, M., Sefusatti, E., Fergusson, J. R., & Shellard, E. P. S. 2010, Adv. Astron., 2010, 980523
Linde, A., & Mukhanov, V. 1997, Phys. Rev. D, 56, 535
Linde, A., & Mukhanov, V. 2006, J. Cosmol. Astropart. Phys., 4, 9
Linde, A., Mooij, S., & Pajer, E., 2013, Phys. Rev. D, 87, 103506
Lyth, D. H. 2005, J. Cosmol. Astropart. Phys., 11, 6
Lyth, D. H., & Riotto, A. 2006, Phys. Rev. Lett., 97, 121301
Lyth, D. H., & Rodriguez, Y. 2005, Phys. Rev. Lett., 95, 121302
Lyth, D. H., Ungarelli, C., & Wands, D. 2003, Phys. Rev. D, 67, 023503
Maldacena, J. 2003, J. High Energy Phys., 5, 13
Lyth, D. H., & Wands, D. 2002, Phys. Lett. B, 524, 5
Maldacena, J. M., & Pimentel, G. L. 2011, J. High Energy Phys., 9, 45

Malik, K. A., & Lyth, D. H. 2006, J. Cosmol. Astropart. Phys., 9, 8
Mangilli, A., & Verde, L. 2009, Phys. Rev. D, 80, 123007
Mangilli, A., Wandelt, B., Elsner, F., & Liguori, M. 2013, A&A, 555, A82
Matsubara, T. 2010, Phys. Rev. D, 81, 083505
McFadden, P., & Skenderis, K. 2011, J. Cosmol. Astropart. Phys., 6, 30
Mecke, K. R., Buchert, T., & Wagner, H. 1994, A&A, 288, 697
Meerburg, P. D., & Pajer, E. 2013, J. Cosmol. Astropart. Phys., 2, 17
Meerburg, P. D., van der Schaar, J. P., & Stefano Corasaniti, P. 2009, J. Cosmol. Astropart. Phys., 5, 18
Meerburg, P. D., Münchmeyer, M., & Wandelt, B. 2016, Phys. Rev. D, 93, 043536
Mizuno, S., & Koyama, K. 2010, Phys. Rev. D, 82, 103518
Modest, H. I., Räth, C., Banday, A. J., et al. 2013, MNRAS, 428, 551
Mollerach, S. 1990, Phys. Rev. D, 42, 313
Moroi, T., & Takahashi, T. 2001, Phys. Lett. B, 522, 215
Moss, I. G., & Xiong, C. 2007, J. Cosmol. Astropart. Phys., 4, 7
Münchmeyer, M., Bouchet, F., Jackson, M., & Wandelt, B. 2014, A&A, 570, A94
Münchmeyer, M., Meerburg, P. D., & Wandelt, B. D. 2015, Phys. Rev. D, 91, 043534
Munshi, D., & Heavens, A. 2010, MNRAS, 401, 2406
Munshi, D., Smidt, J., Cooray, A., et al. 2013, MNRAS, 434, 2830
Natoli, P., de Troia, G., Hikage, C., et al. 2010, MNRAS, 408, 1658
Nicolis, A., Rattazzi, R., & Trincherini, E. 2009, Phys. Rev. D, 79, 064036
Novaes, C. P., Bernui, A., Ferreira, I. S., & Wuensche, C. A. 2015, J. Cosmol. Astropart. Phys., 9, 064
Ohashi, J., & Tsujikawa, S. 2012, J. Cosmol. Astropart. Phys., 10, 35
Okamoto, T., & Hu, W. 2002, Phys. Rev. D, 66, 063008
Park, C., Choi, Y.-Y., Vogeley, M. S., et al. 2005, ApJ, 633, 11
Pénin, A., Lacasa, F., & Aghanim, N. 2014, MNRAS, 439, 143
Planck Collaboration VII. 2011, A&A, 536, A7
Planck Collaboration X. 2014, A&A, 571, A10
Planck Collaboration XII. 2014, A&A, 571, A12
Planck Collaboration XVII. 2014, A&A, 571, A17
Planck Collaboration XVIII. 2014, A&A, 571, A18
Planck Collaboration XIX. 2014, A&A, 571, A19
Planck Collaboration XXII. 2014, A&A, 571, A22
Planck Collaboration XXIV. 2014, A&A, 571, A24
Planck Collaboration XXV. 2014, A&A, 571, A25
Planck Collaboration XXX. 2014, A&A, 571, A30
Planck Collaboration I. 2016, A&A, 594, A1
Planck Collaboration II. 2016, A&A, 594, A2
Planck Collaboration III. 2016, A&A, 594, A3
Planck Collaboration IV. 2016, A&A, 594, A4
Planck Collaboration V. 2016, A&A, 594, A5
Planck Collaboration VI. 2016, A&A, 594, A6
Planck Collaboration VII. 2016, A&A, 594, A7
Planck Collaboration VIII. 2016, A&A, 594, A8
Planck Collaboration IX. 2016, A&A, 594, A9
Planck Collaboration X. 2016, A&A, 594, A10
Planck Collaboration XI. 2016, A&A, 594, A11
Planck Collaboration XII. 2016, A&A, 594, A12
Planck Collaboration XIII. 2016, A&A, 594, A13
Planck Collaboration XIV. 2016, A&A, 594, A14
Planck Collaboration XV. 2016, A&A, 594, A15
Planck Collaboration XVI. 2016, A&A, 594, A16
Planck Collaboration XVII. 2016, A&A, 594, A17
Planck Collaboration XVIII. 2016, A&A, 594, A18
Planck Collaboration XIX. 2016, A&A, 594, A19
Planck Collaboration XX. 2016, A&A, 594, A20
Planck Collaboration XXI. 2016, A&A, 594, A21
Planck Collaboration XXII. 2016, A&A, 594, A22
Planck Collaboration XXIII. 2016, A&A, 594, A23
Planck Collaboration XXIV. 2016, A&A, 594, A24
Planck Collaboration XXV. 2016, A&A, 594, A25
Planck Collaboration XXVI. 2016, A&A, 594, A26
Planck Collaboration XXVII. 2016, A&A, 594, A27
Planck Collaboration XXVIII. 2016, A&A, 594, A28
Qiu, T., Gao, X., & Saridakis, E. N. 2013, Phys. Rev. D, 88, 043525
Ratra, B. 1992, ApJ, 391, L1
Regan, D., Gosenca, M., & Seery, D. 2015, J. Cosmol. Astropart. Phys. 01, 013
Ribeiro, R. H., & Seery, D. 2011, J. Cosmol. Astropart. Phys., 10, 27
Rigopoulos, G. I., Shellard, E. P. S., & van Tent, B. J. W. 2006, Phys. Rev. D, 73, 083522
Rigopoulos, G. I., Shellard, E. P. S., & van Tent, B. J. W. 2007, Phys. Rev. D, 76, 083512
Rudjord, Ø., Hansen, F. K., Lan, X., et al. 2010, ApJ, 708, 1321
Salem, M. P. 2005, Phys. Rev. D, 72, 123516

Sasaki, M., Valiviita, J., & Wands, D. 2006, Phys. Rev. D, 74, 103003
Schmalzing, J., & Buchert, T. 1997, ApJ, 482, L1
Schmalzing, J., & Gorski, K. M. 1998, MNRAS, 297, 355
Sekiguchi, T., & Sugiyama, N. 2013, J. Cosmol. Astropart. Phys., 1309, 002
Senatore, L., & Zaldarriaga, M. 2011, J. Cosmol. Astropart. Phys., 1, 3
Senatore, L., & Zaldarriaga, M. 2012a, J. Cosmol. Astropart. Phys., 1208, 001
Senatore, L., & Zaldarriaga, M. 2012b, JHEP, 1204, 024
Senatore, L., Smith, K. M., & Zaldarriaga, M. 2010, J. Cosmol. Astropart. Phys., 1, 28
Shiraishi, M. 2012, J. Cosmol. Astropart. Phys., 6, 15
Shiraishi, M., Nitta, D., & Yokoyama, S. 2011, Prog. Theor. Phys., 126, 937
Shiraishi, M., Nitta, D., Yokoyama, S., & Ichiki, K. 2012, J. Cosmol. Astropart. Phys., 1203, 041
Shiraishi, M., Komatsu, E., Peloso, M., & Barnaby, N. 2013a, J. Cosmol. Astropart. Phys., 5, 2
Shiraishi, M., Ricciardone, A., & Saga, S. 2013b, J. Cosmol. Astropart. Phys., 11, 51
Shiraishi, M., Liguori, M., & Fergusson, J. R. 2014, J. Cosmol. Astropart. Phys., 5, 8
Shiraishi, M., Liguori, M., & Fergusson, J. R. 2015, J. Cosmol. Astropart. Phys., 1, 7
Silverstein, E., & Tong, D. 2004, Phys. Rev. D, 70, 103505
Sitwell, M., & Sigurdson, K. 2014, Phys. Rev. D, 89, 123509
Smidt, J., Amblard, A., Byrnes, C. T., et al. 2010, Phys. Rev. D, 81, 123007
Smith, K. M., Senatore, L., & Zaldarriaga, M. 2009, J. Cosmol. Astropart. Phys., 9, 6
Smith, K. M., Senatore, L., & Zaldarriaga, M. 2015, ArXiv e-prints [arXiv:1502.00635]
Soda, J., Kodama, H., & Nozawa, M. 2011, J. High Energy Phys., 8, 67
Sorbo, L. 2011, J. Cosmol. Astropart. Phys., 6, 3
Spergel, D. N., Bean, R., Doré, O., et al. 2007, ApJS, 170, 377
Toffolatti, L., Argueso Gomez, F., de Zotti, G., et al. 1998, MNRAS, 297, 117
Tzavara, E., & van Tent, B. 2011, J. Cosmol. Astropart. Phys., 6, 26
Vanmarcke, E. 1983, Random Fields (Cambridge: The Mit Press)
Verde, L., Wang, L., Heavens, A. F., & Kamionkowski, M. 2000, MNRAS, 313, 141
Vernizzi, F., & Wands, D. 2006, J. Cosmol. Astropart. Phys., 5, 19
Vielva, P., & Sanz, J. 2010, MNRAS, 404, 895
Wang, L., & Kamionkowski, M. 2000, Phys. Rev. D, 61, 063504
Weinberg, S. 2008, Phys. Rev. D, 77, 123541
Wiegand, A., Buchert, T., & Ostermann, M. 2014, MNRAS, 443, 241
Winitzki, S., & Kosowsky, A. 1998, New Astron., 3, 75
Yadav, A. P. S., & Wandelt, B. D. 2008, Phys. Rev. Lett., 100, 181301
Yadav, A. P. S., & Wandelt, B. D. 2010, Adv. Astron., 2010, 565248
Yadav, A. P. S., Komatsu, E., & Wandelt, B. D. 2007, ApJ, 664, 680
Yadav, A. P. S., Komatsu, E., Wandelt, B. D., et al. 2008, ApJ, 678, 578
Zaldarriaga, M. 2004, Phys. Rev. D, 69, 043508

[1] APC, AstroParticule et Cosmologie, Université Paris Diderot, CNRS/IN2P3, CEA/lrfu, Observatoire de Paris, Sorbonne Paris Cité, 10 rue Alice Domon et Léonie Duquet, 75205 Paris Cedex 13, France

[2] Aalto University Metsähovi Radio Observatory and Dept of Radio Science and Engineering, PO Box 13000, 00076 Aalto, Finland

[3] African Institute for Mathematical Sciences, 6-8 Melrose Road, Muizenberg 7945, Cape Town, South Africa

[4] Agenzia Spaziale Italiana Science Data Center, via del Politecnico snc, 00133 Roma, Italy

[5] Aix-Marseille Université, CNRS, LAM (Laboratoire d'Astrophysique de Marseille) UMR 7326, 13388 Marseille, France

[6] Astrophysics Group, Cavendish Laboratory, University of Cambridge, J J Thomson Avenue, Cambridge CB3 0HE, UK

[7] Astrophysics & Cosmology Research Unit, School of Mathematics, Statistics & Computer Science, University of KwaZulu-Natal, Westville Campus, Private Bag X54001, Durban 4000, South Africa

[8] CGEE, SCS Qd 9, Lote C, Torre C, 4° andar, Ed. Parque Cidade Corporate, 70308-200 Brasília, DF, Brazil

[9] CITA, University of Toronto, 60 St. George St., Toronto, ON M5S 3H8, Canada

[10] CNRS, IRAP, 9 Av. colonel Roche, BP 44346, 31028 Toulouse Cedex 4, France

[11] CRANN, Trinity College, Dublin, Ireland

[12] California Institute of Technology, Pasadena, CA 91125, USA

[13] Centre for Theoretical Cosmology, DAMTP, University of Cambridge, Wilberforce Road, Cambridge CB3 0WA, UK

[14] Centro de Estudios de Física del Cosmos de Aragón (CEFCA), Plaza San Juan, 1, planta 2, 44001 Teruel, Spain

[15] Computational Cosmology Center, Lawrence Berkeley National Laboratory, Berkeley, CA 94720, USA

[16] Consejo Superior de Investigaciones Científicas (CSIC), 28006 Madrid, Spain

[17] DSM/Irfu/SPP, CEA-Saclay, 91191 Gif-sur-Yvette Cedex, France

[18] DTU Space, National Space Institute, Technical University of Denmark, Elektrovej 327, 2800 Kgs. Lyngby, Denmark

[19] Département de Physique Théorique, Université de Genève, 24 quai E. Ansermet, 1211 Genève 4, Switzerland

[20] Departamento de Astrofísica, Universidad de La Laguna (ULL), 38206 La Laguna, Tenerife, Spain

[21] Departamento de Física, Universidad de Oviedo, Avda. Calvo Sotelo s/n, 33007 Oviedo, Spain

[22] Department of Astronomy and Astrophysics, University of Toronto, 50 Saint George Street, Toronto, Ontario, Canada

[23] Department of Astrophysics/IMAPP, Radboud University Nijmegen, PO Box 9010, 6500 GL Nijmegen, The Netherlands

[24] Department of Physics & Astronomy, University of British Columbia, 6224 Agricultural Road, Vancouver, British Columbia, Canada

[25] Department of Physics and Astronomy, Dana and David Dornsife College of Letter, Arts and Sciences, University of Southern California, Los Angeles, CA 90089, USA

[26] Department of Physics and Astronomy, University College London, London WC1E 6BT, UK

[27] Department of Physics and Astronomy, University of Sussex, Brighton BN1 9QH, UK

[28] Department of Physics, Florida State University, Keen Physics Building, 77 Chieftan Way, Tallahassee, Florida, USA

[29] Department of Physics, Gustaf Hällströmin katu 2a, University of Helsinki, 00014 Helsinki, Finland

[30] Department of Physics, Princeton University, Princeton, NJ 08544, USA

[31] Department of Physics, University of California, Santa Barbara, CA 93106, USA

[32] Department of Physics, University of Illinois at Urbana-Champaign, 1110 West Green Street, Urbana, Illinois, USA

[33] Dipartimento di Fisica e Astronomia G. Galilei, Università degli Studi di Padova, via Marzolo 8, 35131 Padova, Italy

[34] Dipartimento di Fisica e Astronomia, Alma Mater Studiorum, Università degli Studi di Bologna, viale Berti Pichat 6/2, 40127 Bologna, Italy

[35] Dipartimento di Fisica e Scienze della Terra, Università di Ferrara, via Saragat 1, 44122 Ferrara, Italy

[36] Dipartimento di Fisica, Università La Sapienza, P.le A. Moro 2, 00185 Roma, Italy

[37] Dipartimento di Fisica, Università degli Studi di Milano, via Celoria 16, 20133 Milano, Italy

[38] Dipartimento di Fisica, Università degli Studi di Trieste, via A. Valerio 2, 34127 Trieste, Italy

[39] Dipartimento di Matematica, Università di Roma Tor Vergata, via della Ricerca Scientifica 1, 00133 Roma, Italy

[40] Discovery Center, Niels Bohr Institute, Blegdamsvej 17, 2100 Copenhagen, Denmark

[41] Discovery Center, Niels Bohr Institute, Copenhagen University, Blegdamsvej 17, 2100 Copenhagen, Denmark

[42] European Space Agency, ESAC, Planck Science Office, Camino bajo del Castillo, s/n, Urbanización Villafranca del Castillo, 28692 Villanueva de la Cañada, Madrid, Spain

[43] European Space Agency, ESTEC, Keplerlaan 1, 2201 AZ Noordwijk, The Netherlands

[44] Gran Sasso Science Institute, INFN, viale F. Crispi 7, 67100 L'Aquila, Italy

[45] HGSFP and University of Heidelberg, Theoretical Physics Department, Philosophenweg 16, 69120 Heidelberg, Germany

[46] Helsinki Institute of Physics, Gustaf Hällströmin katu 2, University of Helsinki, 00014 Helsinki, Finland

[47] ICTP South American Institute for Fundamental Research, Instituto de Física Teórica, Universidade Estadual Paulista, 01140-070 São Paulo, Brazil

[48] INAF−Osservatorio Astronomico di Padova, Vicolo dell'Osservatorio 5, 35122 Padova, Italy

[49] INAF−Osservatorio Astronomico di Roma, via di Frascati 33, 00040 Monte Porzio Catone, Italy

[50] INAF−Osservatorio Astronomico di Trieste, via G.B. Tiepolo 11, 40127 Trieste, Italy

[51] INAF/IASF Bologna, via Gobetti 101, 40129 Bologna, Italy

[52] INAF/IASF Milano, via E. Bassini 15, 20133 Milano, Italy

[53] INFN, Sezione di Bologna, via Irnerio 46, 40126 Bologna, Italy

[54] INFN, Sezione di Roma 1, Università di Roma Sapienza, P.le Aldo Moro 2, 00185 Roma, Italy

[55] INFN, Sezione di Roma 2, Università di Roma Tor Vergata, via della Ricerca Scientifica 1, 00185 Roma, Italy

[56] INFN/National Institute for Nuclear Physics, via Valerio 2, 34127 Trieste, Italy

[57] IPAG: Institut de Planétologie et d'Astrophysique de Grenoble, Université Grenoble Alpes, IPAG, CNRS, IPAG, 38000 Grenoble, France

[58] IUCAA, Post Bag 4, Ganeshkhind, Pune University Campus, 411 007 Pune, India

[59] Imperial College London, Astrophysics group, Blackett Laboratory, Prince Consort Road, London, SW7 2AZ, UK

[60] Infrared Processing and Analysis Center, California Institute of Technology, Pasadena, CA 91125, USA

[61] Institut Néel, CNRS, Université Joseph Fourier Grenoble I, 25 rue des Martyrs, Grenoble, France

[62] Institut Universitaire de France, 103 bd Saint-Michel, 75005 Paris, France

[63] Institut d'Astrophysique Spatiale, CNRS, Univ. Paris-Sud, Université Paris-Saclay, Bât. 121, 91405 Orsay Cedex, France

[64] Institut d'Astrophysique de Paris, CNRS (UMR 7095), 98bis boulevard Arago, 75014 Paris, France

[65] Institut für Theoretische Teilchenphysik und Kosmologie, RWTH Aachen University, 52056 Aachen, Germany

[66] Institute for Space Sciences, 077125 Bucharest-Magurale, Romania

[67] Institute of Astronomy, University of Cambridge, Madingley Road, Cambridge CB3 0HA, UK

[68] Institute of Theoretical Astrophysics, University of Oslo, Blindern, 0371 Oslo, Norway

[69] Instituto de Astrofísica de Canarias, C/Vía Láctea s/n, La Laguna, 38205 Tenerife, Spain

[70] Instituto de Física de Cantabria (CSIC-Universidad de Cantabria), Avda. de los Castros s/n, 39005 Santander, Spain

[71] Istituto Nazionale di Fisica Nucleare, Sezione di Padova, via Marzolo 8, 35131 Padova, Italy

[72] Jet Propulsion Laboratory, California Institute of Technology, 4800 Oak Grove Drive, Pasadena, CA 31109, USA

[73] Jodrell Bank Centre for Astrophysics, Alan Turing Building, School of Physics and Astronomy, The University of Manchester, Oxford Road, Manchester, M13 9PL, UK

[74] Kavli Institute for Cosmological Physics, University of Chicago, Chicago, IL 60637, USA

[75] Kavli Institute for Cosmology Cambridge, Madingley Road, Cambridge, CB3 0HA, UK

[76] Kazan Federal University, 18 Kremlyovskaya St., 420008 Kazan, Russia

[77] LAL, Université Paris-Sud, CNRS/IN2P3, 91898 Orsay, France

[78] LERMA, CNRS, Observatoire de Paris, 61 avenue de l'Observatoire, 75014 Paris, France

[79] Laboratoire AIM, IRFU/Service d'Astrophysique – CEA/DSM – CNRS – Université Paris Diderot, Bât. 709, CEA-Saclay, 91191 Gif-sur-Yvette Cedex, France

[80] Laboratoire Traitement et Communication de l'Information, CNRS (UMR 5141) and Télécom ParisTech, 46 rue Barrault, 75634 Paris Cedex 13, France

[81] Laboratoire de Physique Subatomique et Cosmologie, Université Grenoble-Alpes, CNRS/IN2P3, 53 rue des Martyrs, 38026 Grenoble Cedex, France

[82] Laboratoire de Physique Théorique, Université Paris-Sud 11 & CNRS, Bâtiment 210, 91405 Orsay, France

[83] Lawrence Berkeley National Laboratory, Berkeley, California, USA

[84] Lebedev Physical Institute of the Russian Academy of Sciences, Astro Space Centre, 84/32 Profsoyuznaya st., GSP-7, 117997 Moscow, Russia

[85] Leung Center for Cosmology and Particle Astrophysics, National Taiwan University, Taipei 10617, Taiwan

[86] Max-Planck-Institut für Astrophysik, Karl-Schwarzschild-Str. 1, 85741 Garching, Germany

[87] McGill Physics, Ernest Rutherford Physics Building, McGill University, 3600 rue University, Montréal, QC, H3A 2T8, Canada

[88] National University of Ireland, Department of Experimental Physics, Maynooth, Co. Kildare, Ireland

[89] Nicolaus Copernicus Astronomical Center, Bartycka 18, 00-716 Warsaw, Poland

[90] Niels Bohr Institute, Blegdamsvej 17, 2100 Copenhagen, Denmark

[91] Niels Bohr Institute, Copenhagen University, Blegdamsvej 17, 2100 Copenhagen, Denmark

[92] Nordita (Nordic Institute for Theoretical Physics), Roslagstullsbacken 23, 106 91 Stockholm, Sweden

[93] Optical Science Laboratory, University College London, Gower Street, WC1E 6BT London, UK

[94] Perimeter Institute for Theoretical Physics, Waterloo ON N2L 2Y5, Canada

[95] SISSA, Astrophysics Sector, via Bonomea 265, 34136 Trieste, Italy

[96] SMARTEST Research Centre, Università degli Studi e-Campus, via Isimbardi 10, 22060 Novedrate (CO), Italy

[97] School of Physics and Astronomy, Cardiff University, Queens Buildings, The Parade, Cardiff, CF24 3AA, UK

[98] School of Physics and Astronomy, University of Nottingham, Nottingham NG7 2RD, UK

[99] Sorbonne Université-UPMC, UMR 7095, Institut d'Astrophysique de Paris, 98bis boulevard Arago, 75014 Paris, France

[100] Space Research Institute (IKI), Russian Academy of Sciences, Profsoyuznaya Str, 84/32, 117997 Moscow, Russia

[101] Space Sciences Laboratory, University of California, Berkeley, CA 94720, USA

[102] Special Astrophysical Observatory, Russian Academy of Sciences, Nizhnij Arkhyz, Zelenchukskiy region, 369167 Karachai-Cherkessian Republic, Russia

[103] Stanford University, Dept of Physics, Varian Physics Bldg, 382 via Pueblo Mall, Stanford, California, CA 94305-4060, USA

[104] Sub-Department of Astrophysics, University of Oxford, Keble Road, Oxford OX1 3RH, UK

[105] Sydney Institute for Astronomy, School of Physics A28, University of Sydney, NSW 2006, Australia

[106] The Oskar Klein Centre for Cosmoparticle Physics, Department of Physics, Stockholm University, AlbaNova, 106 91 Stockholm, Sweden

[107] Theory Division, PH-TH, CERN, 1211 Geneva 23, Switzerland

[108] UPMC Univ. Paris 06, UMR 7095, 98bis boulevard Arago, 75014 Paris, France

[109] Université de Toulouse, UPS-OMP, IRAP, 31028 Toulouse Cedex 4, France

[110] University of Granada, Departamento de Física Teórica y del Cosmos, Facultad de Ciencias, 18071 Granada, Spain

[111] University of Granada, Instituto Carlos I de Física Teórica y Computacional, 18071 Granada, Spain

[112] Warsaw University Observatory, Aleje Ujazdowskie 4, 00-478 Warszawa, Poland

Appendix A: Derivation of an estimator for c_L

As parameterized by Eq. (23), we express a primordial bispectrum of direction-dependence:

$$B_\Phi(k_1, k_2, k_3) =$$
$$\sum_{L \geq 1} c_L \left[P_L(\hat{\boldsymbol{k}}_1 \cdot \hat{\boldsymbol{k}}_2) P_\Phi(k_1) P_\Phi(k_2) + 2\,\text{perm.} \right] \quad (A.1)$$

where $P_L(\hat{\boldsymbol{k}}_1 \cdot \hat{\boldsymbol{k}}_2)$ is a Legendre Polynomial of order L. It can be shown that such a primordial bispectrum leads to a CMB bispectrum

$$\langle a_{l_1 m_1}^{p_1} a_{l_2 m_2}^{p_2} a_{l_3 m_3}^{p_3} \rangle = \quad (A.2)$$

$$(-\iota)^{\ell_1 + \ell_2 + \ell_3} (4\pi)^3 \int \frac{d^3 \boldsymbol{k}_1}{(2\pi)^3} g_{l_1}^{p_1}(k_1) Y_{l_1 m_1}^*(\hat{\boldsymbol{k}}_1)$$

$$\times \int \frac{d^3 \boldsymbol{k}_2}{(2\pi)^3} g_{l_2}^{p_2}(k_2) Y_{l_2 m_3}^*(\hat{\boldsymbol{k}}_2) \int \frac{d^3 \boldsymbol{k}_3}{(2\pi)^3} g_{l_3}^{p_3}(k_3) Y_{l_3 m_3}^*(\hat{\boldsymbol{k}}_3)$$

$$\times (2\pi)^3 \delta^{(3)}(\boldsymbol{k}_1 + \boldsymbol{k}_2 + \boldsymbol{k}_3) c_L \left[P_L(\hat{\boldsymbol{k}}_1 \cdot \hat{\boldsymbol{k}}_2) P_\Phi(k_1) P_\Phi(k_2) + 2\,\text{perm.} \right]$$

$$= \begin{pmatrix} \ell_1 & \ell_2 & \ell_3 \\ m_1 & m_2 & m_3 \end{pmatrix} \left(\sum_L c_L b_{\ell_1 \ell_2 \ell_3}^{(c_L), p_1 p_2 p_3} \right),$$

where p denotes either temperature or E-mode polarization, $b_{\ell_1 \ell_2 \ell_3}^{(c_L), p_1 p_2 p_3}$ is the reduced CMB bispectrum, and the term with large parentheses denotes the Wigner-3j symbol. The reduced CMB bispectrum $b_{\ell_1 \ell_2 \ell_3}^{(c_L), p_1 p_2 p_3}$ is given by (Shiraishi et al. 2013a)

$$b_{\ell_1 \ell_2 \ell_3}^{(c_L), p_1 p_2 p_3} = \frac{4\pi}{2L+1} \frac{w_{\ell_1} w_{\ell_2} w_{\ell_3} \iota^{\ell_1 + \ell_2 + \ell_3}}{h_{\ell_1 \ell_2 \ell_3}} \int_0^\infty r^2 dr$$

$$\times \sum_{L_1 L_2 L_3} \iota^{L_1 + L_2 + L_3} h_{L_1 L_2 L_3} \left[h_{\ell_1 L_1 L} h_{\ell_2 L_2 L} (-1)^{L_1 + L_2 + L} \delta_{L_3, \ell_3} \right.$$

$$\times \left. \beta_{\ell_1 L_1}^{p_1}(r) \beta_{\ell_2 L_2}^{p_2}(r) \alpha_{\ell_3}^{p_3}(r) \begin{Bmatrix} \ell_1 & \ell_3 & \ell_3 \\ L_2 & L_1 & L \end{Bmatrix} + 2\,\text{perm.} \right], (A.3)$$

where $\delta_{L,l}$ denotes the Kronecker delta function, $\{\ldots\}$ the Wigner 6j symbol, "perm." means permutations, w_ℓ is a beam window function, and

$$\alpha_\ell^p(r) = \frac{2}{\pi} \int k^3 \, d\ln k \; g_\ell^p(k) j_\ell(kr), \quad (A.4)$$

$$\beta_{\ell, \ell'}^p(r) = \frac{2}{\pi} \int dk^3 \ln k \, P_\Phi(k) g_\ell^p(k) j_{\ell'}(kr). \quad (A.5)$$

Here, $g_\ell^p(k)$ is the radiation transfer function for temperature or E-mode polarization, and $j_\ell(x)$ is a spherical Bessel function. The h symbol is

$$h_{\ell_1 \ell_2 \ell_3} = \sqrt{\frac{(2\ell_1 + 1)(2\ell_2 + 1)(2\ell_3 + 1)}{4\pi}} \begin{pmatrix} \ell_1 & \ell_2 & \ell_3 \\ 0 & 0 & 0 \end{pmatrix}. \quad (A.6)$$

By maximizing the likelihood with respect to c_L, we obtain the KSW estimator for c_L:

$$\hat{c}_L = \frac{1}{6 \, \mathcal{N}_{c_L}} \sum_{p_i q_i} \sum_{\ell_i m_i} \mathcal{G}_{\ell_1 \ell_2 \ell_3}^{m_1 m_2 m_3} b_{\ell_1 \ell_2 \ell_3}^{(c_L), p_1 p_2 p_3}$$

$$\times \left[(C^{-1} a)_{\ell_1 m_1}^{p_1} (C^{-1} a)_{\ell_2 m_2}^{p_2} (C^{-1} a)_{\ell_3 m_3}^{p_3} \right.$$

$$\left. - 3 \langle (C^{-1} a)_{\ell_1 m_1}^{p_1} (C^{-1} a)_{\ell_2 m_2}^{p_2} \rangle_{\text{MC}} (C^{-1} a)_{\ell_3 m_3}^{p_3} \right], \quad (A.7)$$

where MC denotes that the average is over Monte Carlo simulations and $\mathcal{N}_{c_L}$ is a normalization constant. The normalization constant $\mathcal{N}_{c_L}$ is given by

$$\mathcal{N}_{c_L} = \frac{1}{6} \sum_{p_i q_i} \sum_{\ell_i} (h_{\ell_1 \ell_2 \ell_3})^2 \quad (A.8)$$

$$\times b_{\ell_1 \ell_2 \ell_3}^{(c_L), p_1 p_2 p_3} (C^{-1})_{\ell_1}^{p_1 q_1} (C^{-1})_{\ell_2}^{p_2 q_2} (C^{-1})_{l_3}^{p_3 q_3} b_{\ell_1 \ell_2 \ell_3}^{(c_L), q_1 q_2 q_3}.$$

Using Eq. (A.2), we find that

$$\sum_{p_i \ell_i m_i} \mathcal{G}_{\ell_1 \ell_2 \ell_3}^{m_1 m_2 m_3} b_{\ell_1 \ell_2 \ell_3}^{(c_L), p_1 p_2 p_3} (C^{-1} a)_{\ell_1 m_1}^{p_1} (C^{-1} a)_{\ell_2 m_2}^{p_2} (C^{-1} a)_{\ell_3 m_3}^{p_3}$$

$$= \int r^2 dr \int d\Omega \frac{4\pi}{2L+1} \left(\sum_{q_3 \ell_3 m_3} \alpha_{\ell_3}^{p_3}(r) (C^{-1} a)_{\ell_3 m_3}^{p_3} Y_{\ell_3 m_3}(\hat{\boldsymbol{n}}) \right)$$

$$\times \sum_{M=-L}^L (-1)^M \left(\sum_{\ell_1' m_1'} b_{\ell_1' m_1'}^{LM}(r) Y_{\ell_1' m_1'}(\hat{\boldsymbol{n}}) \right) \left(\sum_{\ell_2' m_2'} b_{\ell_2' m_2'}^{L-M}(r) Y_{\ell_2' m_2'}(\hat{\boldsymbol{n}}) \right)$$

$$+ 2 \;\text{perm.}, \quad (A.9)$$

where

$$b_{\ell' m'}^{LM}(r) = \sum_{pq\ell m} (-1)^{\ell+m} \iota^{\ell+\ell'} h_{\ell' \ell L} \begin{pmatrix} \ell & \ell' & L \\ -m & m' & M \end{pmatrix} \beta_{\ell, \ell'}^p(r) w_\ell (C^{-1})_l^{pq} a_{\ell m}^q,$$

with $\beta_{\ell, \ell'}^p(r)$ being defined in Eq. (A.5). In the derivation above, we used the identities

$$P_L(\hat{\boldsymbol{k}}_1 \cdot \hat{\boldsymbol{k}}_2) = \frac{4\pi}{2L+1} \sum_M Y_{LM}(\hat{\boldsymbol{k}}_1) Y_{LM}^*(\hat{\boldsymbol{k}}_2),$$

and

$$\delta(\boldsymbol{k}_1 + \boldsymbol{k}_2 + \boldsymbol{k}_3) = 8 \int dr \, dn^2 \sum_{\ell_1 m_1} \iota^{\ell_1} j_{\ell_1}(k_1 r) Y_{\ell_1 m_1}(\hat{\boldsymbol{k}}_1) Y_{\ell_1 m_1}^*(\hat{\boldsymbol{n}})$$

$$\times \sum_{\ell_2 m_2} \iota^{\ell_2} j_{\ell_2}(k_2 r) Y_{\ell_2 m_2}(\hat{\boldsymbol{k}}_2) Y_{\ell_2 m_2}^*(\hat{\boldsymbol{n}}) \sum_{\ell_3 m_3} \iota^{\ell_3} j_{\ell_3}(k_3 r) Y_{\ell_3 m_3}(\hat{\boldsymbol{k}}_3) Y_{\ell_3 m_3}^*(\hat{\boldsymbol{n}}).$$

Applying Eqs. (A.9) to (A.7), we find

$$\hat{c}_L = \frac{1}{\mathcal{N}_{c_L}} \frac{2\pi}{(2L+1)} \sum_{M=-L}^L (-1)^M \int r^2 dr \int d^2 \hat{\boldsymbol{n}}$$

$$[A(\hat{\boldsymbol{n}}, r) B_{LM}(\hat{\boldsymbol{n}}, r) B_{L,-M}(\hat{\boldsymbol{n}}, r) - A(\hat{\boldsymbol{n}}, r) \langle B_{LM}(\hat{\boldsymbol{n}}, r) B_{L,-M}(\hat{\boldsymbol{n}}, r) \rangle_{\text{MC}}$$

$$- 2 B_{L,-M}(\hat{\boldsymbol{n}}, r) \langle A(\hat{\boldsymbol{n}}, r) B_{LM}(\hat{\boldsymbol{n}}, r) \rangle_{\text{MC}}],$$

where

$$A(\hat{\boldsymbol{n}}, r) = \sum_{\ell m} \sum_{pq} \alpha_\ell^p(r) (C^{-1})_l^{pq} a_{\ell m}^q Y_{\ell m}(\hat{\boldsymbol{n}}),$$

$$B_{LM}(\hat{\boldsymbol{n}}, r) = \sum_{\ell m} b_{\ell m}^{LM}(r) Y_{\ell m}(\hat{\boldsymbol{n}}).$$

Since $b_{\ell' m'}^{LM}(r) \neq (-1)^{m'} \left[b_{\ell', -m'}^{LM}(r) \right]^*$, $B_{LM}(\hat{\boldsymbol{n}}, r)$ is not a real function, but a complex function. We estimate $B_{LM}(\hat{\boldsymbol{n}}, r)$ efficiently by computing the following with HEALPix (Górski et al. 2005):

$$\text{Re}[B_{LM}(\hat{\boldsymbol{n}}, r)] = \sum_{\ell m} \mathcal{R}_{\ell m}^{LM}(r) Y_{\ell m}(\hat{\boldsymbol{n}});$$

$$\text{Im}[B_{LM}(\hat{\boldsymbol{n}}, r)] = \sum_{\ell m} \mathcal{I}_{\ell m}^{LM}(r) Y_{\ell m}(\hat{\boldsymbol{n}}).$$

Here

$$\mathcal{R}_{\ell m}^{LM}(r) = \frac{b_{\ell m}^{LM}(r) + (-1)^m [b_{\ell-m}^{LM}(r)]^*}{2},$$

$$\mathcal{I}_{\ell m}^{LM}(r) = \frac{b_{\ell m}^{LM}(r) - (-1)^m [b_{\ell-m}^{LM}(r)]^*}{2\iota}.$$

Appendix B: Definition of Minkowski Functionals and theoretical expectations

For a field $f(x)$ of zero average and variance σ_0^2 defined on the two-dimensional sphere $\mathbb{S}^2$, an overdense excursion set is defined as

$$\Sigma \equiv \{x \in \mathbb{S}^2 | f(x) > \nu\sigma_0\}. \tag{B.1}$$

The boundary of the excursion is

$$\partial\Sigma \equiv \{x \in \mathbb{S}^2 | f(x) = \nu\sigma_0\}. \tag{B.2}$$

Then the three Minkowski functionals on the sphere are

$$\text{Area}: V_0(\nu) = \frac{1}{4\pi} \int_\Sigma d\Omega, \tag{B.3}$$

$$\text{Perimeter}: V_1(\nu) = \frac{1}{4\pi} \frac{1}{4} \int_{\partial\Sigma} dl, \tag{B.4}$$

$$\text{Genus}: V_2(\nu) = \frac{1}{4\pi} \frac{1}{2\pi} \int_{\partial\Sigma} \kappa \, dl, \tag{B.5}$$

where $d\Omega$ and dl are respectively elements of solid angles (surface) and of angle (distance), κ is the geodesic curvature. Note that the Genus can be also expressed as the number of components[22] in the excursion minus the number of holes in the excursion.

The fourth functional $V_3(\nu)$, is defined, for $\nu > 0$, as the number of components in the excursion. Symmetrically, for $\nu < 0$, it is the number of underdense components (or the number of components in the excursion $\{x \in \mathbb{S}^2 | f(x) < \nu\sigma_0\}$).

In the Gaussian limit, the functionals can be expressed the following way (see, e.g., Matsubara 2010; Vanmarcke 1983):

$$V_k(\nu) = A_k v_k(\nu), \tag{B.6}$$

with

$$v_k(\nu) = \exp(-\nu^2/2) H_{k-1}(\nu), \quad k \le 2 \tag{B.7}$$

$$v_3(\nu) = \frac{e^{-\nu^2}}{\text{erfc}(\nu/\sqrt{2})}, \tag{B.8}$$

and

$$H_n(\nu) = e^{\nu^2/2} \left(-\frac{d}{d\nu}\right)^n e^{-\nu^2/2}. \tag{B.9}$$

The amplitude A_k depends only on the shape of the power spectrum C_ℓ:

$$A_k = \frac{1}{(2\pi)^{(k+1)/2}} \frac{\omega_2}{\omega_{2-k}\omega_k} \left(\frac{\sigma_1}{\sqrt{2}\sigma_0}\right)^k, \quad k \le 2 \tag{B.10}$$

$$A_3 = \frac{2}{\pi} \left(\frac{\sigma_1}{\sqrt{2}\sigma_0}\right)^2 \tag{B.11}$$

where $\omega_k \equiv \pi^{k/2}/\Gamma(k/2+1)$, which gives $\omega_0 = 1$, $\omega_1 = 2$, $\omega_2 = \pi$ and σ_0 and σ_1 are respectively the rms of the field and its first derivatives.

---

[22] A component is a connected subset of the excursion.